(2)

Polytechnic
UNIVERSITY

POLY-WRI 1537-88

"The Role of Hydromagnetic Waves in the Magnetosphere and the Ionosphere"

S.P. Kuo, Principal Investigator

Route 110 Farmingdale, New York 11735

Weber Research Institute

UNCLASSIFIED

SECURITY CLASSIFICATION OF THIS PAGE

REPORT DOCUMENTATION PAGE

1a. REPORT SECURITY CLASSIFICATION UNCLASSIFIED	1b. RESTRICTIVE MARKINGS
2a. SECURITY CLASSIFICATION AUTHORITY	3. DISTRIBUTION / AVAILABILITY OF REPORT Approved for public release; distribution is unlimited.
2b. DECLASSIFICATION / DOWNGRADING SCHEDULE	
4. PERFORMING ORGANIZATION REPORT NUMBER(S)	5. MONITORING ORGANIZATION REPORT NUMBER(S) AFOSR-TR- 88-1251
6a. NAME OF PERFORMING ORGANIZATION Polytechnic University 6b. OFFICE SYMBOL (If applicable)	7a. NAME OF MONITORING ORGANIZATION AFOSR/NP
6c. ADDRESS (City, State, and ZIP Code) 333 Jay Street Brooklyn, NY 11201	7b. ADDRESS (City, State, and ZIP Code) Building 410, Bolling AFB DC 20332-6448
8a. NAME OF FUNDING / SPONSORING ORGANIZATION AFOSR 8b. OFFICE SYMBOL (If applicable) NP	9. PROCUREMENT INSTRUMENT IDENTIFICATION NUMBER AFOSR-85-0133
8c. ADDRESS (City, State, and ZIP Code) Building 410, Bolling AFB DC 20332-6448	10. SOURCE OF FUNDING NUMBERS PROGRAM ELEMENT NO. 61102F; PROJECT NO. 2311; TASK NO. A1; WORK UNIT ACCESSION NO.

11. TITLE (Include Security Classification)

(U) THE ROLE OF HYDROMAGNETIC WAVES IN THE MAGNETOSPHERE AND THE IONOSphere

12. PERSONAL AUTHOR(S)

13a. TYPE OF REPORT	13b. TIME COVERED	14. DATE OF REPORT (Year, Month, Day)	15. PAGE COUNT
FINAL	FROM 1 Feb 85 TO 31 Jan 88	May 1988	62

16. SUPPLEMENTARY NOTATION

17. COSATI CODES			18. SUBJECT TERMS (Continue on reverse if necessary and identify by block number)
FIELD	GROUP	SUB-GROUP	
	0401		

19. ABSTRACT (Continue on reverse if necessary and identify by block number)

The topics of investigation are devided into four general categories: ~~(a)~~ cavity modes of the magnetosphere resulting in the discrete spectrum of the resonant ULF waves; ~~(b)~~ a hydromagnetic code for the numerical study of the coupling of hydromagnetic waves in the dipole model of the magnetosphere; ~~(c)~~ a theoretical model developed for explaining the phenomenon of plasma line overshoot observed in the ionospheric HF heating experiments; and ~~(d)~~ thermal filamentation instability as the mechanism for generation of large-scale field-aligned ionospheric irregularities. For the first two topics, the hydromagnetic wave equations are analyzed analytically in cylindrical model of the magnetosphere and numerically in dipole model of the magnetosphere, respectively. While the steady state eigenvalue problem is studied in the first topic, the second topic is generalized to the boundary value problem considering the coupling between hydromagnetic waves in the realistic geometry of the magnetosphere. For the third topic, a nonlinear turbulent theory (resonance broadening of electron-wave interaction) is incorporated in the study of parameter instability excited by a powerful HF in the ionosphere. For the last topic, the thermal nonlinearity gives rise to the mode-mode coupling; threshold field and the growth rate of the instability are derived.

20. DISTRIBUTION / AVAILABILITY OF ABSTRACT	21. ABSTRACT SECURITY CLASSIFICATION
X ☐ UNCLASSIFIED/UNLIMITED X ☐ SAME AS RPT. ☐ DTIC USERS	UNCLASSIFIED

22a. NAME OF RESPONSIBLE INDIVIDUAL	22b. TELEPHONE (Include Area Code)	22c. OFFICE SYMBOL
H R RADOSKI	(202) 767-4906	AFOSR/NP

DD FORM 1473, 84 MAR 83 APR edition may be used until exhausted. All other editions are obsolete.

SECURITY CLASSIFICATION OF THIS PAGE

UNCLASSIFIED

(2)

POLY-WRI 1537-88

"The Role of Hydromagnetic Waves in the Magnetosphere and the Ionosphere"

S.P. Kuo, Principal Investigator

Technical Final Report on Air Force Office of Scientific Research Grant AFOSR-85-0133

88 12

I. Introduction

The present report summarizes the work that has been carried out under the support of the AFOSR (Grant No. AFOSR-85-0133) during the funding period Feb. 1, 1985 to Jan. 31, 1988. The investigation covered by the Grant deals with the physical phenomena associated with coupled hydromagnetic waves in the magnetosphere and the physics of the coupling between the magnetosphere and ionosphere. The research effort is also extended to study naturally occurred or artificially induced phenomena related to plasma waves in the ionosphere and magnetosphere. Our study focuses primarily on developing theories to explain the observational results, however, the possibility of providing guidelines to future experiments is also considered.

During the past three years, our work has achieved many interesting results, which have been either submitted or already accepted for publication. Basically, the topics of investigation are divided into four general categories: (a) cavity modes of the magnetosphere resulting in the discrete spectrum of the resonant ULF waves; (b) a hydromagnetic code for the numerical study of the coupling of hydromagnetic waves in the dipole model of the magnetosphere; (c) a theoretical model developed for explaining the phenomenon of plasma line overshoot observed in the ionospheric HF heating experiments; and (d) thermal filamentation instability as the mechanism for generation of large-scale field-aligned ionospheric irregularities. For the first two topics, the hydromagnetic wave equations are analyzed analytically in cylindrical model of the magnetosphere and numerically in dipole model of the magnetosphere, respectively. While the steady state eigenvalue problem is studied in the first topic, the second topic is generalized to the boundary value problem considering the coupling between hydromagnetic waves in the realistic geometry of the magnetosphere. For the third topic, a nonlinear turbulent theory (resonance broadening of electron-wave interaction) is incorporated in the study of parameter instability excited by a powerful HF in the ionosphere. For the last topic, the thermal nonlinearity gives rise to the mode-mode coupling; threshold field and the growth rate of the instability are derived.

II. Publications

The following publications include work supported by the present Grant, which was duly acknowledged:

1. S.P. Kuo, M.C. Lee and A. Wolf, "A Model for the Discrete Spectrum of the Resonant ULF Waves," *EOS Trans.*, AGU, 66(18), 347, 1985.
2. S.P. Kuo, M.C. Lee and S.C. Kuo, "A Theoretical Model for Artificial Spread F Echoes," *Radio Science*, 20(3), 546-552, 1985.
3. M.C. Lee and S.P. Kuo, "Simultaneous Excitation of Large-Scale Geomagnetic Field Fluctuations and Plasma Density Irregularities by Powerful Radio Waves," *Radio Science*, 20(3), 538-545, 1985.

4. M.C. Lee and S.P. Kuo, "Resonant Electron Diffusion as a Saturation Process of the Synchrotron Maser Instability," *J. Plasma Physics*, 35, 177-184, 1986.

5. S.P. Kuo and M.C. Lee, "Parametric Excitation of Whistler Waves by HF Heater," Proceedings of Int'l. Symposium on "Modification of the Ionosphere by Powerful Radio Waves," Suzdal, USSR, Sept. 1986, pp. 109-110.

6. M.C. Lee, J.A. Kong and S.P. Kuo, "Enhanced Ionospheric Modifications by the Combined Operation of HF and VLF Heaters," Proceedings of Int'l. Symposium on "Modification of the Ionosphere by Powerful Radio Waves," Suzdal, USSR, Sept. 1986, pp. 146-147.

7. M.C. Lee, J.A. Kong and S.P. Kuo, "On the Resonant Ionospheric Heating at the Electron Gyrofrequency," Proceedings of Int'l. Symposium on "Modification of the Ionosphere by Powerful Radio Waves," Suzdal, USSR, Sept. 1986, pp. 111-112.

8. S.P. Kuo, M.C. Lee and A. Wolfe, "Dominance of Discrete Magnetospheric Cavity Modes on the Generation of Field-Line Resonances," *EOS Trans.*, AGU, 67(16), 348, 1986.

9. M.C. Lee and S.P. Kuo, "On the Causes of Spectral Broadening of Injected VLF Waves," *EOS Trans.*, AGU, 67(16), 317, 1986.

10. M.H. Whang, S.P. Kuo and M.C. Lee, "Thermal Filamentation Instability of EM Waves in Magneto Plasma," *Bull. Amer. Phys. Soc.*, 31(9), 1438, 1986.

11. S.P. Kuo, M.C. Lee and F.T. Djuth, "New Interpretation of Plasma-Line Overshoot Phenomenon," USNC/URSI, G/H2, p. 298, 12-15, Jan. 1987, Boulder, CO.

12. S.P. Kuo, M.C. Lee and F.T. Djuth, "Overshoot of HF-Enhanced Plasma Lines Due to Resonant Broadening Effects," IES '87 proceedings, 249-253, 1987.

13. S.P. Kuo, M.C. Lee and A. Wolfe, "Spectral Characteristics of Hydromagnetic Waves in the Magnetosphere," *J. Plasma Phyics*, 38, 235-243, 1987.

14. S.P. Kuo, M.C. Lee and F.T. Djuth, "A New Interpretation of Plasma-Line Overshoot Phenomena," *Geophys. Res. Lett.*, 14(9), 961-964, 1987.

15. S.P. Kuo and M.C. Lee, "Thermal Filamentation Instability Driven by the Auroral Electrojet Current," J. Geophys. Res., 93(A), 265-269, 1988.

16. S.P. Kuo, M.H. Whang and M.C. Lee, "Filamentation Instability of Large Amplitudes Alfven Waves," *J. Geophys. Res.*, accepted for publication, 1988.

17. M.H. Whang and S.P. Kuo, "The Stability Analysis of a Finite Difference Scheme for the Coupled Hydromagnetic Wave Equations in the Dipole Model of the Magnetosphere," submitted to J. Computation Phys., 1988.

III. Summary of Work Accomplished

(a) A Model for the Discrete Spectrum of the Resonant ULF Waves

The discrete nature of ULF pulsations observed in the magnetosphere is theoretically explained by using a cylindrical model [Radoski, J. Geomagn. Geoelectr., 22, 361, 1970]. A second order wave equation is derived to characterize the coupling between the poloidal and toroidal modes of the hydromagnetic waves. When the experimentally determined plasma density radial profile of "$1/r^3$" form [Cummings et al., J. Geophys. Res., 74, 778, 1969; Park et al., J. Geophys. Res., 83, 3137, 1978] is used, it is found that the wave equation has two turning points along the radial axis. By contrast, only one turning point exists in the wave equation fo Kivelson and Southwood [Geophys. Res. Lett., 12, 49, 1985] wherein the magnetosphere is described by a box model having a linearly increasing density profile with distance. Undamped eigenfunctions with discrete eigenvalues are found in our collisionless case. They are conceptually analogous to the case that has discrete eigenstates when particle is trapped by a potential well as discussed in quantum mechanics. However, there is a difference between the two cases. In the present case, the function f(r) representing the square of the wavenumber cannot simply be expressed by the difference of a constant eigenenergy and a fixed potential function as in quantum mechanics. This is because the eigenvalues is multiplied by a spatially dependent function. Therefore, the potential well determined by f(r) varies with each discrete eigenstates.

We have calculated the eigenperiods of the most readily excited modes and the most likely values of the east-west wavelengths. The wave eigenperiods are calculated to be in the Pc3-4 range. When the magnetospheric cavity is considered by a resonant filter, only discrete parts of the continuous perturbations on the magnetopause can couple to the localized field line resonance modes excited inside the magnetosphere, where the discrete nature of the spectrum is determined by the eigenmodes of the cavity. Details of this work are enclosed in the Appendix.

(b) Stability Analysis of a Finite Difference Scheme for the Coupled Hydromagnetic Wave Equations in the Dipole Model of the Magnetosphere

In the study of wave propagation in inhomogeneous magnetoplasma, the physical system is generally characterized by coupled partial differential equations. One specific example is the geomagnetic micropulsation originated by the hydromagnetic waves in the magnetosphere. It is shown that these waves in the poloidal and toroidal modes are generally governed by two coupled second order partial differential equations. Though these two equations can be reduced and combined into a single second order ordinary differential equation for a simplified cylindrical model of the magnetosphere, there is no apparent way to simplify the system of coupled equations for a more realistic dipole model of the magnetosphere in which a dipole geomagnetic field is assumed.

Moreover, the equation for the toroidal mode is shown to be a parabolic type of partial differential equation, while the poloidal mode is elliptic. Both equations have variable coefficients, therefore, for practical applications, there is considerable interest in finding or developing means of dealing with such a system of two mixed-type coupled partial differential equations with variable coefficients.

In this work, a numerical algorithm dealing with the mixed-type coupled partial differential equations with variable coefficients has been developed. The stability of the numerical scheme has been examined and solutions for the hydromagnetic wave equations are obtained on non-staggered grids by this algorithm. The main contribution of this algorithm is to offer an efficient way to examine the stability conditions first by the Fourier method and then check them by the matrix methods. Since these two methods are different, one can be sure of the stability conditions. Moreover, this algorithm leads a way for a parametric study of the stability conditions. It also becomes an advantage in the sense that the optimum parameters which can increase the accuracy of the numerical solution can be determined together with the stability analyses. Using the developed numerical scheme, the problem of coupling and propagation of hydromagnetic waves in the realistic dipole model of the magnetosphere can be studied. An example of coupled hydromagnetic waves in the dipole magnetosphere has been considered. Details of this work are addressed in the Appendix.

(c) Thermal Filamentation Instability Driven by the Auroral Electrojet Current

The high-latitude ionosphere is constantly perturbed by the ionospheric irregularities. The Farley-Buneman instability driven by electrojet current is known to be effective in generating meter and shorter-scale irregularities of type I in the E region. The irregularities of type II are of slightly larger scale-sizes and are generated through the $\vec{E} \times \vec{B}$ gradient drift instability. However, the growth rate of the two stream instability as well as of the gradient drift instability is a function of the angle between the wavevector and the direction of the electron drift. The growth rate becomes zero when the wavevector is perpendicular to the drift direction. Therefore, it is not possible to explain the radar observations in the direction perpendicular to the drift motion by using the above-mentioned instability mechanisms. In addition, in the analysis of those instabilities, energy equations are not incorporated because the plasma temperature perturbations can be ignored in those instability processes.

When the ohmic dissipation of electrojet currents is taken into account, we find that a new instability caused by the thermal effect can be excited. The physical process of the instability is through the modification of the electron-neutral collision frequency due to the electron temperature perturbation in the electrojet. The collision frequency increases with the temperature perturbation. This, in turn, further increases the joule loss os the electrojet currents. A thermal instability is thus excited through such a positive feedback process. A

dispersion relation of the instability is derived, from which the threshold electrojet current and the growth rate of the instability are determined. It is shown that the analyzed instability mechanism can indeed produce those as observed relatively large-scale (greater than tens of meters) E region irregular structures which are polarized perpendicular to the drift motion. Details of this work are enclosed in the Appendix.

(D) Overshoot of HF-Enhanced Plasma Lines due to Resonance Broadening Effects

One of the most reproducible phenomena observed in the Arecibo ionospheric heating experiments is the so-called main plasma line overshoot. In this work, a theoretical model is developed to explain the observations. This model is based on the mode suppression process introduced by the resonance broadening effect. It is expected that the presence of instabilities gives rise to perturbations on the phase space orbits of electrons. The result of the incoherent scattering of electron orbits by the total excited waves leads to electron diffusion in the velocity space along the magnetic field together with the cross field diffusion in the spatial space. These diffusion processes thus appear as an enhanced viscosity to the electron motion and therefore broaden the resonance interaction between the electrons and waves. Consequently, the increase of the anomalous damping on one plasma line can be the result of the growth of other lines in the same region. This leads to the mode-mode competition and hence, the spectral lines having smaller growth rate will likely be suppressed by the presence or larger growth rate lines. Such a mode competition process leading to the overshoot of HF-enhanced plasma lines has been described in terms of a rate equation, which determines the temporal evolution of the parametrically excited plasma lines. The result of the modal equation agrees favorably with the observations in the Arecibo heating experiments. The detail of this work is also enclosed in the Appendix.

IV. Appendix

Reprints, preprints and submitted papers attached to this report include:

1. Spectral Characteristics of Hydromagnetic Waves in the Magnetosphere.
2. Thermal Filamentation Instability Driven by the Auroral Electrojet Current.
3. Filamentation Instability of Large Amplitude Alfven Waves.
4. The Stability Analysis of a Finte Difference Scheme for the Coupled Hydromagnetic Waves Equations in the Dipole Model of the Magnetosphere.
5. A New Interpretation of Plasma-Line Overshoot Phenomena.
6. A Theoretical Model of Artificial Spread F Echoes.
7. Simulanteous Excitation of Large-Scale Geomagnetic Field Fluctuations and Plasma Density Irregularities by Powerful Radio Waves.
8. Resonant Electron Diffusion as a Saturation Process of the Synchrotron Maser Instability.
9. Parametric Excitation of Whistler Waves by HF Heater.
10. On the Resonant Ionospheric Heating at the Electron Gyrofrequency
11. Enhanced Ionospheric Modifications by the Combined Operation of HF and VLF Heaters.

J. Plasma Physics (1987), *vol.* 38, *part* 2, *pp.* 235–243
Printed in Great Britain

Spectral characteristics of hydromagnetic waves in the magnetosphere

By S. P. KUO

Polytechnic University, Route 110, Farmingdale, NY 11735

M. C. LEE

Massachusetts Institute of Technology, Cambridge, Massachusetts 02139

AND A. WOLFE

New York City Technical College of the City University of New York, Brooklyn, NY 11201

(Received 3 February 1987)

This work is intended to explain why the resonant response of the magnetosphere prefers to have discrete frequencies. Using a cylindrical model for the outer magnetosphere with a plasma density profile proportional to $1/r^3$, we show that the eigenequation characterizing the eigenmodes of the hydromagnetic waves in this model has two turning points along the radial axis. The locations of the turning points depend upon the values of the eigenperiod and the associated east–west wavenumber of the eigenmode. The energy spectrum of the excited cavity modes is seen to have sharp peaks at discrete frequencies when the surface perturbations have a uniform spectrum in the frequency range of interest. We, therefore, have also shown that only the discrete set of the magnetospheric cavity eigenmodes can efficiently couple the perturbations excited on the boundary of the magnetosphere to the field-line resonant mode excited inside the inner turning point of the cavity eigenmode. The most likely values of east–west wavenumbers and wave period range are determined.

1. Introduction

During the past two decades, there has been a surge of interest in understanding geomagnetic micropulsations. Vigorous observational work (Allan & Poulter 1984; Walker & Greenwald 1981) and theoretical research (Radoski 1970, 1971, 1973, 1974; Chen & Hasegawa 1974; Southwood & Hughes 1983; Rostoker 1979; Lanzerotti & Southwood 1979) have been carried out on hydromagnetic waves and geomagnetic pulsations. It is generally believed that micropulsations are caused by hydromagnetic waves which can be generated near the boundaries of the magnetosphere, internally or externally depending on local time and on the frequency ranges of the pulsations. For example, hydromagnetic waves of poloidal and toroidal modes transmitted along geomagnetic field lines can be excited during geomagnetic storms on the nightside and they can be excited by the Kelvin–Helmholtz instability during quiet times on the dayside magnetopause. These waves then give rise to

signatures of geomagnetic pulsations which can also be used as indicators of the changes in the magnetospheric configuration. The resonant field-line picture (Chen & Hasegawa 1974; Southwood 1974) explains successfully the variation of the amplitude of the geomagnetic pulsation with latitude. This model also explains very well the associated latitudinal variation of the wave polarization (Samson, Jackobs & Rostoker 1971; Lanzerotti *et al.* 1974*a*, *b*). However, the above enumerated work does not explain why the resonant response of the magnetosphere is often observed to have a discrete spectrum of frequencies (Kokubum & Nagata 1965; Stuart, Sherwood & MacIntosh 1971; Takahashi & McPherron 1982). Moreover, the solution of the field-line resonance mode predicts spatially dependent eigenfrequencies and thus contains mathematical inconsistencies in the analysis (Radoski & McClay 1967).

We show in this paper that the cavity modes of the magnetosphere characterized with a discrete spectrum of frequencies can play a dominant role in geomagnetic ULF pulsations. The main objection to the concept of cavity modes in the past arises from the lack of experimental evidence of correlation between the frequency spectra of the dayside and nightside signals. This fact is inconsistent with the assumption of the standing wave pattern around the equator (i.e. along the east–west direction) for a spherical cavity. However, this problem can be resolved if one takes into account the geometry of open field lines in the nightside region, namely, assuming that the open field-line region is a perfect absorber of the surface perturbations that are excited in the dayside region of the magnetopause. Therefore, the wave functions in the east–west direction should have a travelling wave form instead. But it poses another problem: if the source of the cavity modes has a broad and continuous wavenumber spectrum in the east–west direction, each eigenmode then has a finite band-width and becomes degenerate. The overlapping of the eigenfrequency spectrum due to the continuous degeneracy of the eigenmodes will eventually smear out the discrete nature of the individual cavity mode.

In order to resolve this problem, we propose a model that considers the magnetospheric cavity to be a resonant filter. Then, only discrete parts of a continuous spectrum of the perturbations that are excited in the magnetopause can couple efficiently to the field-line resonance modes located inside the magnetosphere (Hasegawa, Tsui & Assis 1983). In the formulation of the theory, we use a cylindrical model of the magnetosphere (Radoski 1970, 1976) to analyse the eigenequation of the resonant ULF waves. We will first show that the linearized MHD equations can be combined into an eigenequation form, namely, a single second-order differential equation with non-uniform coefficients. When a plasma mass density profile proportional to $1/r^3$ (Cummings, O'Sullivan & Coleman 1969; Park, Carpenter & Wiggin 1978) is used, it is seen that this equation has, in general, two real turning points along the positive axis. Therefore, the continuity conditions of the eigenfunctions at the turning points will restrict the eigenvalues of the equation to be discrete for a fixed east–west wavenumber and a fixed azimuthal mode number. This is essentially the same concept that eigenvalues become discrete in a potential well as used in quantum mechanics. The eigenmode solutions are undamped functions inside the two turning points in the collisionless case. Additional constraints associated with the preferential cavity modes have been taken into

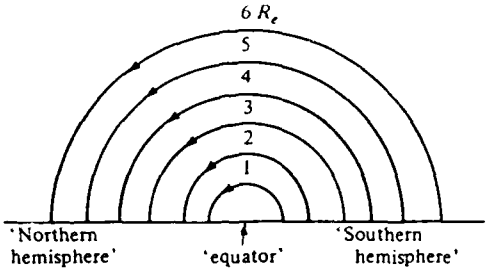

FIGURE 1. Cylindrical magnetospheric model used to study the eigenfrequencies of the resonant ULF waves. $\mathbf{B} = B(r)\hat{\phi}$. The $\hat{z}$ direction, normal to the plane of the figure, is analogous to longitude.

account based on the following facts: (i) the locations of the turning points are a function of both the eigenvalues and the corresponding east–west wavenumbers, and (ii) the perturbations excited in the magnetopause can be efficiently coupled to the inner magnetosphere only when the outer turning point is located near the outer boundary. We shall show in the following analysis that the most likely values of east-west wavenumbers and wave period range can be determined with the present model.

2. Theory and analysis

In a cold plasma, the hydromagnetic wave equations derived from the Maxwell's equations and the fluid equations have the general form of

$$\frac{\partial^2}{\partial t^2}\boldsymbol{\eta} + \frac{1}{4\pi\xi_0}\mathbf{B}_0 \times \{\nabla \times [\nabla \times (\boldsymbol{\eta} \times \mathbf{B}_0)]\} = 0, \tag{1}$$

where $\boldsymbol{\eta}$ is the wave plasma displacement vector, $\mathbf{B}_0$ is the background geomagnetic field, and ξ_0 is the mass density of the plasma.

This wave equation will be solved for a cylindrical model of the magnetosphere. In this model, the earth becomes a flat plane and the magnetic field lines are semicircles as shown in figure 1. In terms of the cylindrical coordinates r, ϕ, z, the geomagnetic field is expressed as $\mathbf{B}_0 = \hat{\phi}B_1/r$, where B_1 is a constant. It is found that (1) has only two non-trivial components (z and r) which correspond to the eigenequations of the toroidal mode and the poloidal mode of the hydromagnetic waves, respectively. These two equations will be shown to couple to each other. If we assume that the transverse wave electric fields vanish at the reflecting points on the conducting earth at $\phi = 0, \pi$ it would be reasonable to use a standing wave expression $\sin n\phi$ for the azimuthal dependence of the perturbations, where the integer n measures the numbers of half-waves along a field line. The z direction corresponds to the longitude. We assume that the surface perturbations excited in the daytime regions of the magnetopause disappear when they propagate toward the nightside regions because of being guided by open field lines. A total absorption boundary condition then requires solutions along the longitude to have the travelling wave form as $\exp[i(k_z z - \omega t)]$ with continuous k_z. Thus we may assume that the

wave perturbations take the form $\eta_r = [F(r)/B_0(r)] \sin n\phi \exp[i(k_z z - \omega t)]$ and $\eta_z = [H(r)/B_0(r)] \sin n\phi \exp[i(k_z z - \omega t)]$, and the two coupled eigenmode equations have the following forms (Radoski 1970, 1976):

$$\left[\left(\frac{\omega}{v_A}\right)^2 - \frac{n^2}{r^2} + \frac{1}{r}\frac{d}{dr} r \frac{d}{dr}\right] F(r) = -ik_z \frac{1}{r}\frac{d}{dr} rH(r), \tag{2}$$

$$\left[\left(\frac{\omega}{v_A}\right)^2 - \frac{n^2}{r^2} - k_z^2\right] H(r) = -ik_z \frac{d}{dr} F(r), \tag{3}$$

where $v_A = B_0/(4\pi\xi_0)^{\frac{1}{2}}$ is the Alfvén speed, and $H(r)$ and $F(r)$ are functions characterizing the radial dependence of the amplitudes of the torodial and poloidal modes, respectively.

From (2) and (3), an eigenequation for the shear magnetic perturbation $G(r) = ik_z rH(r) + r(d/dr) F(r)$ is derived to be

$$\frac{d^2}{dr^2} G - \left[\frac{d}{dr} \ln (rk^2)\right] \frac{d}{dr} G + (k^2 - k_z^2) G = 0, \tag{4}$$

where the notation $k^2 = (\omega/v_A)^2 - n^2/r^2$ is used.

Letting $G(r) = (rk^2)^{\frac{1}{2}} G_1(r)$, equation (4) then reduces to a wave equation with a spatially dependent wave vector given by

$$\frac{d^2}{dr^2} G_1(r) + f(r) G_1(r) = 0, \tag{5}$$

where $$f(r) = k^2 - k_z^2 - \tfrac{1}{4}\alpha^2 + \frac{1}{2}\frac{d}{dr}\alpha \quad \text{and} \quad \alpha = \frac{d}{dr} \ln (rk^2).$$

We now model the outer magnetosphere with a plasma density profile $\xi_0 = \xi_1/r^3$ for $2R_e \leqslant r \leqslant 11R_e$, where ξ_1 is a constant and R_e is the earthradius. In the present paper, the sharp plasma density gradient located at the plasmapause ($r \approx 2-3R_e$) is not taken into account. Thus

$$v_A^2 = \left(\frac{B_1^2}{4\pi\xi_1}\right) r$$

and $$f(r) = \left(\frac{s}{r}\right)\left[1 - \frac{2n^2 + sr}{4(n^2 - sr)^2}\right] - k_z^2 - \frac{n^2}{r^2} + \frac{1}{4r^2}, \tag{6}$$

where $s = 4\pi\xi_1 \omega^2/B_1^2$ is a parameter proportional to the squared eigenfrequency ω.

As shown in figure 2, $f(r)$ has two zeros located at two points r_1 and r_2 on the positive real axis. It implies that (5) has two real positive turning points r_1 and r_2. At the turning points, the wavenumber $f(r)^{\frac{1}{2}}$ becomes zero, thus each of them defines a boundary separating the oscillatory and non-oscillatory parts of the solution of the wave equation. In other words, the wavefunction begins to change its characteristics at the turning point. However, this change must be

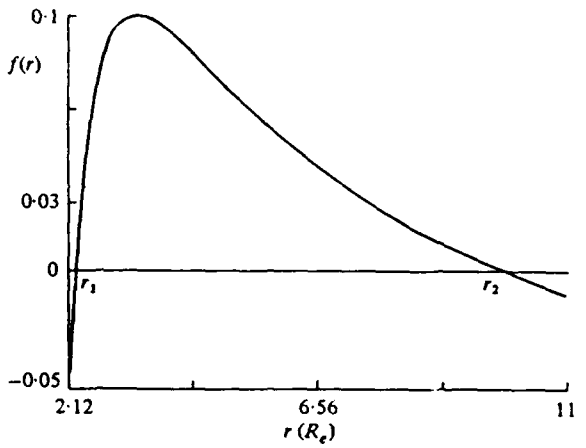

FIGURE 2. Spectral variations of the square of the wavenumber $f(r)$ from $r = 2R_e$ to $r = 11R_e$ where $n = 1$, $k_z = 0{\cdot}32/R_e$ and $s = 1{\cdot}12/R_e$ are used.

compromised by the continuity conditions of the wavefunction and its first derivative at each of the turning points so that the second derivative of the wavefunction can remain finite as imposed by the considered wave equation. The position of the turning points r_1 and r_2 depends on the values of the parameters s, n and k_z. Furthermore $f(r)$ is negative in the region outside the turning points. We find that (5) has solutions for $G(r)$ which are well behaved, namely, they decay exponentially away from the turning points in that region. Thus spatially localized modes exist provided an eigenvalue s (i.e. ω) can be found such that the eigenvalue equation for s (or ω), defined by the Bohr–Sommerfeld quantization condition (Landan & Lifshitz 1965)

$$(m+\tfrac{1}{2})\pi \approx \int_{r_1}^{r_2} f^{\frac{1}{2}}(r)\,dr, \tag{7}$$

can be satisfied, where $m = 0, 1, 2, \ldots$ stands for the number of nodes of the eigenfunction $G_1(r)$ within the two turning points r_1 and r_2.

Equation (7) is solved numerically for s. Since r_1 and r_2 are also functions of s, equation (7) has to be solved self-consistently. Presented in figure 3(*a*) and (*b*) are examples of spatially localized eigenfunctions determined by (5) where (7) has been used to determine first the approximate eigenvalues. For the given values of n and k_z, we find that (7) only has discrete solutions. Moreover, the two turning points have to be located inside the two boundaries taken at $2R_e$ and $11R_e$ of the modelled magnetosphere in order to sustain spatially localized modes. This, in turn, determines the lower bound k_{z1} and the upper bound k_{z2} of the wavenumber k_z. In other words, for a given integral value of n, k_z must be within the interval (k_{z1}, k_{z2}) so that the turning points of (5) determined by each of the solutions of (7) satisfy the conditions $r_1 \geqslant 2R_e$ and $r_2 \leqslant 11R_e$. Figure 4 displays the plots of $f(r)$ for the two extreme cases $k_z = k_{z1}$ and $k_z = k_{z2}$, respectively. We observe that $r_1 > 2R_e$ and $r_2 = 11R_e$ in the first case of $k_z = k_{z1}$ and $s = s_1$, and $r_1 = 2R_e$ and $r_2 < 11R_e$ in the second case of $k_z = k_{z2}$ and $s = s_2$. If the resonant ULF waves in the magnetosphere are assumed to

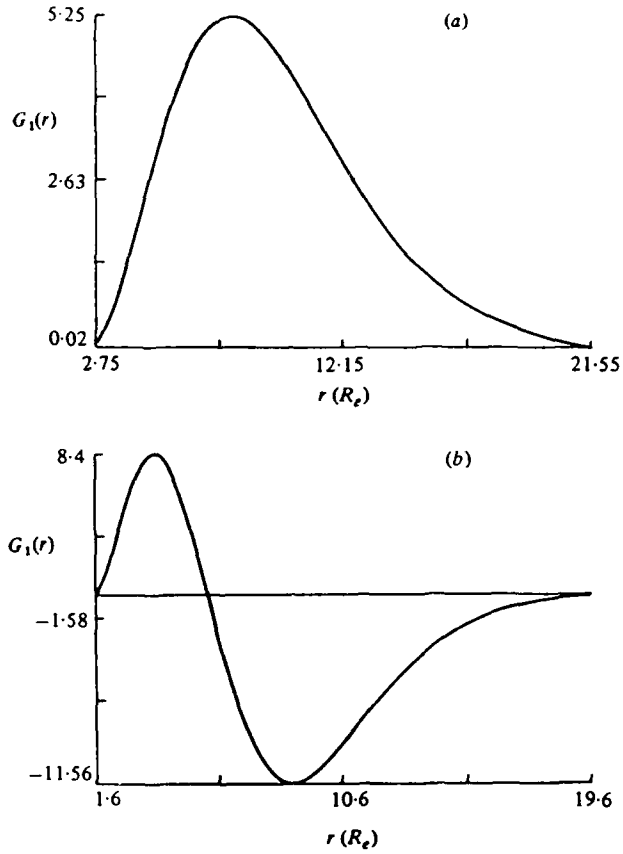

FIGURE 3. Eigenfunctions of the eigenequation (5) for two discrete eigenvalues corresponding to $m = 0$ and 1 of the solutions of (7) for the case of $n = 4$.

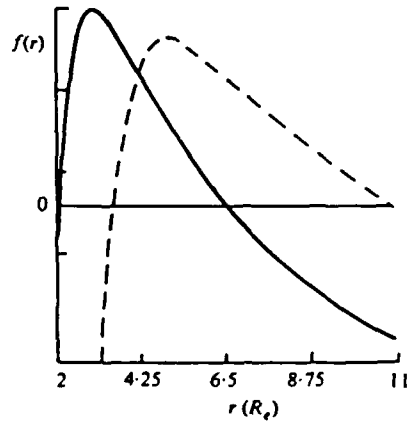

FIGURE 4. Plots of $f(r)$ for two extreme cases $k_z = k_{z1}$ (- - -) and $k_z = k_{z2}$ (——) respectively.

n	m	$\lambda_{z1}(R_e)$	τ_1 (sec)	$\lambda_{z2}(R_e)$	τ_2 (sec)
1	0	21·7	130·3	18·2	119·5
2	0	15·1	87·2	9·0	67·1
3	0	11·9	66·2	6·0	47·0
4	0	9·7	53·1	4·4	35·8
4	1	7·1	40·9	6·0	37·7
5	0	8·3	44·7	3·5	29·1
5	1	6·2	35·4	4·6	30·6
6	0	7·3	38·8	2·8	24·1
6	1	5·6	31·4	3·6	25·3

TABLE 1. Upper and lower bounds of the wave periods and east–west wavelengths of the eigenmodes for azimuthal mode number n from 1 to 6.

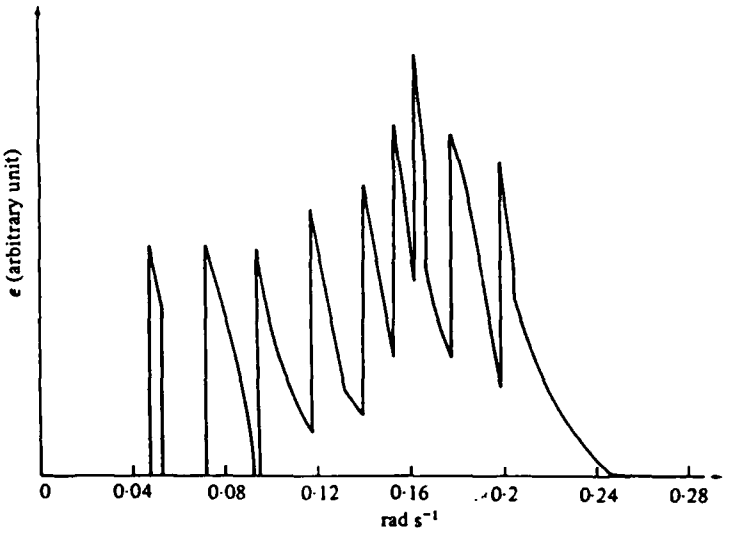

FIGURE 5. Energy spectrum of the magnetospheric cavity modes excited by a source of perturbation with a uniform spectrum in the magnetopause.

arise from the perturbations in the magnetopause, i.e. excited by the Kelvin–Helmholtz instability (Chen & Hasegawa 1974; Southwood 1974), it is quite obvious that the perturbations with parameters corresponding to case one can couple into the magnetosphere more efficiently than that corresponding to case two. This is because in case one the outer turning point is right in the magnetopause, hence the perturbation can be directly propagated into the magnetosphere without tunnelling through a barrier as in case two. Table 1 lists the computed eigenperiod bands for the azimuthal mode number n from 1 to 6. The following $L = 4$ reference parameters: $B_0 = 4{\cdot}86 \times 10^{-3}$ G, $\xi_0 = 6{\cdot}68 \times 10^{-22}$ g cm^{-3}, $R_e = 6{\cdot}4 \times 10^8$ cm are used in the computation (Helliwell & Inan 1982). It shows that the eigenperiod bands for $n = 3$ to 6 overlap with one another. This is because each (n, m) mode has a finite k_z band. Each eigenmode then has a finite band-width and becomes degenerate in the overlapped range of the wave spectrum. However, these modes do not have the same intensities

because their turning points are different. Those having turning points away from the magnetopause, that is the source location of perturbations, have weaker initial intensities weighted by an exponentially decaying factor,

$$\exp\left\{-\int_{r_2}^{11R_e}(-f)^{\frac{1}{2}}dr\right\}.$$

In this factor, f is defined by (6), $11R_e$ is the radial distance of the magnetopause from the centre of the earth and r_2 represents the radial distance of the turning points concerned. As illustrated in figure 5 following table 1, even when the source perturbations in the magnetopause have a uniform spectrum (expressed in an arbitrary unit) in the frequency range of interest, the energy spectrum of the excited cavity modes can have sharp peaks at discrete frequencies in agreement with observations. The discrete nature of the cavity mode spectrum can be, therefore, viewed as the consequence of the following fact. A potential barrier is imposed on the coupling of magnetospheric perturbations (at the magnetopause) into the cavity modes as the outer turning points of the cavity modes do not match the location of the magnetopause. Therefore, in table 1, the values of τ_1 and λ_{z1} are considered to be the most likely periods and east–west wavelengths of the field-line resonances excited in the magnetosphere.

3. Summary

We have theoretically explained the discrete nature of ULF pulsations observed in the magnetosphere by using a cylindrical model (Radoski 1970, 1976). A second-order wave equation is derived to characterize the coupling between the poloidal and toroidal modes of the hydromagnetic waves. When the experimentally determined plasma density radial profile of the '$1/r^3$' form (Cummings *et al.* 1969; Park *et al.* 1978) is used, it is found that the wave equation has two turning points along the radial axis. Undamped eigenfunctions with discrete eigenvalues are found in our collisionless case. They are conceptually analogous to the case that has discrete eigenstates when a particle is trapped by a potential well as discussed in quantum mechanics. However, there is a difference between the two cases. In the present case, $f(r)$ cannot simply be expressed by the difference of a constant eigenenergy and a fixed potential function as in quantum mechanism. This is because the eigenvalues (or ω) are multiplied by a spatially dependent function. Therefore, the potential well determined by $f(r)$ varies with each discrete eigenstate. The eigenfunctions as shown in figure 3(*a*) and (*b*) decay rapidly toward the 'equator'. However, the eigenfunctions still remain finite at $r = 1{\cdot}6R_e$ in the case demonstrated in figure 3(*b*). This means that the pulsations can still be observed at the surface of the earth in the polar regions where they are a distance $\frac{1}{2}\pi R_e$ away from the equator. We have calculated the eigenperiods τ_1 of the most readily excited modes and the most likely values of the east–west wavenumbers λ_{z1} as tabulated in table 1 for illustrative purposes. The wave eigenperiods are calculated to lie in the P_c 3–4 range.

Further work should include the sharp plasma mass density gradient occurring in the inner magnetosphere (plasmapause) together with a realistic

plasma variation for the outer magnetosphere. These results using a cylindrical model should then be modified with a more realistic dipole field model of the earth. Transient time damping of the cavity modes by hot plasmas due to kinetic effects should also be included phenomenologically in the wave equation. In this case, the cavity modes having complex frequencies become damped quasi-modes.

This work is supported by the Air Force Office of Scientific Research, Air Force Systems Command, U.S. Air Force, under Grant No. AFOSR-85-0133, and by the NASA Grant NAG5-725. One of the authors (S.P.K.) wishes to thank Dr H. Radoski for valuable discussions. We are also grateful to Dr A. Hasegawa of AT&T Bell Laboratories for his illuminating comments.

REFERENCES

ALLAN, W. & POULTER, E. M. 1984 *Rev. Geophys. Space Phys.* **22**, 85.

CHEN, L. & HASEGAWA, A. 1974 *J. Geophys. Res.* **79**, 1024 and 1033.

CUMMINGS, W. D., O'SULLIVAN, R. J. & COLEMAN, P. J. 1969 *J. Geophys. Res.* **74**, 778.

HASEGAWA, A., TSUI, K. H. & ASSIS, A. S. 1983 *Geophy. Res. Lett.* **10**, 765.

HELLIWELL, R. A. & INAN, U. S. 1982 *J. Geophys. Res.* **87**, 3537.

KOKUBUM, S. & NAGATA, T. 1965 *Report Ionosph. Space Res.* **19**, 158.

LANDAU, L. D. & LIFSHITZ, E. M. 1965 *Quantum Mechanics: Non-relativistic Theory*, p. 162. Addison-Wesley.

LANZEROTTI, L. J., FUKUNISHI, H., LIN, C. C. & CAHILL, L. J. 1974*a* *J. Geophys. Res.* **79**, 2490.

LANZEROTTI, L. J., FUKUNISHI, H. & CHEN, L. 1974*b* *J. Geophys. Res.* **79**, 4648.

LANZEROTTI, L. J. & SOUTHWOOD, D. J. 1979 *Hydromagnetic Waves, Solar System Plasma Physics* (ed. L. J. Lanzerotti, C. F. Kennel and E. N. Parker), vol. 3, p. 111.

PARK, C. G., CARPENTER, D. L. & WIGGIN, K. B. 1978 *J. Geophys. Res.* **83**, 3137.

RADOSKI, H. R. & MCCLAY, J. F. 1967 *J. Geophys. Res.* **72**, 4899.

RADOSKI, H. R. 1970 *J. Geomagn. Geoelectr.* **22**, 361.

RADOSKI, H. R. 1971 *J. Geomagn. Geoelectr.* **23**, 83.

RADOSKI, H. R. 1973 *J. Geomagn. Geoelectr.* **25**, 363.

RADOSKI, H. R. 1974 *J. Geophys. Res.* **79**, 595.

RADOSKI, H. R. 1976 *Report* AFGL-TR-76-0104.

ROSTOKER, G. 1979 *Geomagnetic Micropulsations, Fundamentals of Cosmic Physics*, vol. 4, p. 211. Gordon and Breach.

SAMSON, J. C., JACKOBS, J. A. & ROSTOKER, G. 1971 *J. Geophys. Res.* **76**, 3675.

SOUTHWOOD, D. J. 1974 *Planet Space Sci.* **22**, 483.

SOUTHWOOD, D. J. & HUGHES, W. J. 1983 *Space Sci. Rev.* **35**, 301.

STUART, W. F., SHERWOOD, V. G. & MACINTOSH, S. M. 1971 *J. Atoms. Terr. Phys.* **33**, 869.

TAKAHASHI, K. & MCPHERRON, R. L. 1982 *J. Geophys. Res.* **87**, 1504.

WALKER, A. D. M. & GREENWALD, R. A. 1981 *J. Geomagn. Geoelectr.* **32** (suppl. II), 111.

JOURNAL OF GEOPHYSICAL RESEARCH, VOL. 93, NO. A1, PAGES 265–269, JANUARY 1, 1988

Thermal Filamentation Instability Driven by the Auroral Electrojet Current

S. P. KUO

Polytechnic University, Farmingdale, New York

M. C. LEE

Massachusetts Institute of Technology, Cambridge

A thermal instability leading to the filamentation of auroral electro-jet currents and giving rise to purely growing magnetic field-aligned density irregularities in the *E* region of the high-latitude ionosphere is investigated. The physical process of the instability is through the modification of the electron-neutral collision frequency due to the electron temperature perturbation in the electrojet. A dispersion relation of the instability is derived, from which the threshold electrojet current and the growth rate of the instability are determined. It is found that they become independent of the scale sizes of the irregularities for scale sizes larger than about 13 m. The proposed instability can, thus, be considered to be one of the mechanisms responsible for those observed relatively large-scale *E* region irregularities (Pfaff et al., 1984).

1. INTRODUCTION

The high-latitude ionosphere is constantly structured in the ionospheric irregularities, (see, for example, *Kelley and Mozer* [1973], *Phelps and Sagalyn* [1976], *Rino et al.* [1978], *Vickrey et al.* [1980], *Weber et al.* [1984], and *Weber and Buchan* [1985]. The appearance of these density irregularities has generally been attributed to the excitation of plasma instabilities. These include the Farley-Buneman two stream instability [*Farley*, 1963], and the **E** × **B** and current-convective instabilities [*Ossakow and Chaturvedi*, 1979; *Keskinen and Ossakow*, 1983; *Mitchell et al.*, 1985]. Recently, *Weber et al.* [1984] and *Cerisier et al.* [1985] have invoked the **E** × **B** instability, and *Das and Das* [1983] and *Lee* [1984] have proposed thermal instability to explain large scale density fluctuations in the *F* layer of the high latitude ionosphere, and *Chaturvedi et al.* [1987] have considered the parallel current effects on the onset of the Farley-Buneman instability in the auroral *E* region. A comprehensive review of ionospheric irregularities excited by some instabilities has been published in *Review of Geophysics* by *Fejer and Kelley* [1980], and in Radio Science by *Keskinen and Ossakow* [1983]. Both large and small-scale irregularities have been observed from the *E* and *F* layers of the high-latitude ionosphere. The Farley-Buneman instability driven by electrojet currents is known to be effective in generating meter and shorter-scale irregularities of type *I* in the *E* region. This instability has been extensively investigated by radar techniques. The irregularities of type II are of slightly larger scale sizes and are generated through the **E** × **B** gradient drift instability. However, the growth rate of the two stream instability as well as of the gradient drift instability is a function of the angle between the wavevector and the direction of the electron drift. The growth rate becomes zero when the wavevector is perpendicular to the drift direction. It is therefore not able to explain the radar observations in the direction perpendicular to the drift motion by using the linear two stream instability mechanism. A two-dimensional nonlinear theory [*Sudan et al.*, 1973] has, thus, been proposed to explain the presence of the type II gradient drift irregularities with wavelengths and propagation directions that are predicted to be linearly damped. Furthermore, the temporal and spatial power spectrum of the irregularities in the equatorial electrojet have also been computed [*Keskinen et al.*, 1979] from simulations of the two-dimensional model. The results are found to compare favorably with several 9-m type II radar spectra taken in the daytime equatorial electrojet [*Balsley and Farley*, 1971]. However, in the analyses of these instabilities, energy equations are not incorporated because plasma temperature perturbations can be ignored in these instability processes.

If the ohmic dissipation of electrojet currents is taken into account, we expect that a new instability caused by the thermal effect may be excited. In this paper, we study this new mechanism for the generation of irregularities in the auroral electrojet under the condition that the electron drift speed exceeds 3 times the ion acoustic speed. This thermal instability, will be shown also to produce relatively large-scale (greater than tens of meters) *E* region irregular structures which are polarized perpendicular to the drift motion. It is then contributed additively to the nonlinear gradient drift instability. This instability is first analyzed analytically and described in section 2, in which the dispersion relation of the instability is presented. This dispersion relation is analyzed to determine the threshold and growth rate of the instability. The results are presented in section 3. Conclusions and general remarks are given in section 4.

2. DISPERSION RELATION

We study the thermal instability excited by the background electrojet current. The vector orientation of Figure 1 is considered, where $\mathbf{E}_0 = \hat{x}E_0$ is the dc driving field of the electrojet current and $\mathbf{B}_0 = -\hat{z}B_0$ is the geomagnetic field. Hence the background Pederson (x component) and Hall (y component) current densities are given respectively by

$$J_{x0} = -en_0(v_{e0x} - v_{i0x}) = (n_0e^2/m) \cdot [\nu_e/(\nu_e^2 + \Omega_e^2) + (m/M)\nu_i/(\nu_i^2 + \Omega_i^2)]E_0 \quad (1)$$

Paper number 6A8889.
0148-0227/88/006A-8889$02.00

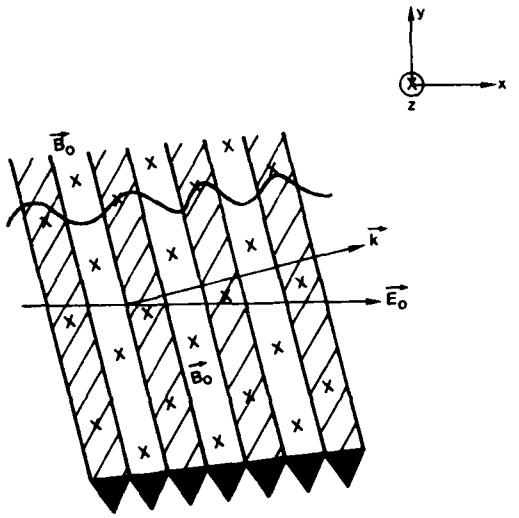

Fig. 1. Filamentation of electrojet current by thermal instability.

$$J_{y0} = -en_0(v_{e0y} - v_{i0y}) = -(n_0e^2/m)$$
$$\cdot[\Omega_e/(\nu_e^2 + \Omega_e^2) - (m/M)\Omega_i/(\nu_i^2 + \Omega_i^2)]E_0 \quad (2)$$

where $m(M)$, $\nu_e(\nu_i)$ and $\Omega_e(\Omega_i)$ are the electron (ion) mass, unperturbed collision frequency and cyclotron frequency respectively; n_0 is the background plasma density; $\mathbf{v}_{e0} = -[(eE_0/m)/(\nu_e^2 + \Omega_e^2)](\hat{x}\nu_e - \hat{y}\Omega_e)$ and $\mathbf{v}_{i0} = [(eE_0/M)/(\nu_i^2 + \Omega_i^2)](\hat{x}\nu_i + \hat{y}\Omega_i)$.

In the presence of thermal fluctuations, the plasma density and the electron temperature of the electrojet are perturbed. In terms of the unperturbed quantities n_0 and T_{e0}, the total density n and the electron temperature T_e are expressed as $n = n_0 + \delta n$ and $T_e = T_{e0} + \delta T_e$, where the quasineutrality is assumed so that $\delta n_e = \delta n = \delta n_i$ and δn and δT_e are the density and temperature pertubations, respectively. These perturbations are, in turn, to introduce modifications on electron collision frequency and the plasma conductivity. Since the electron collisions are dominated by the electron neutral collision in the E region, the collision frequency $\tilde{\nu}_e$ is proportional to the square root of the electron temperature and can be expanded up to the lowest order temperature perturbation as $\tilde{\nu}_e \approx \nu_e(1 + \frac{1}{2}\delta T_e/T_{e0})$. The conductivity will also be expanded up to the lowest order density and temperature perturbations in a similar way. With the aid of these expansions and assuming that the linearized perturbations bear the general form $\delta P = \delta P e^{i\mathbf{k}\cdot\mathbf{r}}e^{\gamma t}$ having real positive γ as the growth rate of the field-aligned purely growing mode and $\mathbf{k} = \hat{x}k_x + \hat{y}k_y$ perpendicular to the magnetic field, the transport equations given by *Braginskii* [1965] are linearized to be

$$\mathbf{k}\cdot(\delta\mathbf{v}_e - \delta\mathbf{v}_i) = -(\delta n/n_0)\mathbf{k}\cdot\mathbf{u}_0 \quad (3)$$

$$\mathbf{k}\cdot\delta\mathbf{v}_i = (i\gamma - \mathbf{k}\cdot\mathbf{v}_{i0})(\delta n/n_0) \quad (4)$$

obtained from the electron and ion continuity equations, where $\mathbf{u}_0 = \mathbf{v}_{e0} - \mathbf{v}_{i0}$,

$$\nu_{en}\mathbf{k}\cdot\delta\mathbf{v}_e - \Omega_e k\times\delta\mathbf{v}_e\cdot\hat{z} = -i(k^2/m)(\delta T_e + T_{e0}\delta n/n_0) - \tfrac{1}{2}\nu_{en}\mathbf{k}\cdot\mathbf{v}_{en}(\delta T_e/T_{e0})$$

$$\Omega_e\mathbf{k}\cdot\delta\mathbf{v}_e + \nu_{en}\mathbf{k}\times\delta\mathbf{v}_e\cdot\hat{z} = -\tfrac{1}{2}\nu_{en}(\mathbf{k}\times\mathbf{v}_{e0}\cdot\hat{z})(\delta T_e/T_{e0}) \quad (5)$$

$$\nu_{en}\mathbf{k}\cdot(\delta\mathbf{v}_e - \delta\mathbf{v}_i) + (M/m)\bar{\nu}_{in}\mathbf{k}\cdot\delta\mathbf{v}_i - \Omega_e\mathbf{k}\times(\delta\mathbf{v}_e - \delta\mathbf{v}_i)\cdot\hat{z}$$
$$= -i(k^2/m)[\delta T_e + (T_{e0} + T_i)(\delta n/n_0)] - \tfrac{1}{2}\nu_{en}(\mathbf{k}\cdot\mathbf{v}_{e0})(\delta T_e/T_{e0}) \quad (6)$$

$$\Omega_e\mathbf{k}\cdot(\delta\mathbf{v}_e - \delta\mathbf{v}_i) + \nu_{en}\mathbf{k}\times(\delta\mathbf{v}_e - \delta\mathbf{v}_i)\cdot\hat{z} + (M/m)\bar{\nu}_{in}\mathbf{k}\times\delta\mathbf{v}_i\cdot\hat{z}$$
$$= -\tfrac{1}{2}\nu_{en}(\hat{z}\cdot\mathbf{k}\times\mathbf{v}_{e0})(\delta T_e/T_{e0}) \quad (7)$$

obtained from the electron and ion momentum equations, where $\bar{\nu}_{in} = \nu_{in} + (m/M)\nu_{en} + \gamma + i\mathbf{k}\cdot\mathbf{v}_{i0}$, and

$$(\gamma + i\mathbf{k}\cdot\mathbf{v}_{e0})\delta T_e + i\tfrac{2}{3}T_{e0}\mathbf{k}\cdot\delta\mathbf{v}_e$$
$$= -\nu_{en}(k^2v_{te}^2/\Omega_e^2)\delta T_e - (m/M_n)\nu_{en}(3 - T_n/T_{e0})\delta T_e$$
$$+ (2/3n_0)\delta(Q_{f\gamma}) - 2(m/M_n)\nu_{en}(T_{e0} - T_n)(\delta n/n_0) \quad (8)$$

derived by the electron thermal diffusion equation, where $v_{te} = (T_{e0}/m)^{1/2}$ and the differential ohmic heating source $\delta(Q_{f\gamma}) = \delta(J^2/n\sigma_\perp{}^*)$, with $\sigma_\perp{}^* = (1/\sigma + M\Omega_i^2/ne^2\bar{\nu}_{in})^{-1}$ and $\sigma = ne^2/m\bar{\nu}_{en}$ [*Braginskii*, 1965], is given by

$$\frac{1}{n_0}\delta(Q_{f\gamma}) = (u_0/v_{te})^2[\tfrac{1}{2}\nu_{en}\delta T_e - T_{e0}(\nu_{en} + \Omega_e\Omega_i/\nu_{in})(\delta n/n_0)]$$
$$+ (m/n_0{}^2e^2)(\nu_{en} + \Omega_e\Omega_i/\nu_{in})\delta J^2 \quad (9)$$

We can further express

$$\delta J^2 = 2J_0{}^2(\delta n/n_0) - 2en_0\mathbf{J}_0\cdot(\delta\mathbf{v}_e - \delta\mathbf{v}_i)$$
$$= 2J_0{}^2(\delta n/n_0) + 2e^2n_0{}^2\{(\mathbf{k}\cdot\mathbf{u}_0)[\mathbf{k}\cdot(\delta\mathbf{v}_e - \delta v_i)]$$
$$+ (\hat{z}\cdot\mathbf{k}\times\mathbf{u}_0)[\hat{z}\cdot\mathbf{k}\times(\delta\mathbf{v}_e - \delta\mathbf{v}_i)]\}/k^2 \quad (10)$$

Solving (5)–(7) yields

$$\mathbf{k}\cdot(\delta\mathbf{v}_e - \delta\mathbf{v}_i) = \{[(m\nu_{en} - M\bar{\nu}_{in})a_1 + m\Omega_e c_1](\delta T_e/T_{e0})$$
$$+ [(m\nu_{en} - M\bar{\nu}_{in})b_1 - m\Omega_e d_1]$$
$$\cdot(\delta n/n_0)\}/[m\nu_{en} - M\bar{\nu}_{in})^2 + m^2\Omega_e{}^2] \quad (11)$$

and

$$\mathbf{k}\times(\delta\mathbf{v}_e - \delta\mathbf{v}_i)\cdot\hat{z} = \{[(m\nu_{en} - M\bar{\nu}_{in})c_1 - m\Omega_e a_1](\delta T_e/T_{e0})$$
$$- [(m\nu_{en} - M\bar{\nu}_{in})d_1 + m\Omega_e b_1]$$
$$\cdot(\delta n/n_0)\}/[(m\nu_{en} - M\bar{\nu}_{in})^2 + m^2\Omega_e{}^2] \quad (12)$$

where

$$a_1 = -ik^2T_{e0} - \tfrac{1}{2}m\nu_{en}\mathbf{k}\cdot\mathbf{v}_{e0} + [(M\nu_{in}/m(\nu_{en}^2 + \Omega_e^2)](a\nu_{en} + c\Omega_e)$$
$$b_1 = -ik^2(T_{e0} + T_i) + [M\nu_{in}\nu_{en}/m(\nu_{en}^2 + \Omega_e^2)]b$$
$$c_1 = -\tfrac{1}{2}m\nu_{en}\hat{z}\cdot\mathbf{k}\times\mathbf{v}_{e0} + [M\nu_{in}/m(\nu_{en}^2 + \Omega_e^2)](c\nu_{en} - a\Omega_e) \quad (13)$$
$$d_1 = [M\nu_{in}\Omega_e/m(\nu_{en}^2 + \Omega_e^2)]b$$

and

$$a = ik^2T_{e0} + \tfrac{1}{2}m\nu_{en}\mathbf{k}\cdot\mathbf{v}_{e0}$$
$$b = ik^2T_{e0}$$
$$c = \tfrac{1}{2}m\nu_{en}\mathbf{k}\times\mathbf{v}_{e0}\cdot\hat{z}$$

From (3) and (11), we have

$$\{\mathbf{k}\cdot\mathbf{u}_0 + [(m\nu_{en} - M\bar{\nu}_{in})b_1 - m\Omega_e d_1]/[(m\nu_{en} - M\bar{\nu}_{in})^2 + m^2\Omega_e{}^2]\}$$
$$\cdot(\delta n/n_0) = -\{[m\nu_{en} - M\bar{\nu}_{in})a_1 + m\Omega_e c_1]/[(m\nu_{en} - M\bar{\nu}_{in})^2$$
$$+ m^2\Omega_e{}^2]\}(\delta T_e/T_{e0}) \quad (15)$$

substituting (9) into (8), and with the aid of (4), (5), (10), (11),

(12), and (15), the dispersion relation for the filamentation instability of the electrojet is derived to be

$$\gamma + i\mathbf{k}\cdot\mathbf{v}_{e0} - \tfrac{1}{3}\nu_{en}[(u_0/v_{te})^2 - 5k^2v_{te}^2/\Omega_e^2 - 3(m/M_n)(3 - T_n/T_{e0})] - i\,\tfrac{1}{3}(\nu_{en}/\Omega_e)[(\nu_{en}/\Omega_e)\mathbf{k}\cdot\mathbf{v}_{e0} + \mathbf{k}\times\mathbf{v}_{e0}\cdot\hat{z}]$$
$$= \tfrac{4}{3}\nu_{en}\{[(k^2v_{te}^2/2\Omega_e^2) + (3m/2M_n)(1 - T_n/T_{e0}) + (1 + \Omega_e\Omega_i/\nu_{en}\nu_{in})\cdot[(\mathbf{k}\cdot\mathbf{u}_0/k\nu_{te})^2 - \tfrac{1}{2}(u_0/v_{te})^2]\}[(m\nu_{en} - M\nu_{in})a_1 + m\Omega_e c_1]$$
$$+ (1 + \Omega_e\Omega_i/\nu_{en}\nu_{in})[(\hat{z}\cdot\mathbf{k}\times\mathbf{u}_0)/k^2v_{te}^2]\cdot\{(\mathbf{k}\cdot u_0)[(m\nu_{en} - M\nu_{in})c_1 - m\Omega_e a_1]$$
$$+ (b_1c_1 + a_1d_1)]\}/\{(\mathbf{k}\cdot\mathbf{u}_0)[(m\nu_{en} - M\bar{\nu}_{in})^2 + m^2\Omega_e^2] + [(m\nu_{en} - M\bar{\nu}_{in})b_1 - m\Omega_e d_1]\} \quad (16)$$

This equation will be solved in the following to determine the threshold electrojet current and the growth rate of the instability, and the filamentation direction of the electrojet. The thermal source of the instability is given by the ohmic loss of the electrojet current manifested by terms proportional to $\nu_{en}(v_{e0} - v_{i0})^2$. Collision and diffusion losses impose a threshold condition of the instability.

3. Results

Equation (16) is complex which can then be broken up into two real equations. While the real part of (16) determines the growth rate, the imaginary part of (16) defines the direction of filamentation instability. These two equations are given, respectively, to be

$$\gamma \cong \tfrac{1}{3}\nu_{en}[(u_0/v_{te})^2 - 5k^2v_{te}^2/\Omega_e^2 - 9(m/M_n)(1 - T_n/3T_{e0})] + \tfrac{1}{3}\nu_{en}^2\nu_{in}^2/\Omega_e)\{-(k^2v_{te}^2/\Omega_e^2) - (3m/M_n)(1 - T_n/T_{e0}) + (u_0/v_{te})^2 + 2(\Omega_e\Omega_i^2/\nu_{en}\nu_{in}^2)[(\Omega_i/\nu_{in})(\mathbf{k}\cdot\mathbf{u}_0)^2 - (\mathbf{k}\cdot\mathbf{u}_0)(\hat{z}\cdot\mathbf{k}\times\mathbf{u}_0)]/k^2v_{te}^2\}\cdot(\hat{z}\cdot\mathbf{k}\times\mathbf{v}_{e0})/[\nu_{in}^2 + \Omega_i^2)(\mathbf{k}\cdot\mathbf{u}_0)] \quad (17)$$

and

$$(\mathbf{k}\cdot\mathbf{v}_{e0})[1 - \tfrac{1}{3}(\nu_{en}/\Omega_e)^2] - \tfrac{1}{3}(\nu_{en}/\Omega_e)(\hat{z}\cdot\mathbf{k}\times\mathbf{v}_{e0}) \cong \tfrac{4}{3}[\nu_{en}^2\nu_{in}^2/\Omega_e\Omega_i(\nu_{in}^2 + \Omega_i^2)]\cdot(1 + \Omega_e\Omega_i/\nu_{en}\nu_{in})(\hat{z}\cdot\mathbf{k}\times\mathbf{v}_{e0})(\hat{z}\cdot\mathbf{k}\times\mathbf{u}_0)/(\mathbf{k}\cdot\mathbf{u}_0) + \tfrac{4}{3}(\nu_{en}/\Omega_e)(1 + \Omega_e\Omega_i/\nu_{en}\nu_{in})(\hat{z}\cdot\mathbf{k}\times\mathbf{u}_0) \quad (18)$$

where we have approximated $\bar{\nu}_{in}$ by ν_{in}, i.e., $|\gamma + (m/M)\nu_{en} + i\mathbf{k}\cdot\mathbf{v}_{i0}| \ll \nu_{in}$ is assumed, and neglected the ion thermal effect, simplify the resultant equations.

In the quantitative analysis, we generally assume uneven electron temperature (T_{e0}) and neutral temperature ($T_n \sim T_{i0} \sim 300$ K), and the following E region parameters: $\nu_{en} = 5 \times 10^4\,s^{-1}$, $\nu_{in} = 3 \times 10^3\ s^{-1}$, $\Omega_i = 159\ s^{-1}$, $\Omega_e = 8.8 \times 10^6\ s^{-1}$, $M_n(NO^+)/m = 5.52 \times 10^4$, and $v_{te} = (T_{e0}/T_n)^{1/2}6.74 \times 10^4$ m/s will be used.

We first analyze (18) to determine the filamentation direction, i.e., the direction of $\mathbf{k}$. With the aid of (10) and (2), and using the E region parameters for simplifying the result, we obtained

$$\theta = \tan^{-1}(k_y/k_x) \approx \tan^{-1}[4\nu_{in}\Omega_i/(3\nu_{in}^2 - \Omega_i^2)] \quad (19)$$

From (1) and (2), the direction of the electrojet current is also obtained to be

$$\theta_0 = \tan^{-1}(J_{y0}/J_{x0}) \approx -\tan^{-1}(\nu_{in}/\Omega_i) \quad (20)$$

consequently, it is found

$$\theta - \theta_0 \cong -\tan^{-1}(3\nu_i/\Omega_i) \approx -\pi/2 \quad (21)$$

We have thus shown that the result of thermal instability is developing the current filaments along the electrojet current. The excited instability is both magnetic field aligned and electrojet current aligned. This feature is the characteristic nature of the filamentation instability that is associated with purely growing (i.e., zero real frequency) mode. If the excited mode is not electrojet current aligned, this mode then has finite frequency determined by $\mathbf{k}\cdot\mathbf{u}_0$. It is found that higher threshold is required for excited nonpurely growing mode. Therefore, the physical reason for proposed instability to be electrojet current-aligned in addition to magnetic field-aligned is that it meets the minimim threshold for its excitation.

We next use (19) for the direction of $\mathbf{k}$, (17) then becomes

$$\gamma \equiv \tfrac{1}{3}\nu_{en}\{(u_0/v_{te})^2[(40\Omega_i^4 + 7\Omega_i^2\nu_{in}^2 + 9\nu_{in}^4)/(\Omega_i^2 + \nu_{in}^2)\cdot(16\Omega_i^2 + 9\nu_{in}^2) + 3\nu_{en}\nu_{in}^3/\Omega_e\Omega_i(\Omega_i^2 + \nu_{in}^2)] - 5(kv_{te}/\Omega_e)^2 - 9(m/M_n)(1 - T_n/3T_e)\cdot[1 + \nu_{en}\nu_{in}^3/\Omega_e\Omega_i(\nu_{in}^2 + \Omega_i^2)]\} \quad (22)$$

Using the E region parameters, we can express (22) as

$$\gamma \sim 1.19[(u_0/v_s)^2 - (T_{e0}/T_n)(162/\lambda^2) - 2.52(1 - T_n/3T_{e0})] \quad (23)$$

where $v_s = (3T_{e0}/M_n)^{1/2} \sim 500\,(T_{e0}/T_n)^{1/2}$ m/s.

The threshold condition obtained from (23) by letting $\gamma = 0$ is found to be

$$u_{0th} \sim [(T_{e0}/T_n)(162/\lambda^2) + 2.52(1 - T_n/3T_{e0})]^{1/2}v_s \quad (24)$$

It is a functional dependence of T_{e0}/T_n. In observations, T_{e0}/T_n is, usually, less than 5 (R. Pfaff, private communication, 1987). We therefore limit our analyses in the following for $T_{e0}/T_n \le 5$.

Figure 2 presents the relation between the threshold drift speed u_{0th} and the scale length λ of the thermal instability. It shows that u_{0th}/v_s quickly approaches to a minimum about 1.55 for $\lambda > 30$ m in both $T_{e0}/T_n = 2$ and 5 cases.

The dependences of the growth rate γ on the scale length are shown in Figure 3 for two cases in corresponding with Figure 2. We first consider the case $T_{e0}/T_n = 2$ and assume

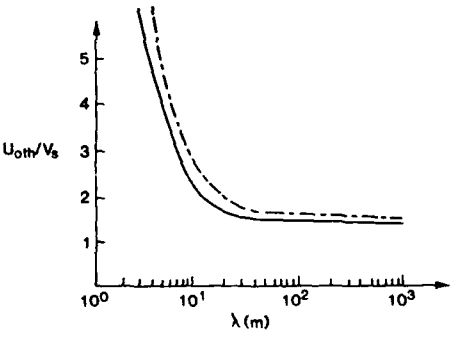

Fig. 2. Threshold drift speed versus the scale length of the thermal instability, where $T_{e0}/T_n = 2$ and $v_s \sim 707$ m/s (solid line) and $T_{e0}/T_n = 5$ and $v_s \sim 1120$ m/s (dashed line) are assumed.

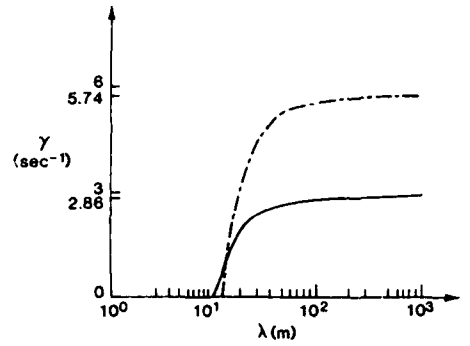

Fig. 3. Growth rate versus the scale length of the irregularity, where the solid line represents the case $E_0 = 75$ mV/m, $u_0 = 1.5$ km/s, and $T_{e0}/T_n = 2$, and the dashed line stands for the case $E_0 = 150$ mV/m, $u_0 = 3$ km/s, and $T_{e0}/T_n = 5$.

that $u_0 = 1.5$ km/s corresponding to a dc driving field $E_0 = 75$ mV/m. In this case, only perturbations with scale lengths larger than 11.5 m can be excited. The growth rate quickly reaches a maximum 2.86 s^{-1} for $\lambda > 30$ m. We next consider a strong electrojet current case with $E_0 = 150$ mV/m and $u_0 = 3$ km/s. strong ohmic heating leads to large T_{e0}/T_n and a ratio 5 is thus assumed. The minimum scale length of the instability increases only slightly to 13 m. However, the maximum growth rate increases to about twice the previous case.

4. Discussion and Conclusion

We have shown that a thermal instability can be excited when the electrojet currents are intense enough. This instability can cause the filamentation of the electrojet currents and gives rise to tens to hundreds of meters E region irregularities. The physical process of the instability is through the modification of the electron-neutral collision frequency due to the electron temperature perturbation in the electrojet. The collision frequency increases with the temperature perturbation. This, in turn, further increases the ohmic loss of the electrojet currents. A thermal instability is thus excited through such a positive feedback process. Here we have considered a magnetoplasma, and hence the heat conduction in the direction perpendicular to the magnetic field is greatly reduced. In this case instability becomes favorable to be excited in magnetic field-align structure and the heat transport processes are essentially determined by the collisional coupling between electrons and neutrals. Electron gas absorbs the energy from the heat source and dumps a fraction of it to the neutrals. For scale sizes larger than about 13 m, the diffusion loss can be neglected and thus the threshold and the growth rate of the instability become independent of the scale sizes of the irregularities.

We also note that unequal electron and neutral temperature in the high-latitude ionosphere were observed [*Schlegel and St.-Maurice*, 1981; *Wickwar et al.*, 1981; *Stauning*, 1984]. Ohmic dissipation of the electrojet current may be partly responsible for the elevated electron temperature. High thresholds are required for the instability because of the additional damping imposed by $T_{e0} > T_n$ condition as shown in Figure 2. The threshold can be exceeded at high latitude when intense electrojet currents are present. Hundred-meter scale irregularities can be excited by the thermal instability in less than a second. Once the threshold conditions are met for the thermal instability, the Farley-Buneman instability can be strongly excited in much shorter time scale (millisecond). This is because the threshold of the Farley-Buneman instability is much lower than that of the proposed thermal instability. It has been shown [*Ossakow et al.*, 1975] that the effects of finite $k_{\parallel}$ should also be considered in determining the maximum growth rate of the Farley-Buneman instability for such large transverse currents. However, we don't expect, in reality, that the relative drift speed can be too much larger than the threshold drift of the thermal instability. Therefore the proposed instability will prefer to operate for the case of minimum threshold ($k_{\parallel} = 0$) instead, so that the diffusion damping is minimized. Though the proposed instability for generating large scale irregularities has much smaller growth rate than that of the Farley-Buneman instability, it does not imply that the proposed instability will not have significant impact regarding the ionospheric disturbances. On the contrary, the perturbations introduced by the large-scale field-aligned density irregularities to the ionosphere are believed to be important by the facts that the large scale field-aligned density irregularities usually have high saturation levels (e.g., fluctuations in a few percent of the background density have often been observed in the HF heating experiments), and can stay for a very long period of time even after the driving force is removed. While our proposed thermal instability can be developed in less than a second, $\mathbf{E} \times \mathbf{B}$ instability that can also excite large scale irregularities takes a few tens of seconds for its development.

The excited hundred meter scale ionospheric irregularities should then be able to cause spread E echoes in ionograms. Also, in the absence of F region irregularities, these E region irregularities may still cause amplitude and phase scintillations of beacon satellite signals. These phenomena can be experimentally studied with coordinated incoherent scatter radar, ionosonde, and scintillation measurement techniques. In addition to the distinct difference in scale lengths, the irregularities induced by the proposed mechanism are purely growing modes (i.e., zero real frequency), while those excited by the Farley-Buneman instability have real frequencies.

Acknowledgments. This work was supported jointly by AFOSR grant AFOSR-85-0133 and NSF grants ATM-8315322 and ATM 87-13217 at the Polytechnic University and by NASA grants NAG-5-889 and P.O. S-56148-D at the Massachusetts Institute of Technology. One of us (M. C. L.) thanks R. F. Pfaff for useful discussions.

The Editor thanks two referees for their assistance in evaluating this paper.

References

Balsley, B. B., and D. T. Farley, Radar studies of the equatorial electrojet at three frequencies, *J. Geophys. Res.*, *76*, 8341, 1971.

Braginskii, S. I., Transport process in a plasma, in *Reviews of Plasma Physics*, Vol. I, edited by M. A. Leontovich, 205 pp., Consultant's Bureau, New York, 1965.

Cerisier, J. C., J. J. Berthelier, and C. Beghin, Unstable density gradients in the high-latitude ionosphere, *Radio Sci.*, *20*, 755, 1985.

Chaturvedi, P. K., J. D. Huba, S. L. Ossakow, P. Satyamarayana, and J. A. Fedder, Parallel current effects on two-stream electrojet plasma instabilities, *J. Geophys. Res.*, *92*, 8700, 1987.

Das, U. N., and A. C. Das, Generation of ionospheric irregularities by thermal-source: A new mechanism, *Planet. Space Sci.*, *31*, 311, 1983.

Farley, D. T., A plasma instability resulting in field-aligned irregularities in the ionosphere, *J. Geophys. Res.*, *68*, 6083, 1963.

Fejer, B. G., and M. C. Kelley, Ionospheric irregularities, *Rev. Geophys.*, *18*, 401, 1980.

Kelley, M. C., and F. S. Mozer, Electric field and plasma density fluctuations due to high-frequency Hall current two stream instability in the auroral E region, *J. Geophys. Res.*, *78*, 2214, 1973.

Keskinen, M. J., and S. L. Ossakow, Theories of high-latitude ionospheric irregularites: A review, *Radio Sci.*, *18*, 1077, 1983.

Keskinen, M. J., R. N. Sudan, and R. L. Ferch, Temporal and spatial power spectrum studies of numerical simulations of type II gradient drift irregularities in the equatorial electrojet, *J. Geophys. Res.*, *84*, 1419, 1979.

Lee, M. C., Ohmic dissipation of Pederson current as the cause of high-latitude *F* region ionospheric irregularities, *J. Geophys. Res.*, *89*, 2289, 1984.

Mitchell, H. G., Jr., J. A. Fedder, M. J. Keskinen, and S. T. Zalesak, A simulation of high latitude *F* layer instabilities in the presence of magnetosphere-ionosphere coupling, *Geophys. Res. Lett.*, *12*, 283, 1985.

Ossakow, S. L., and P. K. Chaturvedi, Current convective instability in the diffuse aurora, *Geophys. Res. Lett.*, *6*, 332, 1979.

Ossakow, S. L., K. Papadopoulos, J. Orens, and T. Coffey, Parallel propagation effects on the type I electrojet instability, *J. Geophys. Res.*, *80*, 141, 1975.

Pfaff, R. F., M. C. Kelley, B. G. Fejer, E. Kudeki, C. W. Carlson, A. Pedersen, and B. Hausler, Electric field and plasma density measurements in the auroral electrojet, *J. Geophys. Res.*, *89*, 236, 1984.

Phelps, A. D. R., and R. C. Sagalyn, Plasma density irregularities in the high-latitude topside ionosphere, *J. Geophys. Res.*, *81*, 515, 1976.

Rino, C. L., R. C. Livingston, and S. J. Matthews, Evidence for sheet like auroral ionospheric irregularities, *Geophys. Res. Lett.*, *5*, 1034, 1978.

Schlegel, K., and J. P. St.-Maurice, Anomalous heating of the polar *E* region by unstable plasma waves, 1, Observations, *J. Geophys. Res.*, *86*, 1447, 1981.

Stauning, P., Absorption of cosmic noise in the *E* region, *Geophys. Res. Lett.*, *11*, 1184, 1984.

Sudan, R. N., J. Akinrimisi, and D. T. Farley, Generation of small-scale irregularities in the equatorial electrojet, *J. Geophys. Res.*, *78*, 240, 1973.

Vickrey, J. F., C. L. Rino, and T. A. Potemra, Chatanika/triad observations of unstable ionization enhancement in the auroral *F* region, *Geophys. Res. Lett.*, *7*, 789, 1980.

Weber, E. J., and J. Buchan, Observation of plasma structure and transport at high latitude, in *The Polar Cusp*, edited by J. A. Holtet and A. Egeland, p. 279, D. Reidel, Hingham, Mass., 1985.

Weber, E. J., J. Buchau, J. G. Moore, J. R. Sharber, R. C. Livingston, J. D. Winningham, and B. W. Reinisch, *F* layer ionization patches in the polar cap, *J. Geophys. Res.*, *89*, 1683, 1984.

Wickwar, V. B., C. Lathuillers, W. Kofman, and G. Lejeune, Electrical electron temperatures in the auroral *E* layer measured with the chatanika radar, *J. Geophys. Res.*, *86*, 4721, 1981.

S. P. Kuo, Polytechnic University, Long Island Center, Route 110, Farmingdale, NY 11735.

M. C. Lee, Massachusetts Institute of Technology, Cambridge, MA 02139.

(Received December 18, 1986;
revised September 22, 1987;
accepted September 24, 1987.)

Filamentation Instability of Large-Amplitude Alfven Waves

S.P. Kuo and M.H. Whang

Polytechnic University, Route 110, Farmingdale, N.Y. 11735

M.C. Lee

Massachusetts Institute of Technology, Cambridge, MA. 02139

Abstract

An instability that leads to the filamentation of large-amplitude Alfven waves and gives rise to purely growing density and magnetic field fluctuations is studied. The dispersion relation of the instability is derived, from which the threshold conditions and the growth rates of the instability are analyzed quantitatively for applications to the solar wind plasma. We have examined their dependence on the filamentation spectrum, the plasma β, and the pump frequency and intensity for both right-hand and left-hand circularly polarized Alfven waves. The excitation of filamentation instability for certain cases of interest is discussed and compared with that of the parametric decay and modulation instability. The relevance of the proposed instability with some observations is commented.

I. Introduction

A great deal of interest in the stability of the MHD system in the presence of finite amplitude Alfvén waves has arisen in recent years [Wong and Goldstein, 1986; Terasawa et al. 1986; Longtin and Sonnerup, 1986]. It is mainly stimulated by the frequent observations of large-amplitude hydromagnetic fluctuations in the solar wind at 1 AU [Belcher and Davis, 1971], in the high speed streams of the solar wind [Abraham-Shrauner and Feldman, 1977], in the upstream of the Jovian bow shock [Goldstein, et al., 1985], and in the interplanetary shocks and the terrestrial foreshock [Vinas, et al. 1984; Smith, et al., 1985]. These fluctuations are generally believed to be circularly polarized Alfvén waves propagating almost exactly field aligned. A class of parametric instabilities excited by the circularly polarized Alfvén pumps has thus been investigated. Two different instability processes are currently discussed in the literature. One leads to the parametric decay instability [Galeev and Oraevskii, 1963; Sagdeev and Galeev, 19669; Cohen and Dewar, 1974; Terasawa et al., 1986], and the other one gives rise to the modulation instability [Lashmore-Davies, 1976; Ionson and Ong, 1976; Goldstein, 1978, Derby, 1978; Longtin and Sonnerup, 1986]. Moreover, the modulation instability has also been analyzed in the region that describes the nonlinear evolution of the Alfvén waves propagating along a static magnetic field [Mio et al. 1976a and b; Mjølhus, 1976; Spangler and Shering, 1982]. A derivative non-linear Schrodinger equation possessing soliton solutions is derived to govern the evolution of nonlinear Alfvén waves. On the contrary, Ovenden et al. [1983] have shown that the evolution of nonlinear Alfvén waves is governed by a set of three coupled equations which in turn are related to the nonlinear Schrodinger equation with known soliton solutions. The possible applications of Alfvén solitons to solar and astrophysical plasmas have been discussed by

Ovenden et al. [1983] and Spangler and Sheerin [1983].

Recently, Sakai and Sonnerup [1983] investigated the effects of dispersion on the modulation instability excited by the circularly polarized Alfvén waves. Their analysis is restricted to the situations that dispersive effects are weak and the wave number k of the sound wave is much smaller than the wave number k_o of the pump wave ($k << k_o$). These restrictions have then been lifted in the more recent work by Wong and Goldstein [1986]. They study the dispersive effects on both the modulation and decay instabilities in a unified manner over a wide range of physical parameters. In addition, the results show that the maximum growth rate of the modulation instability occurs as k is comparable to k_o. A new but weaker instability existing in a very narrow bandwidth near $k \approx k_o$ has also been revealed by their analysis.

In this paper, a filamentation instability which has not been considered by the previous workers is analyzed. It is known that a large-amplitude, initially uniform, wave propagating in a plasma can break up into filaments because of the filamentation instability [G. Schmidt, 1979; Kuo and Schmidt; 1983]. This starts from small perturbations in the plasma density and it results in a modulation of the plasma dielectric constant and wave distribution, which in turn increases the density perturbations. The purpose of the present paper is to show that the filamentation instability can be excited together with the parametric decay and modulation instabilities by the large-amplitude circularly polarized Alfvén waves in the solar wind. The threshold conditions and the growth rates of the instability will be determined and compared with those of the decay instability and the modulation instability. Some observations will be commented for corroborating the predicted characteristic of the proposed instability.

The organization of the paper is as follows. In Section II, we derive the coupling equations for Alfvén sidebands and the purely growing magnetostatic mode. A dispersion relation is obtained in Section III and analyzed for the threshold fields and the growth rates for various cases. The numerical results are also given in Section III. Finally presented in Section IV are a summary and brief discussions.

II. Coupling Equations

We investigate the propagation and filamentation of ducted large-amplitude, circularly polarized Alfvén waves in infinite, spatially uniform plasmas embedded in a constant magnetic field $\vec{B}_o = \hat{z}B_o$. The wave magnetic fields are represented by

$$\vec{B}_{p\pm} = (\hat{x} \pm i\hat{y})B_p \, e^{i(k_o z - \omega_o t)} + c.c. \tag{1}$$

where B_p is the unperturbed wave field intensity, assumed to be constant and a real quantity for simplicity; the $\pm$ signs refer to the right-and left-hand circular polarizations, respectively; k_o and ω_o are the wave number and angular wave frequency, satisfying the dispersion relation $\omega_o^2 = (1 \pm \omega_o/\Omega_i)k_o^2 v_A^2$; *wherein* v_A *and* Ω_i *are the Alfvén speed and the* ion cyclotron frequency, respectively.

The zeroth-order velocity responses of electrons and ions to the Alfvén waves can be written as

$$\vec{v}_{pe\pm} = (1 \pm \omega_o/\Omega_i)\vec{v}_{pi\pm} = -(\hat{x} \pm i\hat{y})(\omega_o/k_o)(B_p/B_o)e^{i(k_o z - \omega_o t)} + c.c. \tag{2}$$

where the subscripts e and i refer to electrons and ions.

The process under consideration is the scattering of the unperturbed Alfvén waves into sidebands (propagating oblique to the z direction) by the simultaneously excited density perturbations associated with the purely growing magnetostatic modes. Let $\vec{k} = \hat{x}k$ be the filamentation wave vector, the density and magnetic field perturbations of the purely growing magentostatic modes have the expression

$$n_s = \tilde{n}_s e^{\gamma t} \cos kx$$

and

$$\vec{B}_s = \hat{z}\tilde{B}_s e^{\gamma t} \sin kx,$$

where $\tilde{n}_s$ and $\tilde{B}_s$ are real amplitudes, and γ is the growth rate; quasineutrality has been assumed. The basic equations that are linearized for analyzing the purely growing modes include the continuity equations, the momentum equations for both electrons and ions, and the Maxwell equations:

$$\gamma n_s + n_o \frac{\partial}{\partial x} v_{sex} = 0 = \gamma n_s + n_o \frac{\partial}{\partial x} v_{six} \tag{3}$$

$$\gamma m \vec{v}_{se} + \vec{F}_e = -\hat{x}(T_e/n_o) \frac{\partial}{\partial x} n_s - e(\vec{E}_s + \frac{1}{c} \vec{v}_{se} \times \hat{z} B_o)$$

$$\gamma M \vec{v}_{si} + \vec{F}_i = -\hat{x}(T_i/n_o) \frac{\partial}{\partial x} n_s + e(\vec{E}_s + \frac{1}{c} \vec{v}_{si} \times \hat{z} B_o) \tag{4}$$

$$\frac{\partial}{\partial x} E_{sy} = -(\gamma/c) B_s \text{ and } \frac{\partial}{\partial x} B_s = (4\pi n_o e/c)(v_{sey} - v_{siy}) \tag{5}$$

where n_o, T_{ej} and m(M) are the unperturbed plasma density, and the unperturbed electron (ion) temperature and mass, respectively; $\vec{F}_{ej}$ are the nonlinear Lorentz forces experienced by electrons and ions that reduce to the

pondermotive forces in the unmagnetized plasma case. In terms of $\vec{v}_{pej\pm}$ and $\delta\vec{v}_{ej\pm}$ that represent the velocity responses of electrons and ions to the unperturbed Alfvén waves and the sidebands respectively, the nonlinear Lorentz forces are given by

$$\vec{F}_{e,i}/m_{e,i} = \nabla(\vec{v}_{pe,i\pm}\cdot\delta\vec{v}^{*}_{e,i\pm}) + i\epsilon_{e,i}(\Omega_{e,i}/\omega_o)$$
$$\{-ik_o\delta v^{*}_{e,i\pm z}\vec{v}_{pe,i\pm}x\hat{z} - \vec{v}_{pe,i\pm}x[\nabla x(\delta\vec{v}^{*}_{e,i\pm}x\hat{z})]\} + c.c. \tag{6}$$

where the notations $m_{ej} = m(M)$ and $\epsilon_{ej} = \pm 1$ are used. One can show in a self-consistent way that the nonlinear Lorentz forces act only in the x direction, i.e., $\vec{F}_{ej} = \hat{x}\,F_{ej}$.

We now substitute the expressions $\vec{v}_{sej} = (\hat{x}\,\tilde{v}_{sejx} + \hat{y}\,\tilde{v}_{sejy})e^{\gamma t}\sin kx$, $\tilde{v}_{sex} = \tilde{v}_{six} = \tilde{v}_{sx}$, $\vec{E}_s = \hat{y}\,\tilde{E}_{sy}e^{\gamma t}\cos kx$ and $\vec{F}_{ej} = \hat{x}\,\tilde{F}_{ej}e^{\gamma t}\sin kx$ into (3)-(5). The relation $\tilde{B}_s/B_o = -[\omega^2_{pe}/(\omega^2_{pe} + k^2c^2)]\tilde{n}_s/n_o$ is obtained and the resultant equations can be combined into a single coupled mode equation for the purely growing magnetostatic mode

$$\{\gamma^2 + [k^2 v_A^2/(1 + k^2 v^2_A/\Omega_e\Omega_i)] + k^2 c^2_s\}\tilde{n}_s/n_o = (k/M)(\vec{F}_e + \vec{F}_i) \qquad (7)$$

This equation gives the purely growing density perturbation as a function of the Alfven waves and sidebands. Without the nonlinear Lorentz forces, Eq. (6) reduces to the linear dispersion relation of the magnetosonic eigen-mode. The magnetostatic mode is, however, a nonlinearly driven mode.

The Alfven sidebands are excited through the beating current density driven by the Alfven pump wave fields on the density perturbation of the magnetostatic mode. The coupled mode equation for these sidebands can be derived from the following fluid equations for electrons and ions together with the Maxwell equations:

$$\frac{\partial}{\partial t}\,\delta n_\pm + \nabla\cdot(n_o \delta\vec{v}_{e\pm} + n_s \vec{v}_{pe\pm}) = 0 = \frac{\partial}{\partial t}\,\delta n_\pm + \nabla\cdot(n_o \delta\vec{v}_{i\pm} + n_s \vec{v}_{pi\pm}) \qquad (8)$$

$$\delta\vec{E}_\pm + \frac{1}{c}\,\delta v_{e\pm} \times \hat{z}B_o = -(T_e/n_o e)\,\nabla\,\delta n_\pm \qquad (9)$$

$$\frac{\partial}{\partial t}\,\delta\vec{v}_{i\pm} = -c_s^2 \nabla(\delta n_\pm/n_o) + (e/Mc)(\delta\vec{v}_{i\pm} - \delta\vec{v}_{e\pm}) \times \hat{z}B_o \qquad (9')$$

$$\nabla \times \delta\vec{E}_\pm = -\frac{1}{c}\,\frac{\partial}{\partial t}\,\delta\vec{B}_\pm \qquad (10)$$

and

$$\nabla x \delta\vec{B}_\pm = (4\pi n_o e/c)[(\delta\vec{v}_{i\pm} - \delta\vec{v}_{e\pm}) + (n_s/n_o)(\vec{v}_{pi\pm} - \vec{v}_{pe\pm})] \qquad (11)$$

where $c_s^2 = (T_e + T_i)/m_i$.

We have neglected the nonlinear Lorentz forces ($\vec{v} \cdot \nabla \vec{v}$) in (9) and kept the beating currents ($n_s \vec{v}_{p\pm}$) in (8) and (11) as the driving sources of the Alfven sidebands. The underlying reason is that the purely growing mode is more effective in producing density perturbations than velocity perturbations.

Following the functional dependence of the magnetostatic mode, we express the physical quantities of the sidebands as

$$\delta\vec{v}_{ei\pm} = [(\hat{x}\,\delta\tilde{v}_{ei\pm x} \pm i\hat{y}\,\delta\tilde{v}_{ei\pm y})\cos kx + i\hat{z}\,\delta\tilde{v}_{ei\pm z}\sin kx]e^{\gamma t}e^{i(k_o z - \omega_o t)} + c.c.$$

$$\delta n_{\pm} = i\,\delta\tilde{n}_{\pm}\sin kx\; e^{\gamma t}e^{i(k_o z-\omega_o t)} + c.c.$$

$$\delta\vec{B}_{\pm} = [(\hat{x} \pm i\alpha_{\pm}\hat{y})\cos kx - i\hat{z}(k/k_o)\sin kx]\delta\tilde{B}_{\pm}\; e^{\gamma t}e^{i(k_o z-\omega_o t)} + c.c. \qquad (12)$$

where the upper sideband ($\vec{k}_+ = \vec{k}_o + \vec{k}$, $\omega_+ = \omega_o + i\gamma$) and lower sideband ($\vec{k}_- = \vec{k}_o - \vec{k}$, $\omega_- = \omega_o - (i\gamma)^*$) propagate together along the magnetic field and form a standing wave pattern across the magnetic field, $\alpha_{\pm}$ are unknown parameters defining the polarizations of the Alfvén sidebands and will be determined shortly; the expressions of $\delta\vec{E}_{\pm}$ can be obtained from the Faraday law (10).

Substituting (12) into (8)-(11), and eliminating $\delta\tilde{n}_{\pm}$ from (8) and (9), we first obtain

$$\delta\tilde{v}_{e\pm x} = -(\omega_o/k_o)\delta\tilde{B}_\pm/B_o$$

$$\delta\tilde{v}_{e\pm y} = -\alpha_\pm(\omega_o/k_o)\delta\tilde{B}_\pm/B_o$$

$$\delta\tilde{v}_{i\pm x} = [(k_o v_A^2/\omega_o)(\tilde{n}_s/n_o)(B_p/B_o) - (k_o\Omega_i^2/k^2\omega_o)(\omega_o^2/k_o^2 v_{ti}^2 - 1)(1 \mp \alpha_\pm\omega_o/\Omega_i)(\delta\tilde{B}_\pm/B_o)]/f$$

$$\delta\tilde{v}_{i\pm y} = \mp(\Omega_i/\omega_o)\{(k_o v_A^2/\omega_o)(\tilde{n}_s/n_o)(B_p/B_o) + (\omega_o/k_o)[1 + (k_o/k)^2(\Omega_i/\omega_o)(\omega_o^2/k_o^2 v_{ti}^2 - 1)(\pm\alpha_\pm - \omega_o/\Omega_i)](\delta\tilde{B}_\pm/B_o)\}/f$$

$$\delta\tilde{v}_{i\pm z} = -(k_o/k)(\Omega_i/\omega_o)^2[(1-\omega_o^2/\Omega_i^2)(k_o v_A^2/\omega_o)(\tilde{n}_s/n_o)(B_p/B_o) + (\omega_o/k_o)(1 \mp \alpha_\pm\omega_o/\Omega_i)(\delta\tilde{B}_\pm/B_o)\}/f \qquad (13)$$

where $f = 1 + (k_o/k)^2(\Omega_i/\omega_o)^2(1-\omega_o^2/\Omega_i^2)(\omega_o^2/k_o^2 v_{ti}-1)$, and $v_{ti} = (T_i/M)^{1/2}$ is the ion thermal speed.

The missing component $\delta\tilde{v}_{e\pm z}$ can be obtained from the z component of (11), it reads

$$\delta\tilde{v}_{e\pm z} = \delta\tilde{v}_{i\pm z} \pm \alpha_\pm(kv_A^2/\Omega_i)(\delta\tilde{B}_\pm/B_o) \qquad (14)$$

These relations of (13) and (14) are then used in the remaining two equations, i.e., the x and y component of (11), leading to the determination of the parameter

$$\alpha_{\pm} = \{(1 \pm \omega_o/\Omega_i)[1-(k_o/k)^2(\omega_o^2/k_o^2v_{ti}^2-1)] + (f \pm \Omega_i/\omega_o)(k_o^2v_A^2/\Omega_i^2)(1+k^2/k_o^2)\}/$$

$$\{(1/f \pm \omega_o/\Omega_i)[1-(k_o/k)^2(\omega_o^2/k_o^2v_{ti}^2-1)]$$

$$+ (1-\Omega_i^2/\omega_o^2f)[fk_o^2v_A^2/\Omega_i^2-(k_o/k)^2(\omega_o^2/k_o^2v_{ti}^2-1)]\} \qquad (15)$$

and that of the coupled mode equations for the Alfvén sidebands

$$\{1-(k_o/k)^2(\Omega_i/\omega_o)^2(1 \mp \alpha_{\pm}\omega_o/\Omega_i)(\omega_o^2/k_o^2v_{ti}^2-1)/f \mp \alpha_{\pm}(k_o^2v_A^2/\Omega_i\omega_o)\}(\tilde{\delta B}_{\pm}/B_o)$$

$$= -(1/f \pm \omega_o/\Omega_i)(k_o^2v_A^2/\omega_o^2)(\tilde{n}_s/n_o)(B_p/B_o) \qquad (16)$$

Equation (16) shows the sideband fields to be produced by the pump field and the purely growing density perturbation of the magnetostatic mode. Thus, equations (7) and (16) form a complete coupled set of equations describing the proposed instability process.

III. Dispersion Relation

With the aid of (2), (13), (14) and (6), the coupling term on the right hand side of (7) can be expressed explicitly as

$$
\begin{aligned}
(\tilde{F}_e + \tilde{F}_i)/M = \pm 2k(\Omega_i/\omega_o)(k_o v_A^2/\Omega_i)^2 \Big(& \{1 + k^2/k_o^2 \mp (\omega_o \Omega_i/k_o^2 v_A^2)[\alpha_\pm + (m/M) \\
& (1+\alpha_\pm)(1 \pm \omega_o/\Omega_i) \\
& - (1/f)(k_o/k)^2(\Omega_i/\omega_o)^2(1 \mp \alpha_\pm \omega_o/\Omega_i)]\}(\delta\tilde{B}_\pm/B_o) \mp (\Omega_i/\omega_o) \\
& \{(1 \pm 2\omega_o/\Omega_i) \\
& - (k_o/k)^2(\Omega_i/\omega_o)^2(1-\omega_o^2/\Omega_i^2)/f\}\ (\tilde{n}_s/n_o)(B_p/B_o)\Big)(B_p/B_o) \qquad (17)
\end{aligned}
$$

Substituting (17) into (7) and combining the resultant with (16), we finally obtain the dispersion relation

$$
\begin{aligned}
& \gamma^2 + k^2 v_A^2/(1 + k^2 v_A^2/\Omega_e \Omega_i) + k^2 c_s^2 + 2k^2 (k_o v_A^2/\omega_o)^2 [(1 \pm 2\omega_o/\Omega_i) - (k_o/k)^2 \\
& \quad (\Omega_i^2/\omega_o^2 - 1)/f](B_p/B_o)^2 \\
& = -2k^2 (k_o v_A^2/\omega_o)^2 (k_o^2 v_A^2/\Omega_i^2)(1 \pm \Omega_i/\omega_o f)\{1 + k^2/k_o^2 \mp (\omega_o \Omega_i/k_o^2 v_A^2) \\
& \quad [\alpha_\pm + (m/M)(1+\alpha_\pm)(1 \pm \omega_o/\Omega_i) \\
& \quad -(1/f)(k_o/k)^2(\Omega_i/\omega_o)^2(1 \mp \alpha_\pm \omega_o/\Omega_i)]\}(B_p/B_o)^2/ \\
& \quad \{1-(k_o/k)^2(\Omega_i/\omega_o)^2(1 \mp \alpha_\pm \omega_o/\Omega_i)(\omega_o^2/k_o^2 v_{ti}^2 - 1)/f \mp \alpha_\pm k_o^2 v_A^2/\omega_o \Omega_i\} \qquad (18)
\end{aligned}
$$

Equation (18) is a general expression of the dispersion relation for filamentation instability of ducted Alfven waves. It will be analyzed in the following to determine the threshold conditions and the growth rates of the instability.

In principal, (18) is a quadratic equation in γ and can be solved analytically. However, since the coefficients of (18) are complicated functions of the constant parameters $\beta = c_s^2/v_A^2$ and $K = K_o V_A/\Omega_i$ and the normalized variable parameter $K = k/k_o$ (the notations used in Wong and Goldstein [1986] are adopted). A numerical analysis of (18) with different parameters is desirable. In doing so, we vary K from 0 to 2, and examine the dependences of the threshold intensity and the growth rate on β and K for both right-(R) and left-hand (L-H) circularly polarized Alfven waves. Presented in Figures 1-4 are the dependence of the normalized threshold intensity (η^2_{th}) on K. $\eta^2_{th} = (B_p/B_o)^2_{th}$ is obtained by setting $\gamma = 0$ in (18). Figures 1 and 2 correspond to the R-H circularly polarized waves. It is shown that the filamentation instability has a lower threshold level for a wave with a smaller frequency (i.e. smaller κ). In addition, the threshold of the instability also varies with β. For very low frequency waves ($\kappa \leq 0.05$) the threshold intensity increases with β. It, however, becomes a decreasing function of β for $\kappa \geq 0.1$. This trend has been demonstrated in these two Figures, wherein $\kappa = 0.01$ and 0.3 are used as the representative parametric values. We have excluded the threshold values in the neighborhood of X (marked on the curves) from the Figures. This is because, in that wave number region the nonlinear Lorentz forces on electrons and on ions are in opposite direction with comparable magnitude so that the two terms proportional to $(B_p/B_o)^2$ in (18) tend to cancel to each other and the threshold, thus, becomes very high.

Figures 3 and 4 correspond to L-H circularly polarized waves. It is found that the instability can only be excited by waves with higher frequencies (e.g. $\kappa \geq 0.15$) with reasonable thresholds. The dependence of the threshold on κ for $\beta = 1.5$ and that on β for $\kappa = 0.3$ are also shown in Figures 3 and 4, respectively. It appears that the instability prefers to be excited in the region $K < 0.5$. Otherwise, the threshold increases very fast with K. In the region $K < 0.5$, the threshold decreases with both κ and β until the instability becomes forbidden for the region of very small κ (e.g. the region below K = X marked in both Figures 3 and 4 for $\kappa = 0.3$ and $\beta = 1.5$).

We next present the growth rates of the instability. Shown in Figures 5 and 6 are the functional dependence of the growth rate γ on the wave field intensity η^2 of R-H wave for low $\beta(= 0.5)$ and high $\beta(= 1.5)$ cases, where κ and K are considered to be constant parameters. In order to obtain adequate information for the dependencies of γ in these two cases, two representative values for each of the two parameters κ and K are chosen in the figure presentation. $\kappa = 0.01$ and 0.3 stand for the cases of the low-frequency and high-frequency waves, respectively. We then use K = 0.1 and 1 to characterize the regions of large-scale and small-scale filamentation instability, respectively. The results show that, in general, the growth rate increases with β and K and it decreases with κ. For L-H wave case, the instability can only be excited by the high-frequency waves in the high β plasma. We, therefore, choose $\beta = 1.5$ and $\kappa = 0.15$ and 0.3 to evaluate the dependence of γ on η^2. Again K = 0.1 and 1 are considered and the results are presented in Figure 7. In this case, the growth rate increases with κ for K = 0.1 and becomes a decreasing function of κ for K = 1.

IV. Summary and Discussion

We have investigated the filamentation instabilities of large amplitude, circularly polarized Alfvén waves propagating along the background magnetic field. The instabilities are excited via the scattering of the unperturbed Alfvén pumps (considered as a pump wave) into sidebands by the density perturbations that are associated with the simultaneously excited purely growing magnetostatic modes. A four-wave coupling process is then considered for the analysis of the instabilities. The theory developed is based on the two fluid plasma model. In general, the fluid model is valid when the condition $K^2 v_{ti}^2/\Omega_i^2 = K^2\kappa^2\beta/2 \ll 1$ is satisfied. In the present work, the maximum value of the parameter $K^2\kappa^2\beta/2$ for $K = 2$, $\kappa = 0.3$ and $\beta = 1.5$ is 0.27, which reasonably justifies the use of the fluid model. For the more general consideration that includes the region $K^2\kappa\beta/2 \gtrsim 1$, however, a kinetic plasma model should be used.

The nonlinear source for the Alfvén sidebands is the beating current driven by the pump wave field on the density perturbation of the purely growing mode, whereas, the nonlinear Lorentz force (which reduces to the pondermotive force in the unmagnetized case) introduced by the spatial gradient of the resultant high frequency wave field is the driving source for the nonoscillatory (i.e., the purely growing) mode. These nonlinear effects result in the coupling of nonoscillatory mode with the Alfvén sidebands through the Alfvén pump wave. A dispersion relation of the instabilities is thus derived by combining the coupled mode equations together. Solving the dispersion relation, we have determined the threshold fields and the growth rates for the caes of the R-H and L-H circularly polarized pump waves. We have also determined the functional dependencies of the threshold field η_{th} on the wavenumber K of the nonoscillatory mode, the β of the plasma, and the frequency κ

of the pump (see Figures 1-4). The dependence of the growth rate $\bar{\gamma}$ on the pump intensity η^2 is examined for several sets of representative parameters (K,β,κ) (see Figures 5-7).

For the geophysical applications of the concerned instabilities, we follow the examples discussed by Wong and Goldstein [1986]. The finite amplitude Alfvén waves that were observed in the high speed streams of the solar wind and discussed by Abraham-Shrauner and Feldman [1977] are the left-hand circularly polarized with $\kappa = 0.3$ and $\eta^2 = 0.05$. As shown in Wong and Goldstein [1986], these waves are stable to both the modulational and the decay instabilities for $\beta > 1$. From our analysis, however, it is found that these waves are unstable to the filamentation instability in the small K region. The growth rates of the instability evaluated for $\beta = 1.5$ have been presented in Figure 8. We, therefore, predict the appearance of nonoscillatory, cross-field plasma density perturbations and magnetic field perturbations in the background solar wind plasma. However, these predicted cross-field density striations and magnetostatic structure probably have not been observed in Abraham-Shrauner and Feldman [1977]. The difficulty in the in-situ measurements by satellites lies on the large velocity difference between the solar wind and the satellite.

Low frequency, left-hand polarized finite amplitude Alfvén waves have also been observed in the upstream of the Jovian bow shock [Goldstein, et al., 1985]. It is shown from our analysis that this wave is filamentally stable. In fact, only the decay instability is very weakly unstable for the case $\kappa = 0.02$, $\eta^2 = 0.05$ and $\beta = 1.5$. Whereas, the observation of right-hand polarized waves were not reported. It can be speculated from the linear dispersion relations of the Alfvén waves. Because, in such low frequency region, the dispersion relations of right and left-hand polarized Alfvén

waves are almost identical. If it is indeed so, the filamentation instability is found to be unstable against to the right-hand pumps in the entire K region of interest. The functional dependence of the growth rate of the instability on K is presented in Figure 9. Again, this instability introduces nonoscillatory, cross-field density and magnetic fluctuations to the background plasma, and thus, can attribute to the observed correlations in the magnetic and density fluctuations.

For the other cases of right-hand polarized waves in interplanetary shocks and in the terrestrial foreshock [Vinas, et al., 1984; Smith, et al., 1985], the filamentation instability requires a threshold power higher than that used by Wong and Goldstein [1986] in each case.

Acknowledgements

This work is supported by the Air Force Office of Scientific Research, Grant No. AFOSR-85-0133. The numerical work was performed at the Pittsburgh Supercomputing Center of NSF.

References

Abraham-Shrauner, B., and W.C. Feldman, Nonlinear Alfvén waves in high-speed solar wind streams, J. Geophys. Res., 82, 618, 1977.

Belcher, J.W., and Davis, L., Large-amplitude Alfvén waves in the interplanetary medium, 2, J. Geophys. Res., 76, 3534, 1971.

Cohen, R., and Dewar, R., On the backscatter instability of solar wind Alfvén waves. J. Geophys. Res., 79, 4174, 1974.

Derby, N.F., Modulational instability of finite-amplitude circularly polarized Alfvén waves, Astrophys. J., 224, 1013, 1978.

Galeev, A.A., and Oraevskii, V.N., The stability of Alfvén waves, Sov. Phys. Dokl., Engl. Transl., 7, 988, 1963.

Goldstein, M.L., An instability of finite amplitude circularly polaried Alfvén waves, Astrophys, J., 219, 700, 1978.

Goldstein, M.L., H.K. Wong, A.F. Vinas and C.W. Smith, Large-amplitude MHD waves upstream of the Jovian bow shock Reinterpretation, J. Geophys. Res., 90, 302, 1985.

Ionson, J.A., and Ong, R.S.B., The long time behavior of a finite amplitude shear Alfvén wave in a warm plasma, Plasma Phys., 18, 809, 1976.

Kuo, S.P., and Schmidt, G., Filamentation instability in magneto plasmas, Phys. Fluids, 26, 2529, 1983.

Lashmore-Davies, C.N., Modulation instability of a finite amplitude Alfvén wave, Phys. Fluids, 19, 587, 1976.

Longtin, M., and Sonnerup, B.U.Ö. , Modulational Instability of Circularly Polarized Alfvén waves, J. Geophys. Res., 91, 6816, 1986.

Mio, J., Ogino, T., Minami, K., and Takeda, S., Modified nonlinear Schrodingen equation for Alfvén wave propagating along the magnetic field in cold plasmas, and, modulational instability and envelope-solitons for nonlinear Alfvén waves propagating along the magnetic field in plasmas, J. Phys. Soc. Jpn., 41, 265 and 667, 1967a & b.

Mjølhus, E., On the modulational instability of hydromagnetic waves parallel to the magnetic field, J. Plasma Phys., 16, 321, 1976.

Ovenden, C.R., Shah, H.A. and Schwartz, S.J., Alfvén soitons in the solar wind, J. Geophys. Res., 88, 6095, 1983.

Sagdeev, R.Z., and Galeov, A.A., Nonlinear plasma theory, edited by T. O'Neil and D. Book, W.A. Benjamin, New York, 1969.

Sakai, J., and Sonnerup, B.U.O., Modulational instability of finite amplitude dispensive Alfvén waves, J. Geophys. Res., 88, 9069, 1983.

Schmidt, G., Physics of high temperature plasma, Academic, New York, 1979, 2nd. edition.

Smith, C.W., Goldstein, M.L., Gary, S.P., and Russell, C.T., Beam driven ion-cyclotron harmonic waves resonances in the terrestrial foreshock, J. Geophys. Res., 90, 1429, 1985.

Spangler, S.R., and Sheering, J.P., Alfvén wave collapse and the stability of a relativistic electron beam in a magnetized astrophysical plasma, Astrophys. J., 272, 273, 1983.

Terasawa, T., Hoshino, M., Sakai, J.I., and Hada, T., Decay Instability of Finite-Amplitude Circularly Polarized Alfvén Waves: A Numerical Simulation of Stimulated Brillouon Scattering, J. Geophys. Res., 91, 4171, 1986.

Vinas, A.F., Goldstein, M.L., and Acuna, M.H., Spectral analysis of magnetohydrodynamic fluctuations near interplanetary shocks, J. Geophys. Res.,89, 6813, 1984.

Wong, H.K., and Goldstein, M.L., Parametric instabilities of circularly polarized Alfvén waves including dispersion, J. Geophys. Res., 91, 5617, 1986.

Figure Captions

Fig. 1 Functional dependence of the threshold field intensity on K and β for low frequency (κ = 0.01) R-H circularly polarized pump.

Fig. 2 Dependence of the threshold field intensity on K and β for high frequency (κ = 0.3) R-H circularly polarized pump.

Fig. 3 Dependence of the threshold field intensity on K and κ for L-H circularly polarized pump in high β(= 1.5) plasma.

Fig. 4 Dependence of the threshold field intensity on K and β for high frequency (κ = 0.3) L-H circularly polarized pump.

Fig. 5 The dependence of the normalized growth rate $\tilde{\gamma} = \gamma/k_0 V_A$ on the R-H circularly polarized pump intensity η^2, where K = 0.1 and (κ, β) as indicated are set in the evaluation.

Fig. 6 Dependence of $\tilde{\gamma}$ on η^2 of R-H circularly polarized pump for K = 1 and (κ, β) as indicated.

Fig. 7 Dependence of $\tilde{\gamma}$ on η^2 of a L-H circularly polarized pump in a plasma with β = 1.5.

Fig. 8 Dependence of $\tilde{\gamma}$ on K for a L-H circularly polarized pump with η^2 = 0.05 and κ = 0.3 in a plasma with β = 1.5.

Fig. 9 Dependence of $\tilde{\gamma}$ of K for a R-H circularly polarized pump with η^2 = 0.05 and κ = 0.02 in a plasma with β = 1.5.

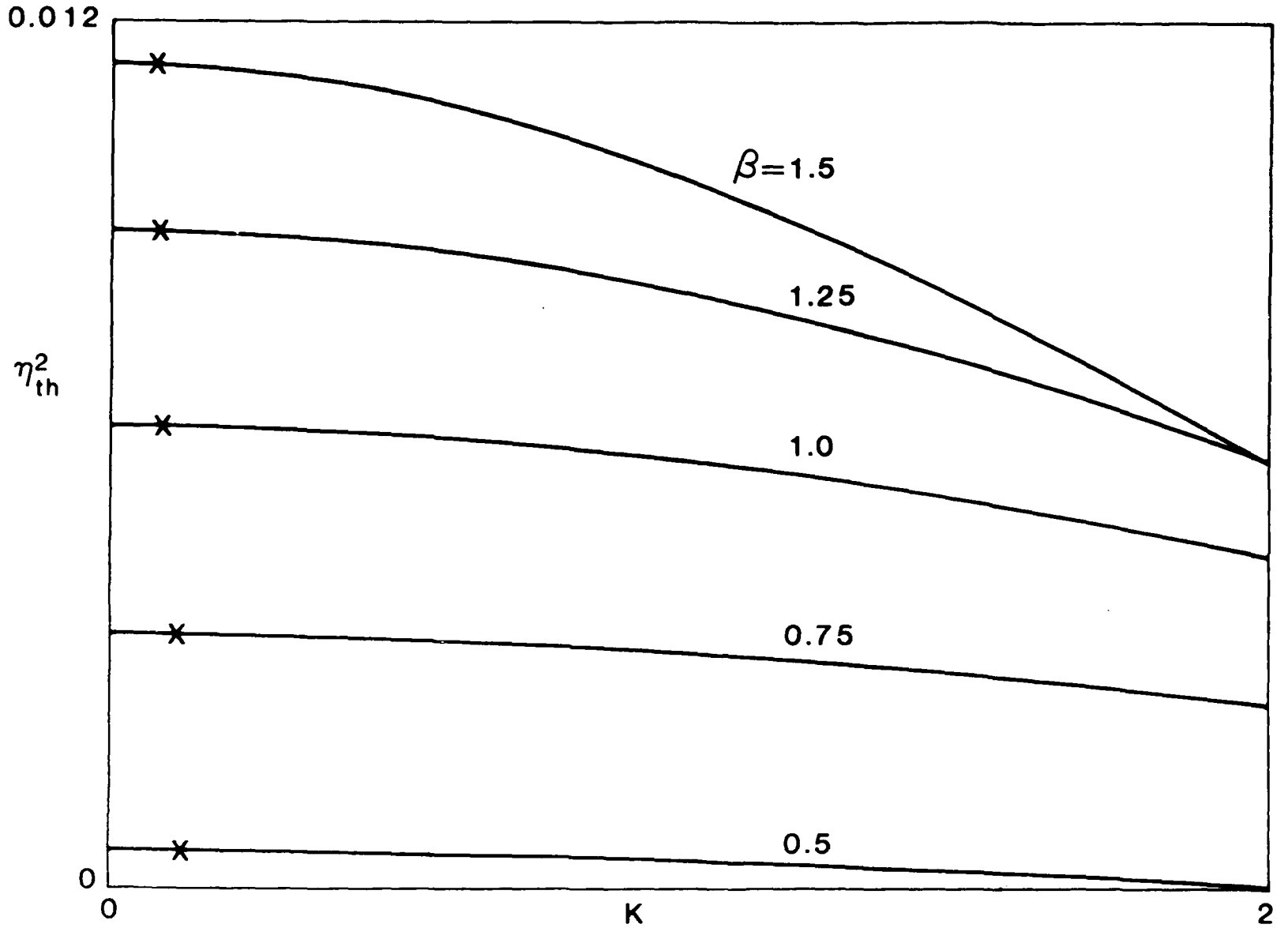

Fig. 1 Functional Dependencies of the threshold field intensity on K and β for low frequency ($\kappa = 0.01$) R-H circularly polarized pump

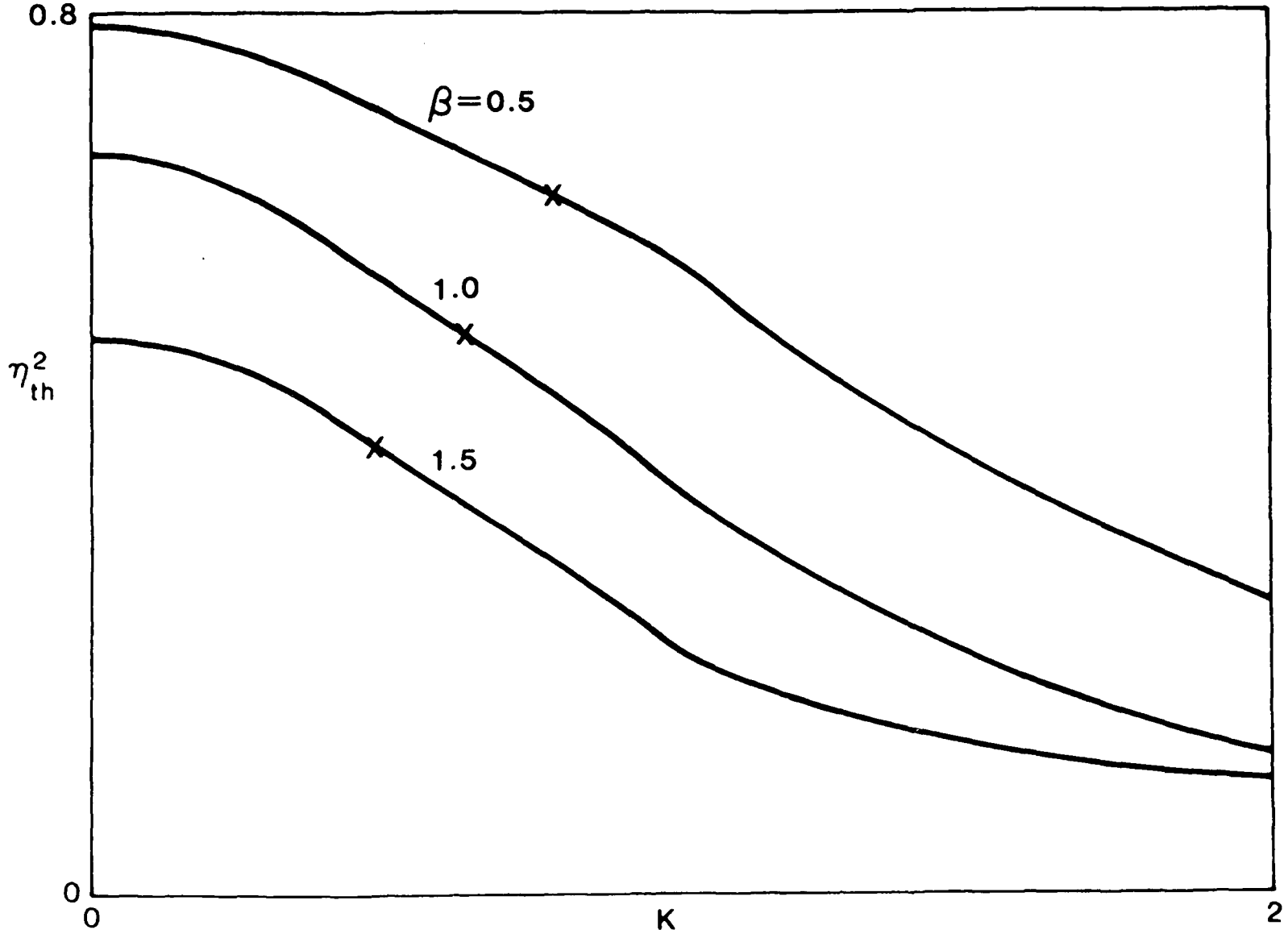

Fig. 2 Dependecies of the threshold field intensity on K and β for high frequency (κ=0.3) R-H circularly polarized pump

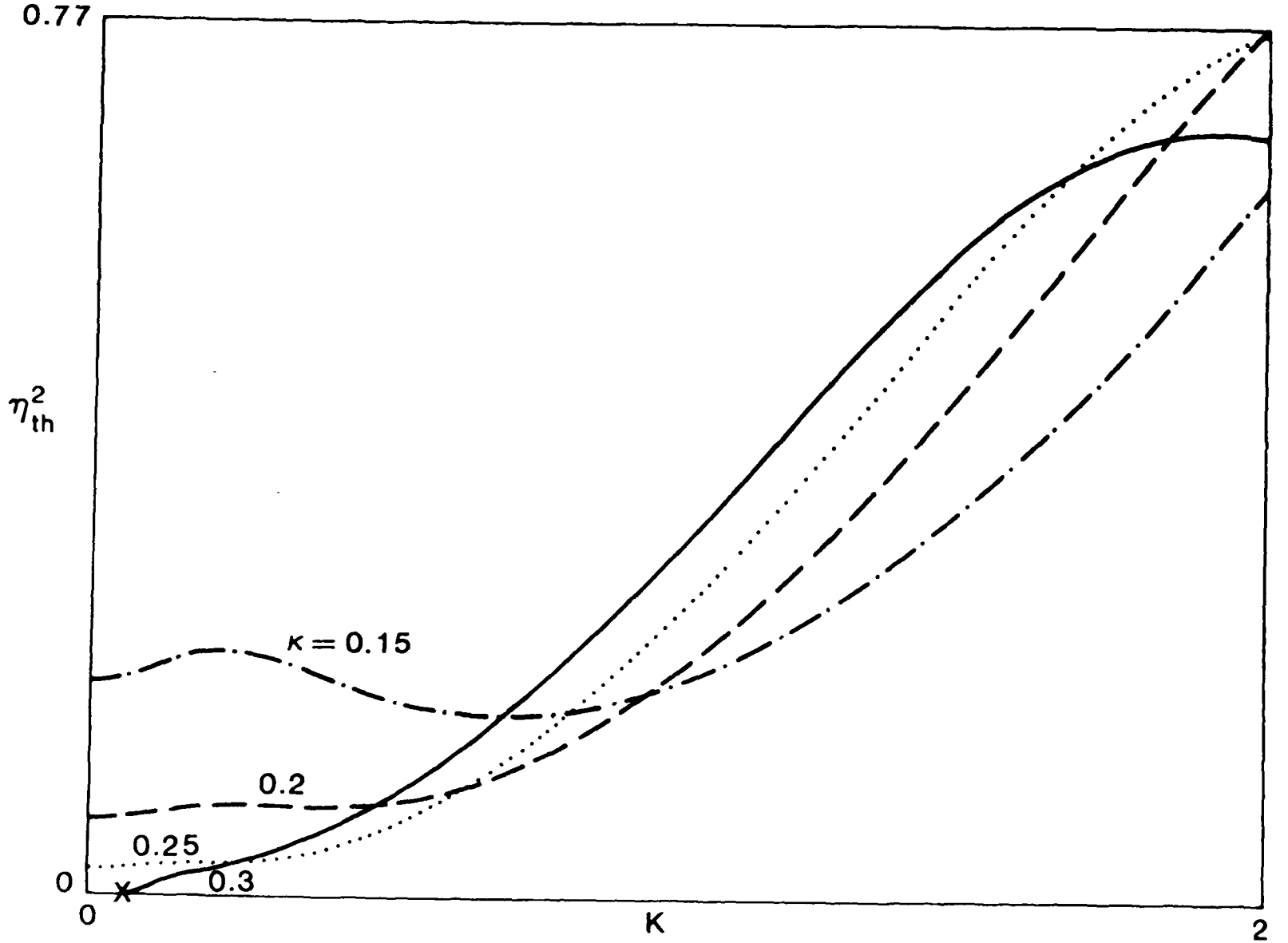

Fig. 3. Dependencies of the threshold field intensity on K and κ for L-H circularly polarized pump in high β (=1.5) plasma

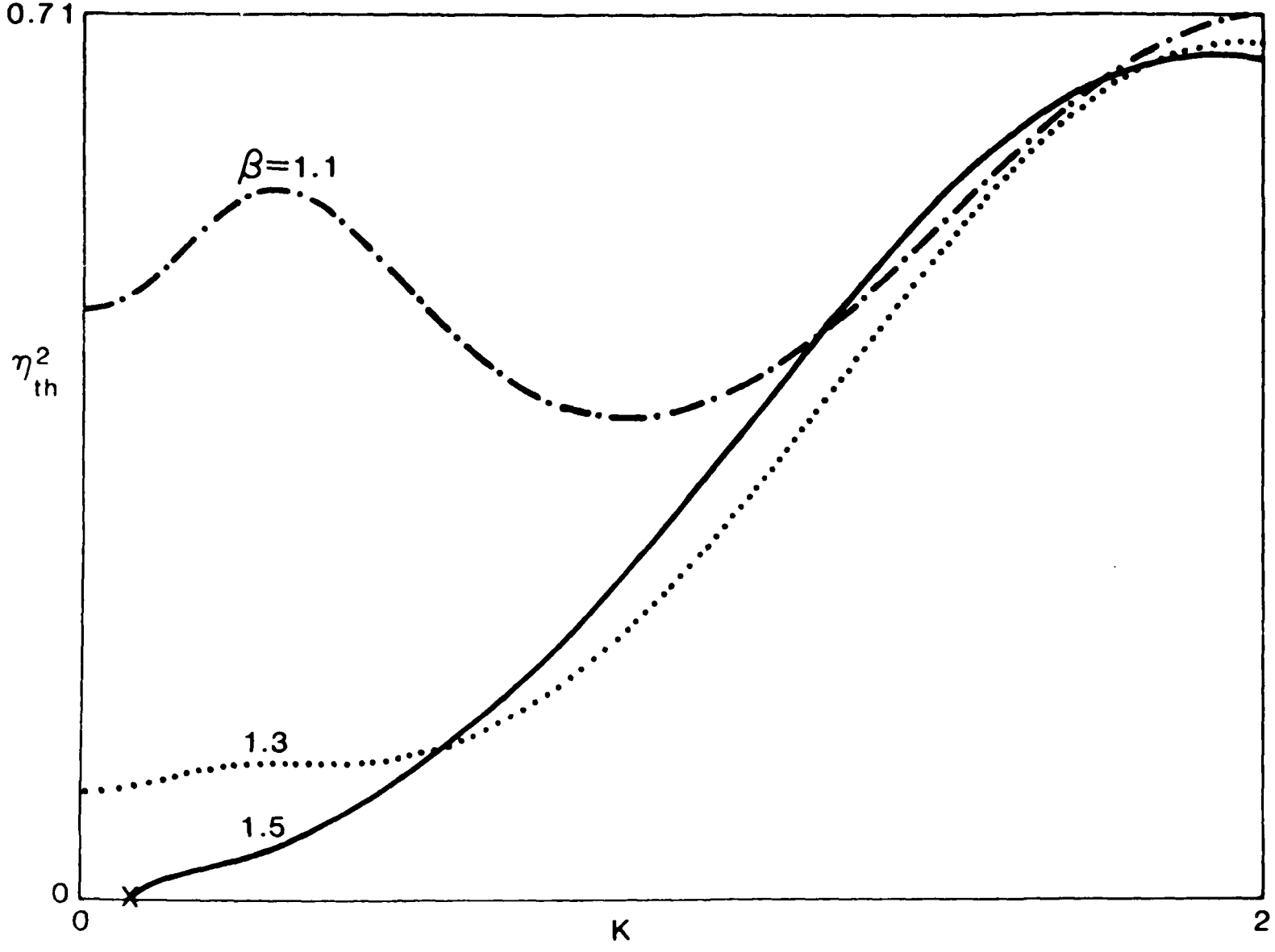

Fig. 4 Dependencies of the threshold field intensity on K and β for high frequency (κ=0.3) L-H circularly polarized pump

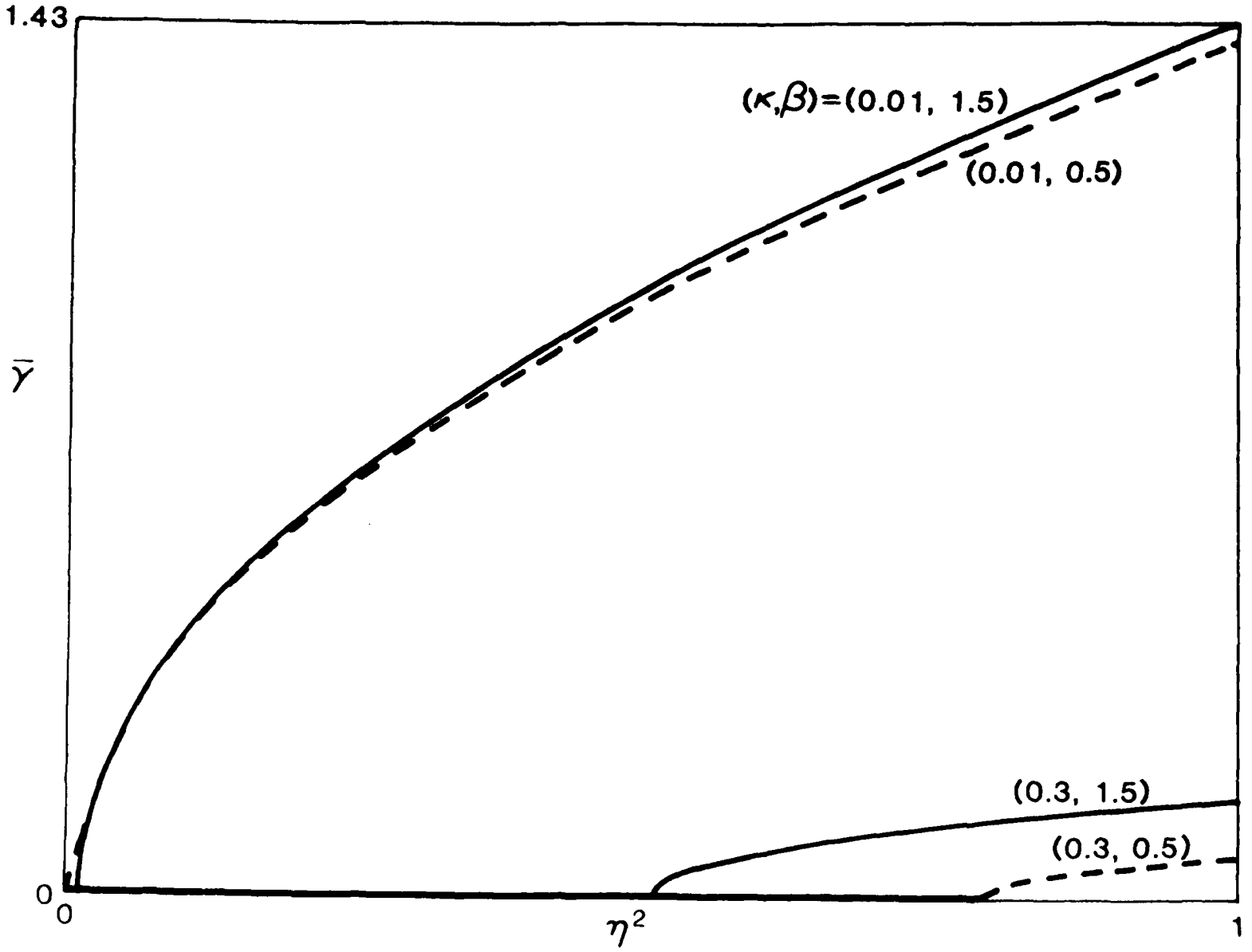

Fig. 5 The dependence of the normalized growth rate $\bar{\gamma}=\gamma/k_0V_A$ on the R-H circularly polorized pump intensity η^2, where K=0.1 and (κ,β) as indicated are set in the evaluation.

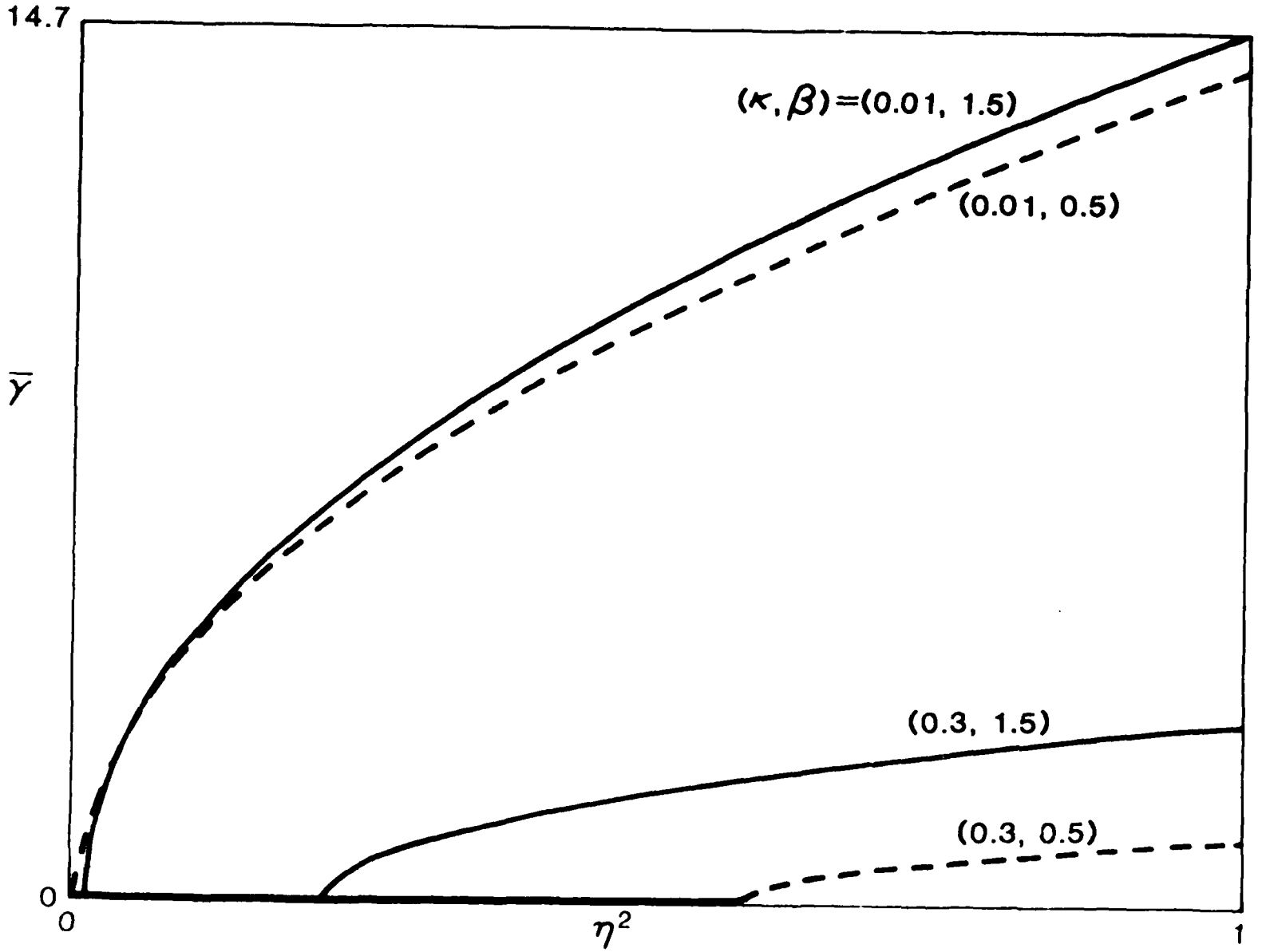

Fig. 6 Dependence of $\overline{\gamma}$ on η^2 of R-H circularly polorized pump for K=1 and (κ, β) as indicated.

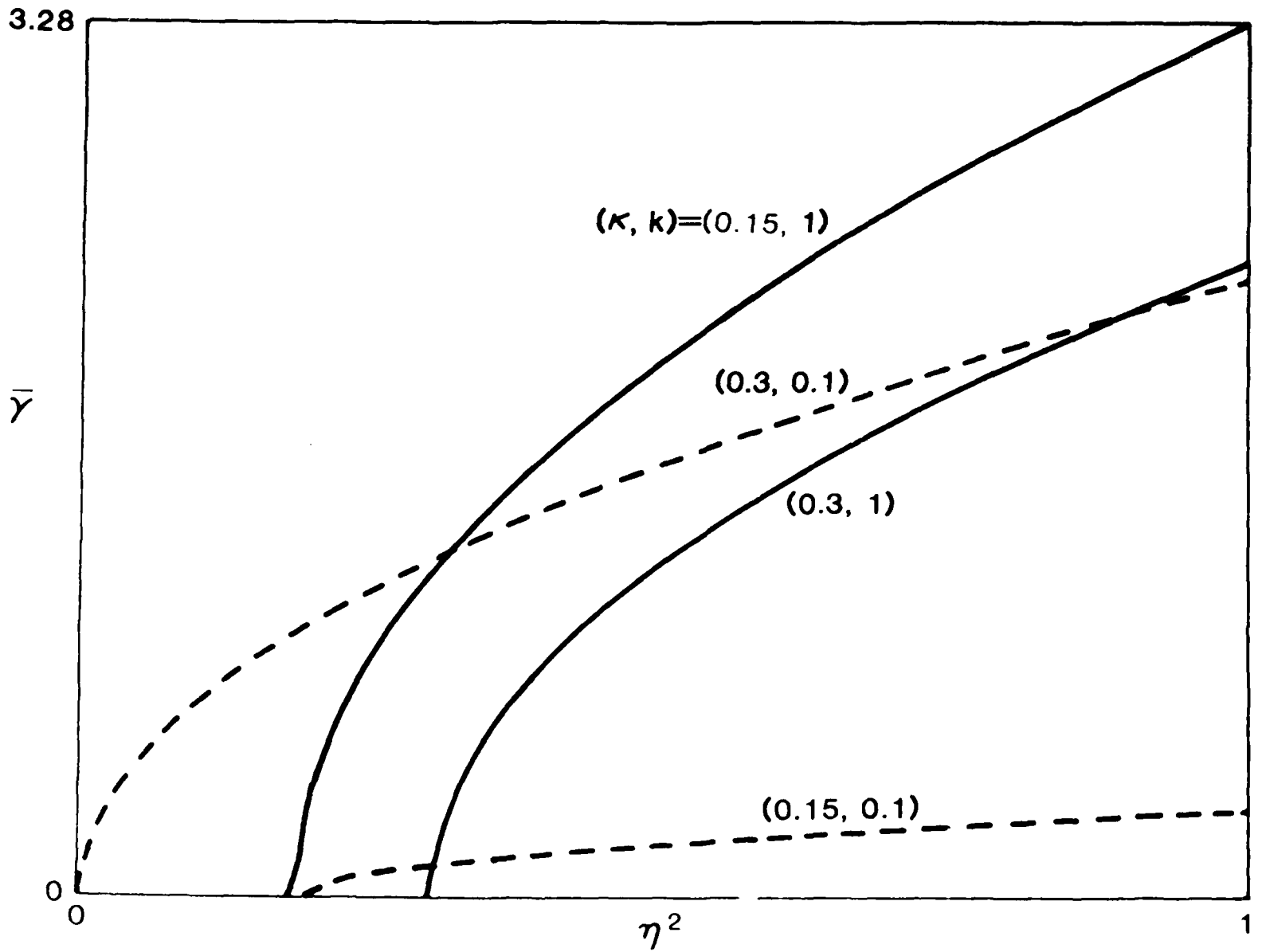

Fig. 7 Dependence of $\bar{\gamma}$ on η^2 of a L-H circularly polorized pump in a plasma with $\beta=1.5$

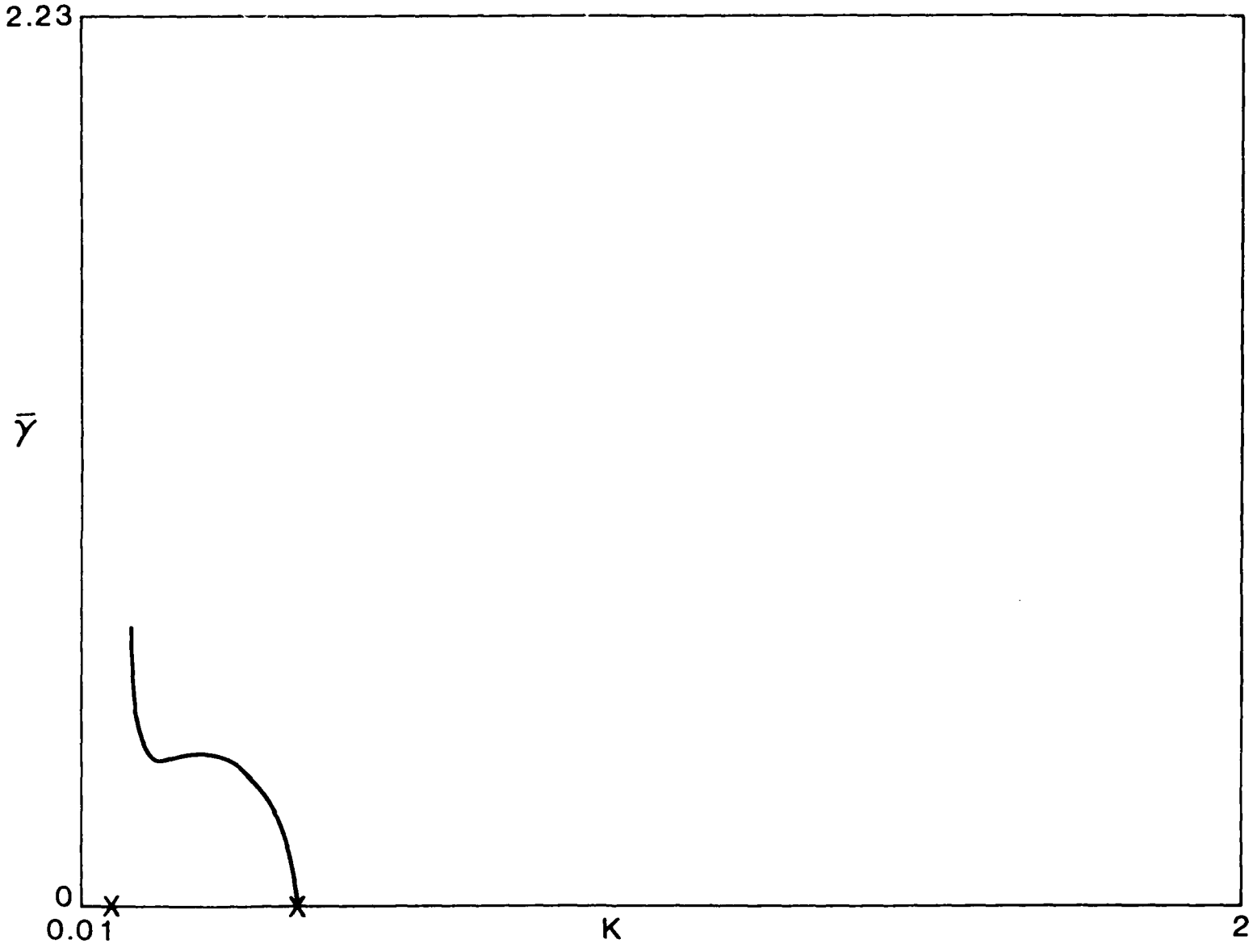

Fig. 8 Dependence of $\bar{\gamma}$ on K for a L–H circularly polarized pump with $\eta^2 = 0.05$ and $\kappa = 0.3$ in a plasma with $\beta = 1.5$.

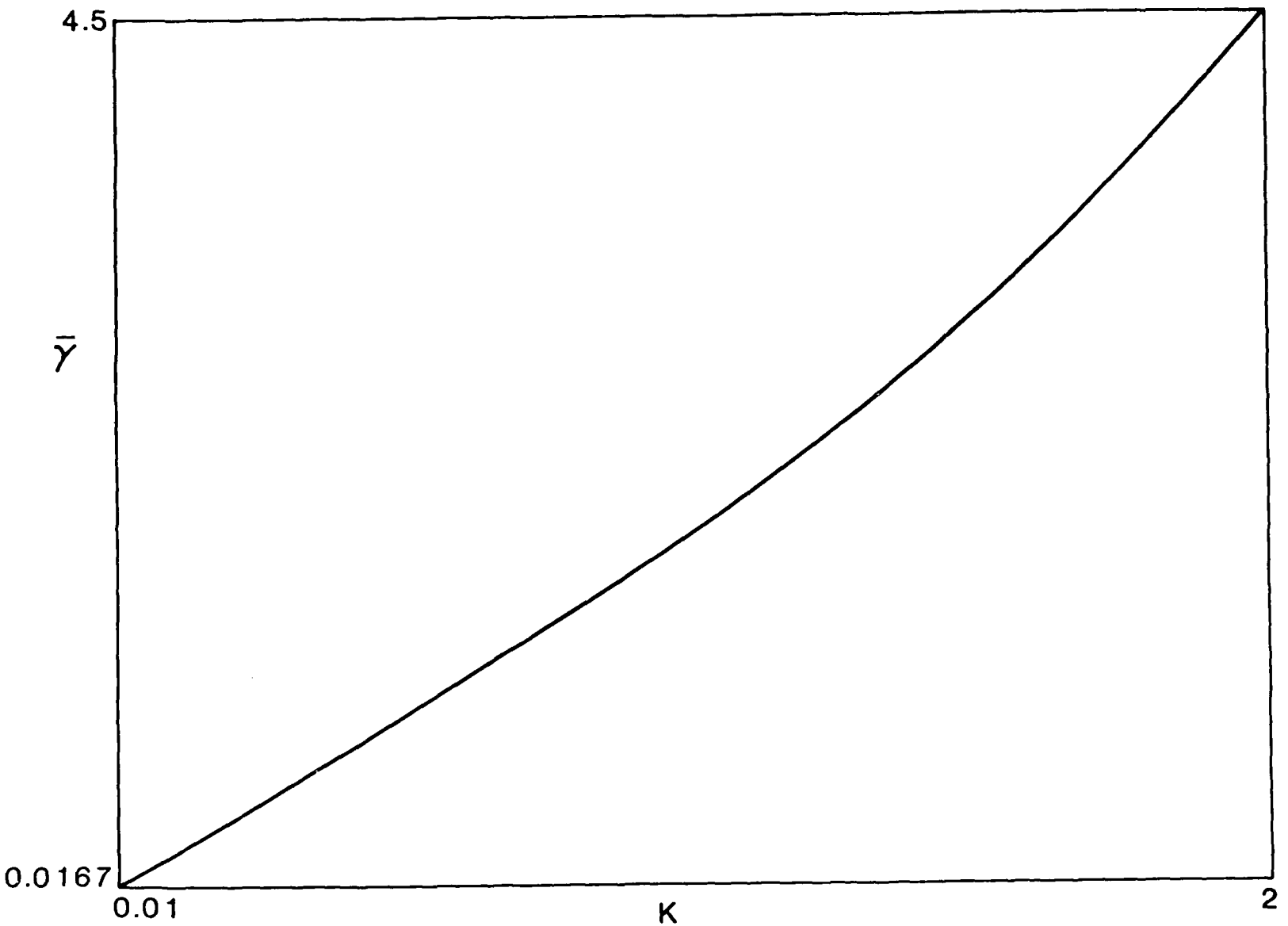

Fig. 9 Dependence of $\bar{\gamma}$ of K for a R-H circularly polarized pump with $\eta^2 = 0.05$ and $\kappa = 0.02$ in a plasma with $\beta = 1.5$.

The Stability Analyses of a Finite Difference Scheme for the Coupled Hydromagnetic Wave Equations in the Dipole Model of the Magnetosphere

M.H. Whang and S.P. Kuo

Department of Electrical Engineering and Computer Science

Polytechnic University

Route 110, Farmingdale, New York 11735

Subject Classifications: 65M05, 65M10, 76W05

Key Words: Finite difference scheme, Stability analysis, Fourier method, Matrix method, Initial value problem

Running head: Stability analyses

Name: M.H. Whang, S.P. Kuo

Address: Polytechnic Univeristy

Dept. EE/CS

Route 110

Farmingdale, N.Y. 11735

Abstract

This work is intended to establish a useful method for studying the coupling and propagation of hydromagnetic waves in the dipole model of the magnetosphere. A numerical scheme for solving a system of two mixed-type coupled partial differential equations having variable coefficients is developed. The stability condition of the scheme has been examined by the Fourier method and matrix method. An initial value problem has then been solved to demonstrate the relevance and applicability of the work to the study of magnetospheric hydromagnetic waves.

I. Introduction

In the study of wave propagation in inhomogeneous magnetoplasma, the physical system is generally characterized by coupled partial differential equations. One specific example is the geomagnetic micropulsation originated by the hydromagnetic waves in the magnetosphere [1-3]. It is shown that these waves in the poloidal and toroidal modes are generally governed by two coupled second order partial differential equations [4, 5]. Though these two equations can be reduced and combined into a single second order ordinary differential equation for a simplified cylindrical model of the magnetosphere [5], there is no apparent way to simplify the system of coupled equations for a more realistic dipole model of the magnetosphere [4] in which a dipole geomagnetic field is assumed. Moreover, the equation for the toroidal mode is shown to be a parabolic type of partial differential equation, while the poloidal mode is elliptic. Both equations have variable coefficients, therefore, for practical applications, there is a considerable interest in finding or developing means of dealing with such a system of two mixed-type coupled partial differential equations with variable coefficients.

Because of the difficulty anticipated and approximations necessary in the analytical methods [6, 7], a numerical approach is, therefore, thought to be more feasibile. Various numerical methods have been developed for dealing with partial differential equations. However, the applicability of each method is mainly determined by its range of stability. As early as the 1960's the energy method had been used to solve certain classes of the partial differential equations with variable coefficients [8, 9]. The range of applicability of the method has also been discussed and demonstrated for limited cases. Thus, the elliptic type partial differential equation with varible coefficients has to be solved by the high-order methods [10, 11]. On the

other hand, the Galerkin method [12] has been shown to be more applicable for dealing with an equation of the form $u_t = P(x, D)u$, where D is a differential operator with respect to x. It is noted that all the above mentioned methods have been developed based on the finite difference techniques.

The Fourier method is widely used for the stability analyses of the finite difference schemes [13, 14]. However, an analytical study of the stability of the difference schemes by the Fourier method was often found to be very complicated or practically impossible. Numerical approaches were thus introduced [15, 16]. In addition to the Fourier method, a matrix method [17, 18] which includes the boundary conditions in the analysis was also suggested for the stability analysis. In the present work, both method will be employed in the stability analyses. The Fourier method will first be used to examine parametrically the stability conditions of the designed scheme. These conditions will then be incorporated in applying the matrix method which is thus used to exemplify the validity of these stability conditions.

For the Fourier method, solutions of the monochromatic wave form are substituted into the difference scheme and the stability boundaries are obtained by von Neumann condition. In the second approach, the difference equations will be arranged into a matrix form $AV_{j+1} = BV_j$, where A and B are matrices and V_{j+1} and V_j are solution vectors at grid number j + 1 and j. The stability of the finite difference approximation is then ensured if the absolute values of all the eigenvalues of $A^{-1}B$ are less than or equal to 1.

In Section II, the coupled hydromagnetic wave equations in the dipole coordinate system are introduced. They represent a set of mixed-type coupled partial differential equations with variable coefficients. The finite difference equations which are derived by a designed numerical scheme for the system of partial differential equations are

presented in Section III, in which the stability analyses by Fourier and matrix method are also presented. As a specific example, the boundary conditions of the wave equations are specified in Section IV. Presented in Section V are the stability conditions of the numerical scheme and the numerical solutions of the wave equations. Finally, a summary and conclusion are in Section VI.

II. Governing Equations

Considered next will be the propagation and coupling of hydromagnetic waves in the magnetosphere. The coupled hydromagnetic wave equations in the dipole model of the magnetosphere are given by [4]

$$H_1H_2 \frac{\partial^2}{\partial\mu^2} \epsilon_\nu + H_1G_2 \frac{\partial}{\partial\mu} \epsilon_\nu + (\frac{\omega^2}{A^2}-m^2H_1)\epsilon_\nu = mH_1 \frac{\partial}{\partial\nu} \epsilon_\phi \tag{1}$$

$$H_1H_2 \frac{\partial^2}{\partial\mu^2} \epsilon_\phi + H_2G_1 \frac{\partial}{\partial\mu} \epsilon_\phi + \left(\frac{\omega^2}{A^2}\right) \epsilon_\phi = -H_2 \frac{\partial^2}{\partial\nu^2} \epsilon_\phi - mH_2 \frac{\partial}{\partial\nu} \epsilon_\nu \tag{2}$$

where (ν, μ, ϕ) form an orthogonal set of the dipole coordinates; ϵ_ν and ϵ_ϕ are the normalized toroidal (shear) and poloidal (compressional) mode fields of the hydromagnetic waves,

$$H_1 = \frac{1}{\nu r^3}, \quad H_2 = \frac{\nu(\nu + 4\mu^2 r^3)}{r}$$

$$G_1 = \frac{\partial H_1}{\partial\mu}, \quad G_2 = \frac{\partial H_2}{\partial\mu}$$

r is related to ν and μ through the equation $\nu r + \mu^2 r^4 = 1$,

$$A^2 = A_o^2 \, (1+3\mu^2 r^4) \, (r)^{n-6}$$

where $A_o = \frac{B_o}{\sqrt{4\pi\rho_o}}$ is the Alfvén speed at the equator of the earth, a model plasma

mass density profile $\rho = \rho_o(r)^{-n}$ the plane of equator is assumed; B_o is the geomagentic field, R_e is the earth's radius, m is the azimuthal (i.e. east-west direction) mode number and ω is eigenfrequency of waves.

Equations (1) and (2) constitute a set of mixed-type coupled partial differential equations with variable coefficients. Equation (1) is a parabolic type of P.D.E., while Eq. (2) is an elliptic type. For the convenience of the following analysis, Equations (1) and (2) are rewritten as

$$P_\nu = a_1(\mu,\nu)T_{\mu\mu} + a_2(\mu,\nu)T\mu + a_3(\mu,\nu)T \tag{3}$$

$$[1-a_1(\mu,\nu)b_4 \frac{\partial^2}{\partial\mu^2} -a_2(\mu,\nu)b_4 \frac{\partial}{\partial\mu} -a_3(\mu,\nu)b_4]T_\nu$$

$$= b_1(\mu,\nu)P_{\mu\mu} + b_2(\mu,\nu)P_\mu + b_3(\mu,\nu)P + a_{1_\nu}(\mu,\nu)b_4T_{\mu\mu} + a_{2_\nu}(\mu,\nu)b_4T_\mu + a_{3_\nu}(\mu,\nu)b_4T \tag{4}$$

where $P \Leftrightarrow \epsilon_\phi$, $T \Leftrightarrow \epsilon_\nu$

$$a_1 = \frac{H_2}{m}, \quad a_2 = \frac{G_2}{m}, \quad a_3 = \frac{1}{mH_1}\left(\frac{\omega^2}{A^2} - m^2H_1\right)$$

$$b_1 = -\frac{H_1}{m}, \quad b_2 = -\frac{G_1}{m}, \quad b_3 = -\frac{1}{mH_2}\left(\frac{\omega^2}{A^2}\right) \quad b_4 = -\frac{1}{m}$$

$$x_\mu = \frac{\partial}{\partial \mu} x,\ x_\nu = \frac{\partial}{\partial \nu} x,\ x = P, T,\ a_1,\ a_2,\ a_3$$

There is no apparent way to solve (3) and (4) analytically. A numerical approach is therefore employed in the present study.

III. Finite difference discretization and stability analyses

The governing Eq. (3) and (4) are approximated on a non-staggered grid with grid increments $\Delta\mu$ and $\Delta\nu$. Both the computational grids used are carefully chosen to ensure an algebraic system of equations that reach second order accuracy. The standard two and three-point centered difference formulas to approximate first and second derivatives with respect to μ and ν are applied in this finite difference discretization. Moreover, a parameter θ valued in the range (0, 1) is introduced as a weighting factor into the system of difference equations. Thus, the numerical scheme of the difference equations can change from fully implicit ($\theta = 1$) to fully explicit ($\theta = 0$). Based on the above discussion, the resulting finite difference equations converted from (3) and (4) become

$$P_i^{j+1} - \left(\frac{2\Delta\nu}{\Delta\mu^2}\ \theta\ a_{1_{i+1}}^j + \frac{\Delta\nu}{\Delta\mu}\ \theta\ a_{2_i}^j \right) T_{i+1}^{j+1} + \left(\frac{4\Delta\nu}{\Delta\mu^2}\ \theta\ a_{1_i}^j - 2\Delta\nu\theta\ a_{3_i}^j \right) T_i^{j+1}$$

$$- \left(\frac{2\Delta\nu}{\Delta\mu^2}\ \theta\ a_{1_i}^j - \frac{\Delta\nu}{\Delta\mu}\ \theta a_{2_i}^j \right) T_{i-1}^{j+1}$$

$$= P_i^{j-1} + \left[\frac{2\Delta\nu}{\Delta\mu^2} (1-\theta)\ a_i^j \quad + \frac{\Delta\nu}{\Delta\mu} (1-\theta)\ a_{2_i}^j \quad \right] T_{i+1}^{j-1}$$

$$- \left[\frac{\Delta\nu}{\Delta\mu^2} (1-\theta)\ a^j{}_{1_i} \ -2(1-\theta)\Delta\nu a^j{}_{3_i} \right] T_i^{j-1} + \left[\frac{2\Delta\nu}{\Delta\mu^2} (1-\theta)\ a_{1_i}^j \quad - \frac{\Delta\nu}{\Delta\mu} (1-\theta) a_{2_i}^j \quad \right] T_{i-1}^{j-1} \quad (5)$$

$$(1-a^j{}_{3_i}\ b_4 - 2\Delta\nu\theta\ a_{3\nu_i}^i\ b_4 + \frac{2}{\Delta\mu^2} a^j{}_{1_i}\ b_4 + 4\ \frac{\Delta\nu}{\Delta\mu^2}\ \theta\ a_{1\nu_i}^j\ b_4) T_i^{j+1}$$

$$-(\frac{1}{\Delta\mu^2}\ a_{1_i}^j \quad b_4 + \frac{1}{2\Delta\mu}\ a_{2_i}^j \quad b_4 + \frac{2\Delta\nu}{\Delta\mu^2}\ \theta\ a_{i\nu_i}^j \quad b_4 + \frac{\Delta\nu}{\Delta\mu}\ \theta\ a_{2\nu_i}^j \quad b_4) T_{i+1}^{j+1}$$

$$-(\frac{1}{\Delta\mu^2}\ a_{1_i}^j \quad b_4 - \frac{1}{2\Delta\mu}\ a_{2_i}^j \quad b_4 + \frac{2\Delta\nu}{\Delta\mu^2}\ \theta\ a_{1\nu_i}^j \quad b_4 - \frac{\Delta\nu}{\Delta\mu}\ \theta\ a_{2\nu_i}^j \quad b_4) T_{i-1}^{j+1}$$

$$-\left(\frac{2\Delta\nu}{\Delta\mu^2}\ \theta\ b_{1_i}^j \quad + \frac{\Delta\nu}{\Delta\mu}\ \theta\ b_{2_i}^j \quad \right) P_{i+1}^{j+1}$$

$$+ \left(4\ \frac{\Delta\nu}{\Delta\mu^2}\ \theta\ b^j{}_{1_i} \ -2\Delta\nu\ \theta\ b^j{}_{3_i} \right) P_i^{j+1}$$

$$-\left(\frac{2\Delta\nu}{\Delta\mu^2}\ \theta\ b_{1_i}^j \quad - \frac{\Delta\nu}{\Delta\mu}\ \theta\ b_{2_i}^j \quad \right) P_{i-1}^{j+1}$$

$$= \left[1 + \frac{2}{\Delta\mu^2}\ a^j{}_{1_i} b_4 - a^j{}_{3_i} b_4 - \frac{4\Delta\nu}{\Delta\mu^2}(1-\theta) a_{1\nu_i}^j b_4 + 2\Delta\nu(1-\theta)\ a_{3\nu_i}^j b_4 \right] T_i^{j-1}$$

$$- \left[\frac{1}{\Delta\mu^2}\ a_{1_i}^j \quad b_{4_i}^j \quad + \frac{1}{2\Delta\mu}\ a_{2_i}^j \quad b_4 - \frac{2\Delta\nu}{\Delta\mu^2} (1-\theta)\ a_{1\nu_i}^j \quad b_4 - \frac{\Delta\nu}{\Delta\mu} (1-\theta)\ a_{2\nu_i}^j \quad b_4 \right] T_{i+1}^{j-1}$$

$$- \left[\frac{1}{\Delta\mu^2}\ a_{1_i}^j \quad b_4 \quad - \frac{1}{2\Delta\mu}\ a_{2_i}^j \quad b_4 - \frac{2\Delta\nu}{\Delta\mu^2} (1-\theta)\ a_{1\nu_i}^j \quad b_4 \quad + \frac{\Delta\nu}{\Delta\mu} (1-\theta)\ a_{2\nu_i}^j \quad b_4 \right] T_{i-1}^{j-1}$$

$$+ \left[\frac{2\Delta\nu}{\Delta\mu^2} (1-\theta)\ b^j_{1_i} + \frac{\Delta\nu}{\Delta\mu} (1-\theta)\ b^j_{2_i} \right] P^{j-1}_{i+1}$$

$$- \left[\frac{4\Delta\nu}{\Delta\mu^2} (1-\theta)\ b^j_{1_i} - 2\Delta\mu(1-\theta)\ b^j_{3_i} \right] P^{j-1}_{i}$$

$$+ \left[\frac{2\Delta\nu}{\Delta\mu^2} (1-\theta)\ b^j_{1_i} - \frac{\Delta\nu}{\Delta\mu} (1-\theta)\ b^j_{2_i} \right] P^{j}_{i-1} \qquad (6)$$

where i: $1 \rightarrow I-1$ and j : $1 \rightarrow J-1$

Two methods are used to establish the stability conditions of the finite difference scheme which converts the differential equations (3) and (4) into the finite difference equations (5) and (6).

A. Fourier method

In this method, the independent solutions of the difference equations are all of the forms $P^j_l = \hat{P}^j e^{ikl\Delta\mu}$ and $T^j_l = \hat{T}^j e^{ikl\Delta\mu}$ where k is a real spatial wave number which can have any value. Using these expressions for P^j_l and T^j_l in (5) and (6), yields

$$\hat{P}^{j+1} + \theta\ F_1 \hat{T}^{j+1} = \hat{P}^j + (1-\theta) F_1 \hat{T}^j \qquad (7)$$

$$\theta\ F_2 \hat{P}^{j+1} + F_3 \hat{T}^{j+1} = (1-\theta) F_2 \hat{P}^j + F_4 \hat{T}^j \qquad (8)$$

where $F_1 = \left[a_1 \frac{4\Delta\nu}{\Delta\mu^2} (\cos k\Delta\mu - 1) + 2a_3\Delta\nu + i(2a_2 \frac{\Delta\nu}{\Delta\mu} \sin k\Delta\mu) \right]$

$$F_2 = -\left[b_1 \frac{4\Delta\nu}{\Delta\mu^2} (\cos k\Delta\mu - 1) + 2b_3\Delta\nu + i(2b_2 \frac{\Delta\nu}{\Delta\mu} \sin k\Delta\mu) \right]$$

$$F_3 = \{(1-a_3b_4) - a_1b_4 \frac{2}{\Delta\mu^2}(\cos k\Delta\mu - 1) - \theta[a_{1\nu}b_4 \frac{4\Delta\nu}{\Delta\mu^2}(\cos k\Delta\mu - 1) + 2a_{3\nu}b_4\Delta\nu]$$

$$- i(a_2b_4 \frac{\sin k\Delta\mu}{\Delta\mu} + 2a_{2\nu}b_4 \frac{\Delta\nu}{\Delta\mu} \sin k\Delta\mu)\}$$

and

$$F_4 = \{(1-a_3b_4) - a_1b_4 \frac{2}{\Delta\mu^2} (\cos k\Delta\mu - 1) + (1-\theta)[a_{1\nu}b_4 \frac{2\Delta\nu}{\Delta\mu^2}(\cos k\Delta\mu - 1) + a_{3\nu}b_4\Delta\nu]$$

$$- i [a_2b_4 \frac{\sin k\Delta\nu}{\Delta\mu} - 2(1-\theta)a_{2\nu}b_4 \frac{\Delta\nu}{\Delta\mu} \sin k\Delta\mu])$$

The coefficients a_1, a_2, a_3, $a_{1\nu}$, $a_{2\nu}$, $a_{3\nu}$, b_1, b_2 and b_3 in the above expressions are evaluated at $\mu = l\Delta\mu$ and $\nu = j\Delta\nu$. Eq. (7) and (8) can then be expressed in the matrix form as

$$\begin{bmatrix} 1 & \theta F_1 \\ \theta F_2 & F_3 \end{bmatrix} \begin{bmatrix} \hat{p}^{j+1} \\ \hat{v}^{j+1} \end{bmatrix} = \begin{bmatrix} 1 & (1-\theta)F_1 \\ (1-\theta)F_2 & F_4 \end{bmatrix} \begin{bmatrix} \hat{p}^{j} \\ \hat{v}^{j} \end{bmatrix} \qquad (9)$$

which leads the amplification matrix

$$G = \begin{bmatrix} \dfrac{F_3-\theta(1-\theta)F_1F_2}{F_3-\theta^2F_1F_2} & \dfrac{(1-\theta)F_1F_3-\theta F_1F_4}{F_3-\theta^2F_1F_2} \\ \dfrac{(1-2\theta)F_2}{F_3-\theta^2F_1F_2} & \dfrac{F_4-\theta(1-\theta)F_1F_2}{F_3-\theta^2F_2F_2} \end{bmatrix}$$

The definition of stability here is the classical von Neumann stability condition which requires that the norm of the amplification matrix have to be less than or equal to 1. It is noted that the amplification matrix has to be determined for every grid point because of the variable coefficients appeared in the coupled equations of the present study. The norm of the amplification matrix at each grid point is then evaluated numerically. The result of a parametric stability analysis obtained by varying the parameters $\Delta\mu$, $\Delta\nu$ and θ will be presented in Section II evaluated numerically.

B. Matrix method:

By transforming the difference equations (5) and (6) into a heptagiagonal matrix form, it reads

$$A^{j+1}E^{j+1} = B^{j-1}E^{j-1} \tag{9}$$

where

$$
A^{j+1} = \left\{ \begin{array}{cccccccccc}
1 & \alpha^{j+1}_{2,1} & 0 & \alpha^{j+1}_{1,1} & & & & & & \\
\beta^{j+1}_{5,1} & \beta^{j+1}_{1,1} & \beta^{j+1}_{4,1} & \beta^{j+1}_{2,1} & & & & & & \\
 & \alpha^{j+1}_{3,2} & 1 & \alpha^{j+1}_{2,2} & 0 & \alpha^{j+1}_{1,2} & & & & \\
\beta^{j+1}_{6,2} & \beta^{j+1}_{3,2} & \beta^{j+1}_{5,2} & \beta^{j+1}_{1,2} & \beta^{j+1}_{4,2} & \beta^{j+1}_{2,2} & & & & \\
 & & & \alpha^{j+1}_{3,3} & 1 & \alpha^{j+1}_{2,3} & 0 & \alpha^{j+1}_{1,3} & & \\
 & & \beta^{j+1}_{6,3} & \beta^{j+1}_{3,2} & \beta^{j+1}_{5,2} & \beta^{j+1}_{1,3} & \beta^{j+1}_{4,3} & \beta^{j+1}_{2,3} & & \\
 & & & \ddots & \ddots & \ddots & \ddots & \ddots & \ddots & \\
 & & & & & \alpha^{j+1}_{3,I-2} & 1 & \alpha^{j+1}_{2,I-2} & \alpha^{j+1}_{1,I-2} & \\
 & & & \beta^{j+1}_{6,I-2} & \beta^{j+1}_{3,I-2} & \beta^{j+1}_{5,I-2} & \beta^{j+1}_{1,I-2} & \beta^{j+1}_{4,I-2} & \beta^{j+1}_{2,I-2} & \\
 & & & & & & \alpha^{j+1}_{3,I-1} & 1 & \alpha^{j+1}_{2,I-1} & \\
 & & & & & & \beta^{j+1}_{6,I-1} & \beta^{j+1}_{5,I-1} & \beta^{j+1}_{1,I-1} &
\end{array} \right\}
$$

$$
\left\{
\begin{array}{cccccccccccc}
1 & \gamma_{2,1}^{j+1} & 0 & \gamma_{1,1}^{j-1} & & & & & & & & \\
\delta_{5,1}^{j-1} & \delta_{1,1}^{j-1} & \delta_{4,1}^{j-1} & \delta_{2,1}^{j-1} & & & & & & & & \\
 & \gamma_{3,2}^{j-1} & 1 & \gamma_{2,2}^{j-1} & 0 & \gamma_{1,2}^{j-1} & & & & & & \\
\delta_{6,2}^{j-1} & \delta_{3,2}^{j-1} & \delta_{5,2}^{j-1} & \delta_{1,2}^{j-1} & \delta_{4,2}^{j-1} & \delta_{2,2}^{j-1} & & & & & & \\
 & & & \gamma_{3,3}^{j-1} & 1 & \gamma_{2,3}^{j-1} & 0 & \gamma_{1,3}^{j-1} & & & & \\
 & & \delta_{6,3}^{j-1} & \delta_{3,3}^{j-1} & \delta_{5,3}^{j-1} & \delta_{1,3}^{j-1} & \delta_{4,3}^{j-1} & \delta_{2,3}^{j-1} & & & & \\
 & & & & & & & & \ddots & & & \\
 & & & & & & & & & \gamma_{3,I-2}^{j-1} & 1 & \gamma_{2,I-2}^{j-1} & 0 & \gamma_{1,I-2}^{j-1} \\
 & & & & & & & & \delta_{6,I-2}^{j-1} & \delta_{3,I-2}^{j-1} & \delta_{5,I-2}^{j-1} & \delta_{1,I-2}^{j-1} & \delta_{4,I-2}^{j-1} & \delta_{2,I-2}^{j-2} \\
 & & & & & & & & & & & \gamma_{3,I-1}^{j-1} & 1 & \gamma_{2,I-1}^{j-1} \\
 & & & & & & & & & & & \delta_{6,I-1}^{j-1} & \delta_{5,I-1}^{j-1} & \delta_{1,I-1}^{j-1}
\end{array}
\right\}
$$

$$E^{j+1} = \begin{bmatrix} P_1^{j+1} \\ T_1^{j+1} \\ P_2^{j+1} \\ T_2^{j+1} \\ \cdot \\ \cdot \\ \cdot \\ \cdot \\ \cdot \\ P_{I-1}^{j+1} \\ T_{I-1}^{j+1} \end{bmatrix}$$

$$E^{j-1} = \begin{bmatrix} P_1^{j-1} \\ T_1^{j-1} \\ P_2^{j-1} \\ T_2^{j-1} \\ \cdot \\ \cdot \\ \cdot \\ \cdot \\ \cdot \\ P_{I-1}^{j-1} \\ T_{I-1}^{j-1} \end{bmatrix}$$

where $\alpha_{1,i}^{j+1} = -\left(\frac{2\Delta\nu}{\Delta\mu^2} \theta \, a_{1_i}^{j} + \frac{\Delta\nu}{\Delta\mu} \theta \, a_{2_i}^{j} \right)$

$$\alpha^{j+1}_{2,i} = \frac{4\Delta\nu}{\Delta\mu^2}\,\theta\; a^{j}{}_{1_i} \;-2\Delta\nu\theta\; a^{i}{}_{3_i}$$

$$\alpha^{j+1}_{3,i} = -\left(\frac{2\Delta\nu}{\Delta\mu^2}\,\theta\; a^{j}_{1_i} \;-\; \frac{2\Delta\nu}{\Delta\mu}\,\theta\; a^{j}_{2_i} \right)$$

$$\beta^{j+1}_{1,i} = 1-a^{j}_{3_i}\;\; b_4 \;-2\Delta\nu\theta\; a^{j}_{3\nu_i} b_4 \;+\; \frac{2}{\Delta\mu^2}\, a^{j}{}_{1_i}\, b_4 \;+\; 4\frac{\Delta\nu}{\Delta\mu^2}\,\theta a^{j}_{1\nu_i} b_4$$

$$\beta^{j+1}_{2,i} = -\left(\frac{1}{\Delta\mu^2}\, a^{j}_{1_i} \;\; b_4 \;+\; \frac{1}{2\Delta\mu}\, a^{j}_{2_i} \;\; b_4 \;+\; \frac{2\Delta\nu}{\Delta\mu^2}\,\theta\; a^{j}_{1\nu_i} \;\; b_4 \;+\; \frac{\Delta\nu}{\Delta\mu}\,\theta a^{j}_{2\nu_i} \;\; b_4 \right)$$

$$\beta^{j+1}_{3,i} = -\left(\frac{1}{\Delta\mu^2}\, a^{j}_{1_i} \;\; b_4 \;-\; \frac{1}{2\Delta\mu}\, a^{j}_{2_i} \;\; b_4 \;+\; \frac{2\Delta\nu}{\Delta\mu^2}\,\theta\; a^{j}_{1\nu_i} \;\; b_4 \;-\; \frac{\Delta\nu}{\Delta\mu}\,\theta\; a^{j}_{2\nu_i} \;\; b_4 \right)$$

$$\beta^{j+1}_{4,i} = -\left(\frac{2\Delta\nu}{\Delta\mu^2}\,\theta\; b^{j}_{1_i} \;+\; \frac{\Delta\nu}{\Delta\mu}\,\theta\; b^{j}_{1_i} \right)$$

$$\beta^{j+1}_{5,i} = 4\;\frac{\Delta\nu}{\Delta\mu^2}\,\theta\; b^{j}{}_{1_i} \;-2\Delta\nu\theta\; b^{j}{}_{3_i}$$

$$\beta^{j+1}_{6,i} = -\left(\frac{2\Delta\nu}{\Delta\mu^2}\,\theta\; b^{j}_{1_i} \;-\; \frac{\Delta\nu}{\Delta\mu}\,\theta\; b^{j}_{2_i} \right)$$

$$\gamma^{j-1}_{1,i} = \frac{2\Delta\nu}{\Delta\mu^2}\,(1-\theta) a^{j}_{1_i} \;+\; \frac{\Delta\nu}{\Delta\mu}\,(1-\theta) a^{j}_{2_i}$$

$$\gamma^{j-1}_{2,i} = -\left[\frac{4\Delta\nu}{\Delta\mu^2}\,(1-\theta) a^{j}{}_{1_i} \;-2\;(1-\theta)\Delta\nu\; a^{j}{}_{3_i} \right]$$

$$\gamma^{j-1}_{3,i} = \frac{2\Delta\nu}{\Delta\mu^2}\,(1-\theta) a^{j}_{1_i} \;\; -\frac{\Delta\nu}{\Delta\mu}\,(1-\theta) a^{j}_{2_i}$$

$$\delta^{j-1}_{1,i} = 1 \;+\; \frac{2}{\Delta\mu^2}\, a^{j}{}_{1_i}\, b_4 \;-a^{j}_{3_i}\, b_4 \;-\frac{4\Delta\nu}{\Delta\mu^2}\,(1-\theta) a^{j}_{1\nu_i} b_4 \;+\; 2\Delta\nu(1-\theta) a^{j}_{3\nu_i} b_4$$

$$\delta^{j-1}_{2,i} = -\left[\frac{1}{\Delta\mu^2} a^j_{1_i} \; b_4 + \frac{1}{2\Delta\mu} a^j_{2_i} \; b_4 - \frac{2\Delta\nu}{\Delta\mu^2}(1-\theta)a^j_{1\nu_i} - \frac{\Delta\nu}{\Delta\mu}(1-\theta)a^j_{2\nu_i} \; b_4 \right]$$

$$\delta^{i-1}_{3,i} = -\left[\frac{1}{\Delta\mu^2} a^j_{1_i} \; b_4 - \frac{1}{2\Delta\mu} a^j_{2_i} \; b_4 - \frac{2\Delta\nu}{\Delta\mu^2} (1-\theta)a^j_{1\nu_i} \; b_4 + \frac{\Delta\nu}{\Delta\mu} (1-\theta)a^j_{2\nu_i} \; b_4 \right]$$

$$\delta^{j-1}_{4,i} = \frac{2\Delta\nu}{\Delta\mu^2} (1-\theta)b^j_{1_i} + \frac{\Delta\nu}{\Delta\mu} (1-\theta)b^j_{2_i}$$

$$\delta^{j-1}_{5,i} = -\left[\frac{4\Delta\nu}{\Delta\mu^2}(1-\theta)b^j_{1_i} - 2\Delta\nu \; (1-\theta)b^j_{4_i} \right]$$

$$\delta^{j-1}_{6,i} = \frac{2\Delta\nu}{\Delta\mu^2} (1-\theta)b^j_{1_i} - \frac{\Delta\nu}{\Delta\mu} (1-\theta)b^j_{2_i}$$

Matrices A and B have dimension 2(I-1)x2(I-1), while matrix E has dimension 2(I-1)x1. The stability of the scheme is then governed by the norm of the matrix $A^{-1}B$.

V. Boundary conditions

In the magnetosphere, the inner boundary is located at the outside edge of the ionosphere ($r = 2R_e$), while the outside boundary is at the magnetopause ($r = 10R_e$). We thus have the inner boundary at $\nu = 0.5$ and outer boundary at $\nu = 0.1$. The other two boundaries are the north pole ($\mu = 0.25$) and south pole ($\mu = -0.25$). These boundaries define the region $-0.25 \leq \mu \leq 0.25$ and $0.1 \leq \nu \leq 0.5$ for the magentosphere.

Assuming that the ionosphere is a perfect conductor, hence, the tangential components of electric field at the inner boundary are equal to zero, which lead to the fixed boundary conditions: $P(\nu, \mu = \pm 0.25) = 0 = T(\nu, \mu = \pm 0.25)$. The boundary conditions at the magnetopause $P(\nu = 0.1, \mu)$ and $T(\nu = 0.1, \mu)$ are, in general, imposed by the external source such as the solar wind. They can thus be assumed to be any funcitons of μ for different physical situation. In the present work, we set the boundary conditions at $\nu = 0.1$ to be

$$P(0.1, \mu) = P_o(\mu) = |\sin(4\pi h\mu)|$$

$$T(0.1, \mu) = 0$$

where $P_o(\mu)$ is a spatially distributed sinusoidal perturbation; h is the harmonic number of sinusoidal perturbation; T = 0 is for the practical reason since the perturbations in the frequency range of the toroidal mode at the outer boundary cannot propagate into the magnetosphere.

The frequency ω is given to be $2\pi \times 0.002H_z$ by the experimental data [19]. Two extreme cases with the azimuthal wave number m = 20 and 100 respectively will be considered consistent with the observations ($|m| = 20 - 100$) [19-22]. We will also assume a reasonable density index n = 3 in the numerical analysis. The stability conditions of the numerical scheme and numerical solutions will be determined by using these boundary conditions and parameter values.

VI. Results

In order to find the stability conditions by Fourier method which is described in Section III A, the eigenvalues of amplification matrix G are evaluated at every grid point. By varying the parameters $\Delta\mu$, $\Delta\nu$ and θ, the roots of a second order equation defined by the eigenvalue equation are determined iteratively to satisfy the von Newmann stability condition which requires the absolute values of both

roots to be less than or equal to 1. Fig. 1 shows the ν dependence of the maximum absolute value of both roots of the second order equation over the entire range [-0.25, 0.25] of μ for several different θ values and for the case m = 100, where $\Delta\mu$ = 0.004 and $\Delta\nu$ = 0.01334 are chosen for the reason stated in the following. It should be pointed out that only θ and $\Delta\nu$ are the sensitive factors in the scheme. Because the grid number in the μ direction will be the dimension of the matrices A and B of Eq. (9) used for the analysis of the matrix method. Hence, $\Delta\mu$, the grid size in the μ direction, is limited by the memory size of the computer, and determined reasonably to be 0.004. In other words, the dimension of the matrices A and B is set to be 248 x 248 and the program is executed in the Cray X-MP/48 of the Pittsburgh supercomputing center. As shown in Fig. 1, the larger θ is used in the scheme, the more stable scheme can be found. Therefore, the fully implicit scheme (θ = 1) will be chosen to be the second parameter. For the accuracy of the numerical solution, there is a need to find the minimum $\Delta\nu$ in the numerical scheme. By specifying $\Delta\mu$ = 0.004 and θ = 1, the functional dependence of the maximum eigenvalue of amplification matrix G on ν for different $\Delta\nu$ values is shown in Fig. 2. From this analysis, the minimum $\Delta\nu$ = 0.01334 is determined. We next apply the matrix method to examine the stability conditions obtained by the Fourier method. As shown in Fig. 3, all of the eigenvalues of the matrix $A^{-1}B$ in Eq. (9) are found to be less than 1. Therefore, the designed numerical scheme has been proven to be stable consistently by Fourier and matrix method. In other words, a viable numerical algorithm dealing with the mixed-type coupled partial differential equations with variable coeffients has been developed.

Presented in Figs. 4 and 5 are the three dimensional plots for the results of $\epsilon_\phi(\nu, \mu)$ and $\epsilon_\nu(\nu, \mu)$, where h = 2 is assumed. Using the relations [23,

24] derived from Faraday's law

$$B_\nu = \frac{i}{\omega} \frac{\nu + 4\mu^2 r^3}{r^4 \nu} \frac{\partial \epsilon_\phi}{\partial \mu} = \frac{i}{\omega} \tilde{B}_\nu \tag{10}$$

$$B_\mu = -\frac{i}{\omega} \left\{ \frac{[r(\nu + 4\mu^2 r^3)]^{1/2}}{r^3} \right\} \left(\frac{\partial \epsilon_\phi}{\partial \nu} - im\epsilon_\nu \right) = -\frac{i}{\omega} \tilde{B}_\mu \tag{11}$$

$$B_\phi = -\frac{i}{\omega} \left[\frac{\nu^{1/2}(\nu + 4\mu^2 r^3)}{r^{7/2}} \right] \frac{\partial \epsilon_\nu}{\partial \mu} = -\frac{i}{\omega} \tilde{B}_\phi \tag{12}$$

the corresponding components of magnetic field perturbation $\tilde{B}_\nu$, $\tilde{B}_\phi$ and $|\tilde{B}_\mu|$ are also obtained and presented in figures 6-8, where $\frac{\partial \epsilon_\phi}{\partial \nu} = 1 \times 10^{-5}$ is assumed at the magnetopause. Using the same procedure for the stability analysis for m = 20 case, the optimum $\Delta\nu = 0.028$ is found. It is then incorporated in the numerical scheme in solving (1) and (2) for m = 20. The results of ϵ_ϕ and ϵ_ν together with B_ν, B_μ and B_ϕ obtained through (10)-(12) are presented in Figs. 9-13. The results show that the field line resonance (toroidal) mode ($\epsilon_\nu, B_\phi, B_\mu$) can be excited inside the magnetosphere through the coupling with the global cavity (poloidal) mode (ϵ_ϕ, B_ν) initiated by the perturbation appeared on the outer boundary of the magnetosphere (i.e., magnetopause). The field line resonance mode appears to be a localized oscillation as expected. For m = 20, the peak of the oscillation is located along $\nu = 0.23$. It moves outward to $\nu = 0.13$ when m is increased to 100. It is noted that, for m = 100 case, the frequency considered is too low for the globe mode to propagate in the magnetosphere. Nevertheless, through the tunneling effect the field line resonance mode can still be excited by coupling to the

excited by coupling to the decay part of the globe mode oscillation.

VII. Summary and Conclusion

A numerical algorithm dealing with the mixed-type coupled partial differential equations with variable coefficients has been developed. The stability of the numerical scheme has been examined and solutions for the hydromagnetic wave equations are obtained on non-staggered grids by this algorithm. The main contribution of this algorithm is to offer an efficient way to examine the stability conditions first by the Fourier method and then check them by the matrix method. Since these two methods are different, one can be sure of the stability conditions. Moreover, this algorithm leads a way for a parametric study of the stability conditions. It also becomes an advantage in the sense that the optimum parameters which can increase the accuracy of the numerical solution can be determined together with the stability analyses. Using the developed numerical scheme, the problem of coupling and propagation of hydromagnetic waves in the realistic dipole model of the magnetosphere can be studied. An example has been considered. The results are presented in Figs. 4-13.

Acknowledgement

We are grateful to Dr.J. Bentson for valuable discussions and suggestions. This work is supported by the Air Force Office of Scientific Research Grant No. AFOSR-85-0133 and AFOSR-88-0127. The numerical work was performed at the Pittsburgh Supercomputing center, supported by the National Science Foundation.

References

1. J. W. Dungey, in Physics of Geomagnetic Phenomena, Vol. 2, edited by S. Matsushita and W.H. Campbell (Academic, New York, 1967), p. 913.
2. J.W. Dungey, Physics of the Magnetosphere, edited by R.L. Carovillano et al. (D. Reidel, Dordrecht, Holland, 1968). p. 218.
3. J.A. Jacobs, Geomagnetic Micropulsations (Springer, New York, 1970), p. 126.
4. H.R. Radoski, J. Geophys. Res., 72, 1, 418 (1967).
5. S.P. Kuo, M.C. Lee and A. Wolfe, J. Plasma Physics, 38, 2, 235 (1987).
6. H.R. Radoski, J. Geomag. Geoelectr. 25, 363 (1973).
7. H.R. Radoski, J. Geophys. Res., 78, 4, 595 (1974).
8. P.D. Lax and B. Wendroff, Comm. Pure Appl. Math., 13, 217 (1960).
9. H.O. Kreiss, Numer. Math., 5, 24 (1963).
10. D.M. Young and J.H. Danwalder, in Error in Digital Computation, edited by L. Rall, (Academic, New York, 1965). p. 181.
11. U. Ananthakrishnaiah, R. Manohar and J.W. Stephenson, Numerical Math. for Partial Differential Equations, 3, 219 (1987).
12. D. Gottlieb and S.A. Orszag, Numerical Analysis of Spectral Methods: Theory and Applications (SIAM, Philadelphia, 1986).
13. D. Potter, Computational Physics (Wiley-Interscience, London, 1972), p. 13.
14. R.D. Richtmyer and K.W. Morton, Difference Methods for Initial-Value Problems (Wiley-Interscience, New York, 1967). p. 9.
15. G. Hall and J.M. Watt, Modern Numerical Methods for Ordinary Differential Equations (Clarendon Press, Oxford, 1976).
16. T.F. Chan, SIAM J. Num. Anal. 21, 272 (1984).

17. W.F. Ames, Numerical Methods for Partial Differential Equations (Academic Press, New York, 1977), p. 56.

18. D.A. Anderson, J.C. Tannehill and R.H. Pletcher, Computational Fluid Mechanics and Heat Transfer (Hemisphere Publishing Corporation, New York, 1984) p.80

19. K. Takahashi, J.F. Fennell, E. Amata and P.R. Higbie, J. Geophys. Res., 92, A6, 5857 (1987).

20. A.D.M. Walker, R.A. Greenwald, A. Korth and G. Kremser, J. Geophys. Res., 87, 9135 (1982).

21. K. Takahashi, P.R. Higbie and D.N. Baker, J. Geophys. Res., 90, 1493 (1985).

22. C.S. Lin and J.N. Barfield, J. Geophys. Res., 90, 11075 (1985).

23. W.D. Cumming, R.J. O'Sullivan, and R.J. Coleman, J. Geophys. Res. 74, 3, 778 (1969).

24. M.H. Whang and S.P. Kuo, EOS Transactions, 68, 16, 393 (1987).

Figure Captions

Fig. 1. Maximum eigenvalue evaluated by the Fourier method along the ν axis at $\Delta\mu = 0.004$, $\Delta\nu = 0.01334$ for different θ.

Fig. 2. Maximum eigenvalue evaluated by the Fourier method along the ν axis at $\Delta\mu = 0.004$, $\theta = 1$ for different $\Delta\nu$.

Fig. 3. Maximum eigenvalue evaluated by the Matrix method along the ν axis at $\theta = 1$, $\Delta\mu = 0.004$, $\Delta\nu = 0.01334$.

Fig. 4. Normalized electric field of poloidal mode (m = 100).

Fig. 5. Normalized electric field of toroidal mode (m = 100).

Fig. 6. Normalized magnetic field of poloidal mode (radial component) (m = 100).

Fig. 7. Normalized magnetic field of toloidal mode (N-S component) (m = 100).

Fig. 8. Normalized magnetic field of toroidal mode (E-W component) (m = 100).

Fig. 9. Normalized electric field of poloidal mode (m = 20).

Fig. 10. Normalized electric field of toroidal mode (m = 20).

Fig. 11. Normalized magnetic field of poroidal mode (radial component) (m = 20).

Fig. 12. Normalized magnetic field of toroidal mode (N-S component) (m = 20).

Fig. 13. Normalized magnetic field of toroidal mode (E-W component) (m = 20).

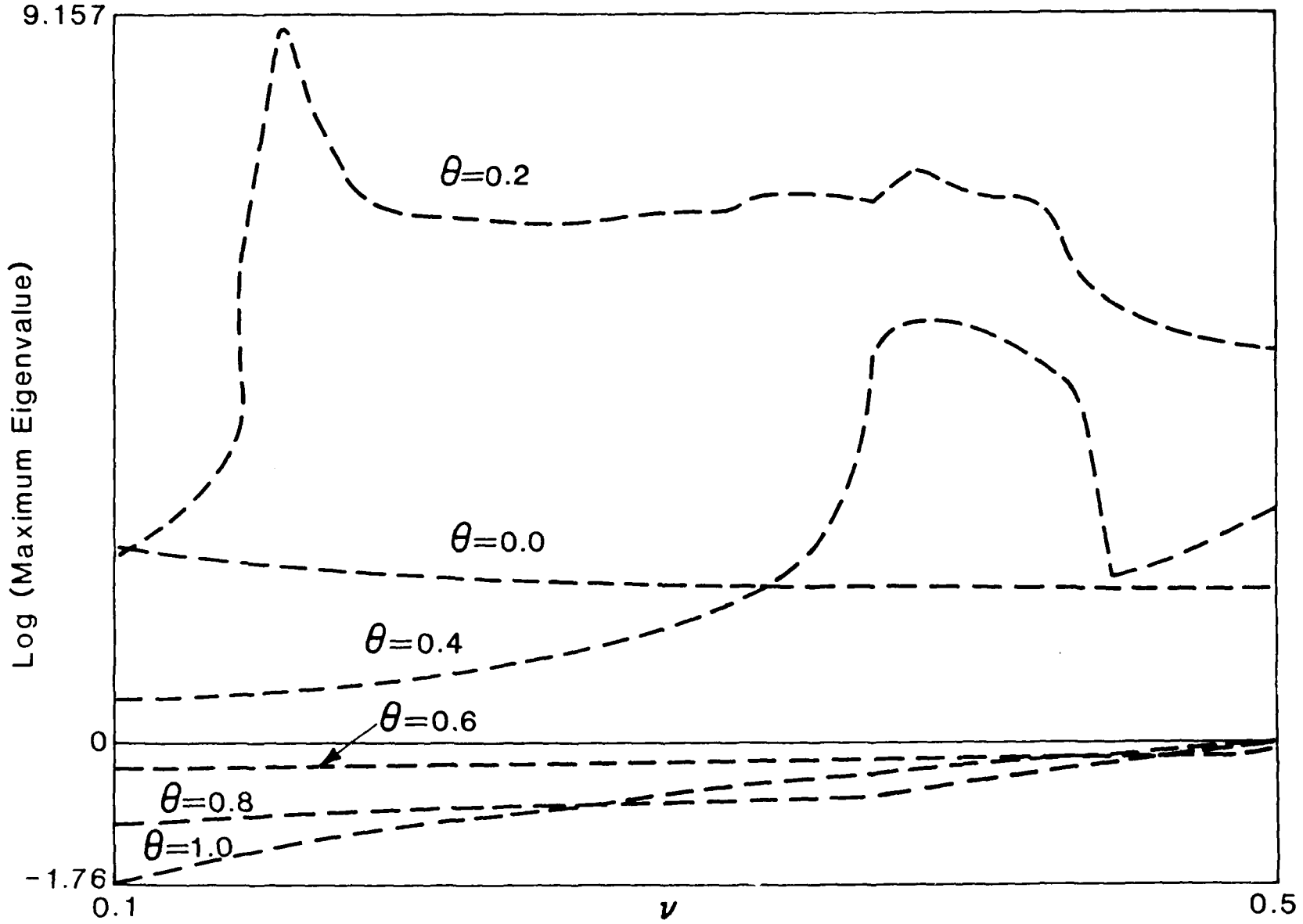

Fig. 1. Maximum eigenvalue evaluated by the Fourier method along the ν axis at $\Delta\mu = 0.004$, $\Delta\nu = 0.01334$ for different θ.

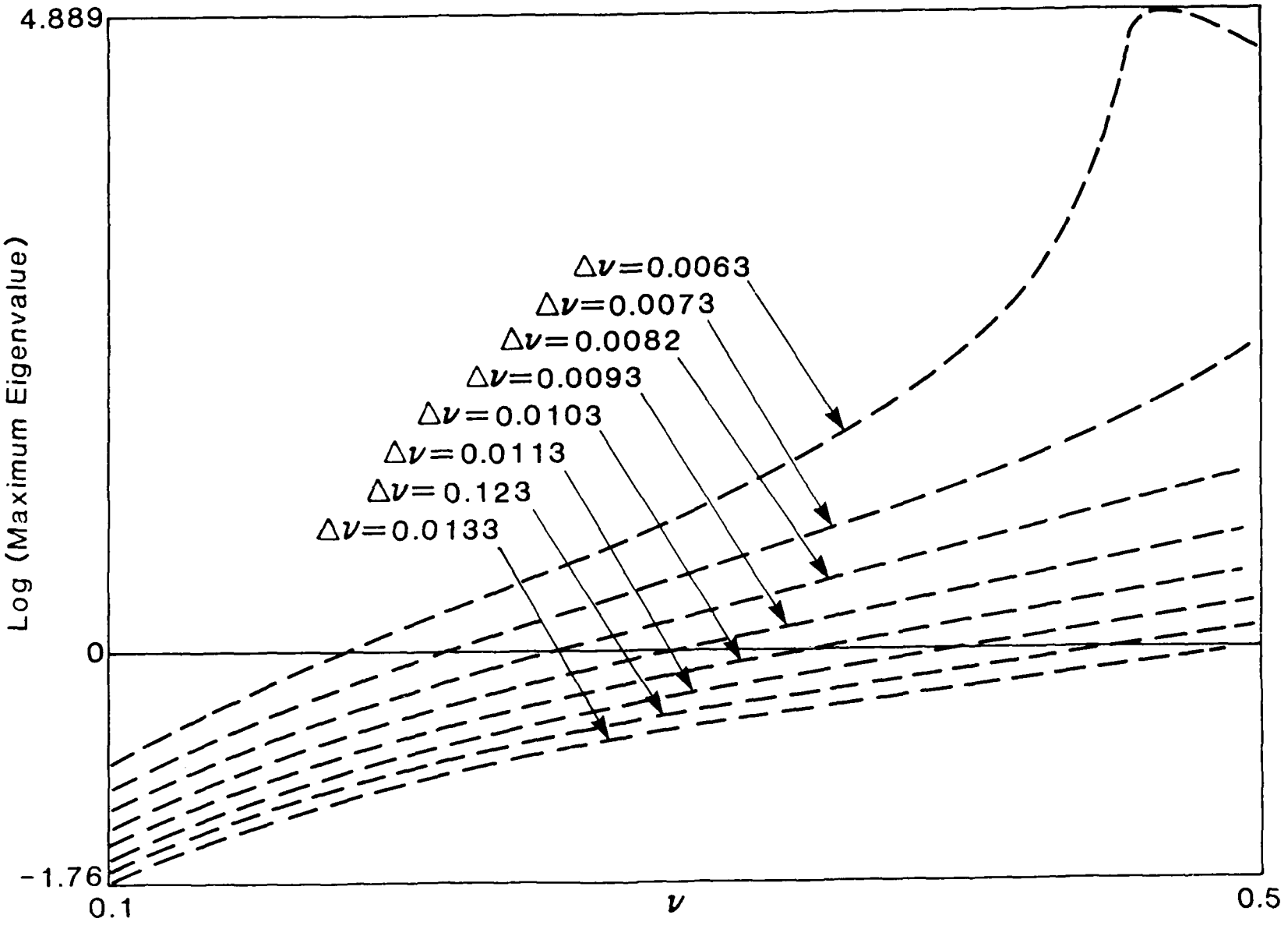

Fig. 2. Maximum eigenvalue evaluated by the Fourier method along the ν axis at $\Delta\mu = 0.004$, $\theta = 1$ for different $\Delta\nu$.

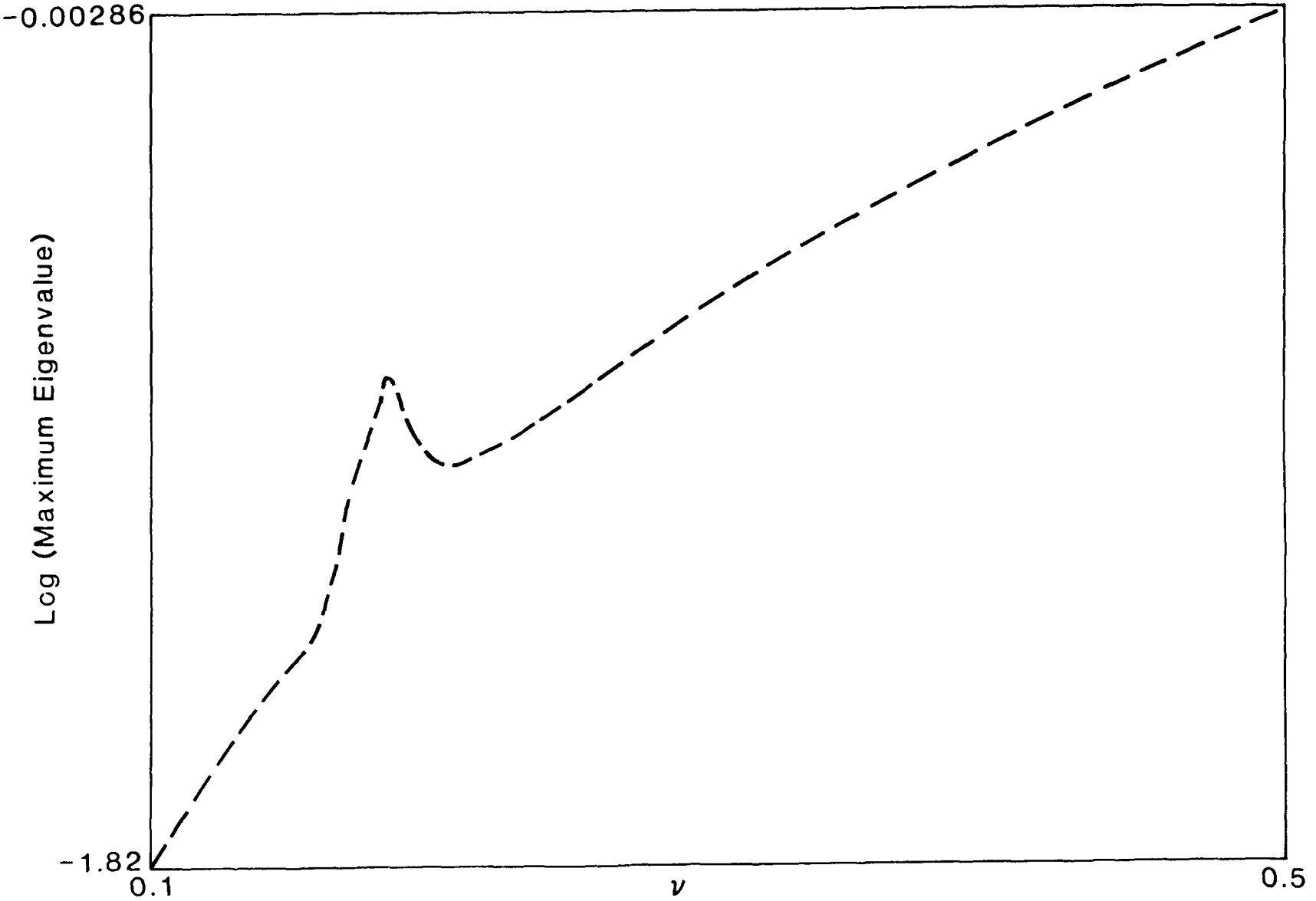

Fig. 3. Maximum eigenvalue evaluated by the Matrix method along the ν axis at $\theta = 1$, $\Delta\mu = 0.004$, $\Delta\nu = 0.01334$.

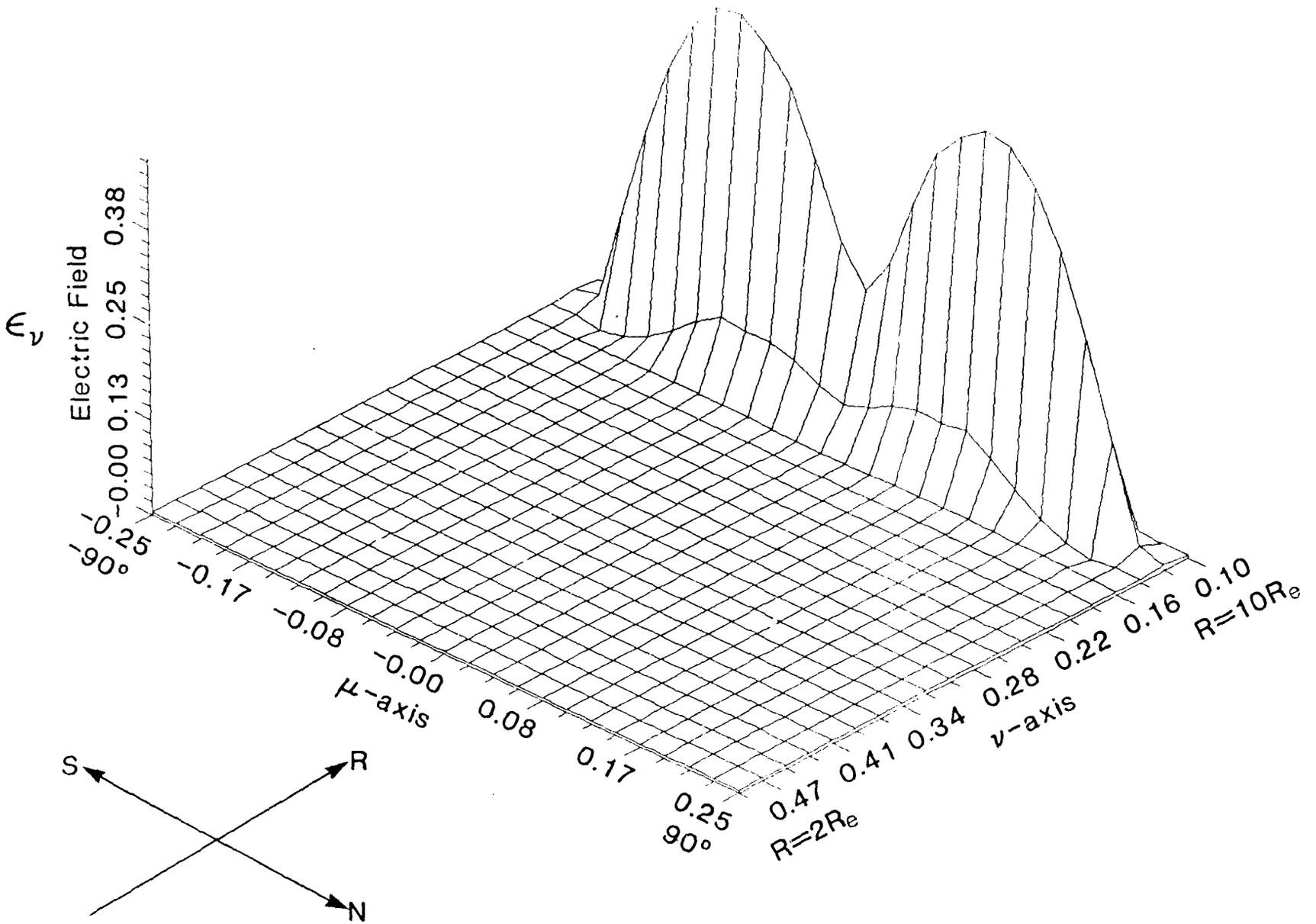

Fig. 5. Normalized electric field of toroidal mode (m = 100).

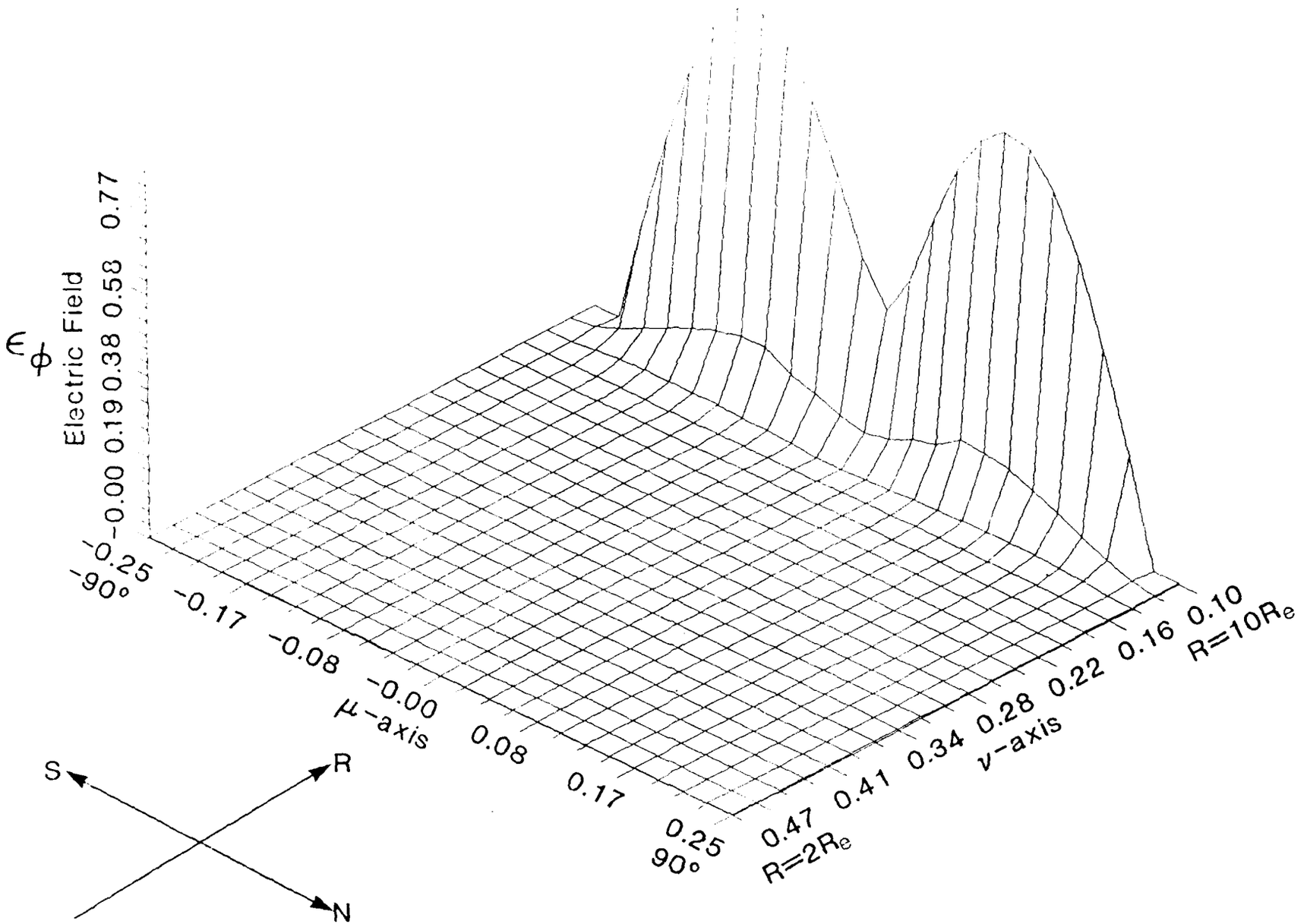

Fig. 4. Normalized electric field of poloidal mode (m = 100).

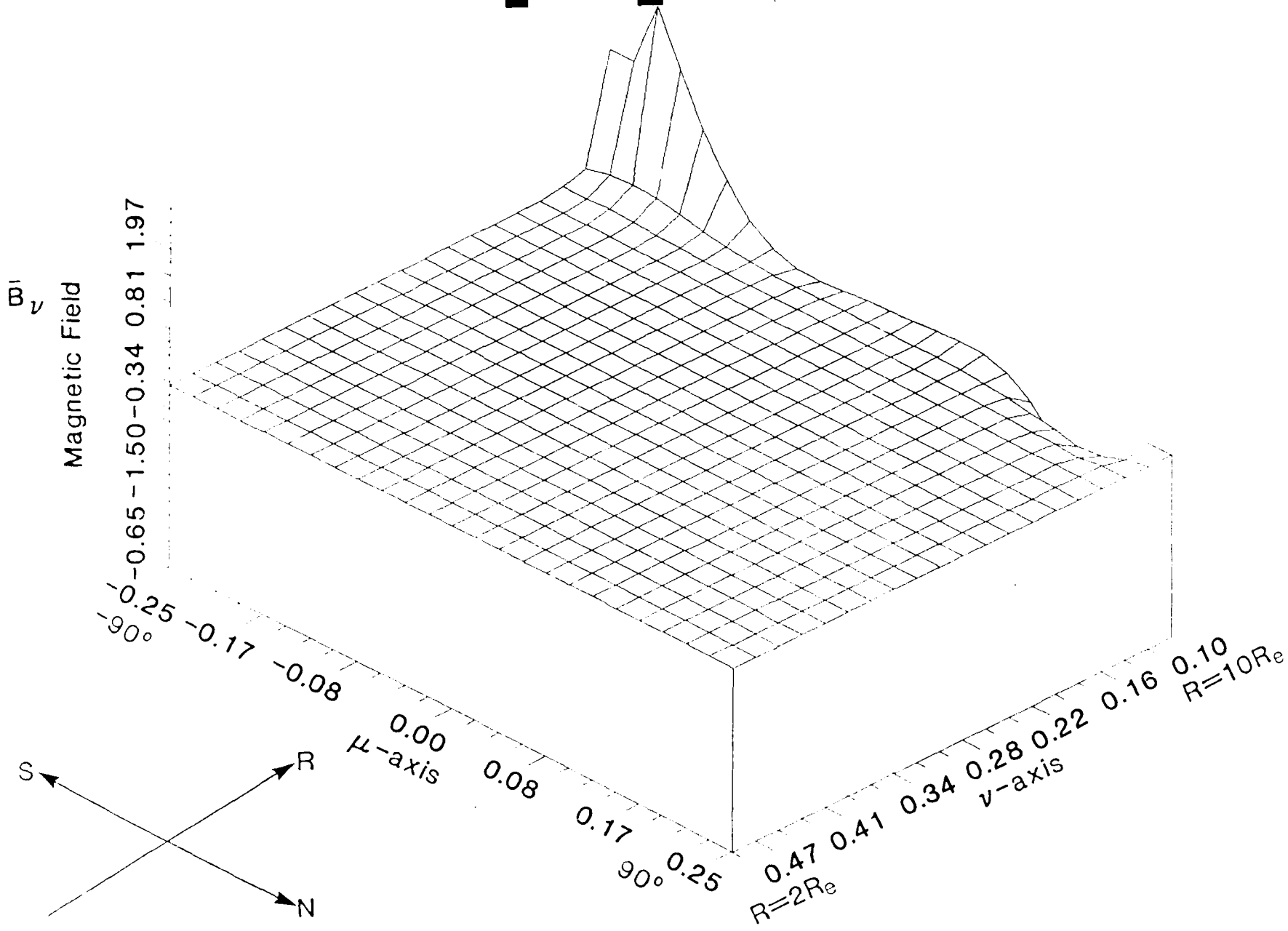

Fig. 6. Normalized magnetic field of poloidal mode (radial component) (m = 100).

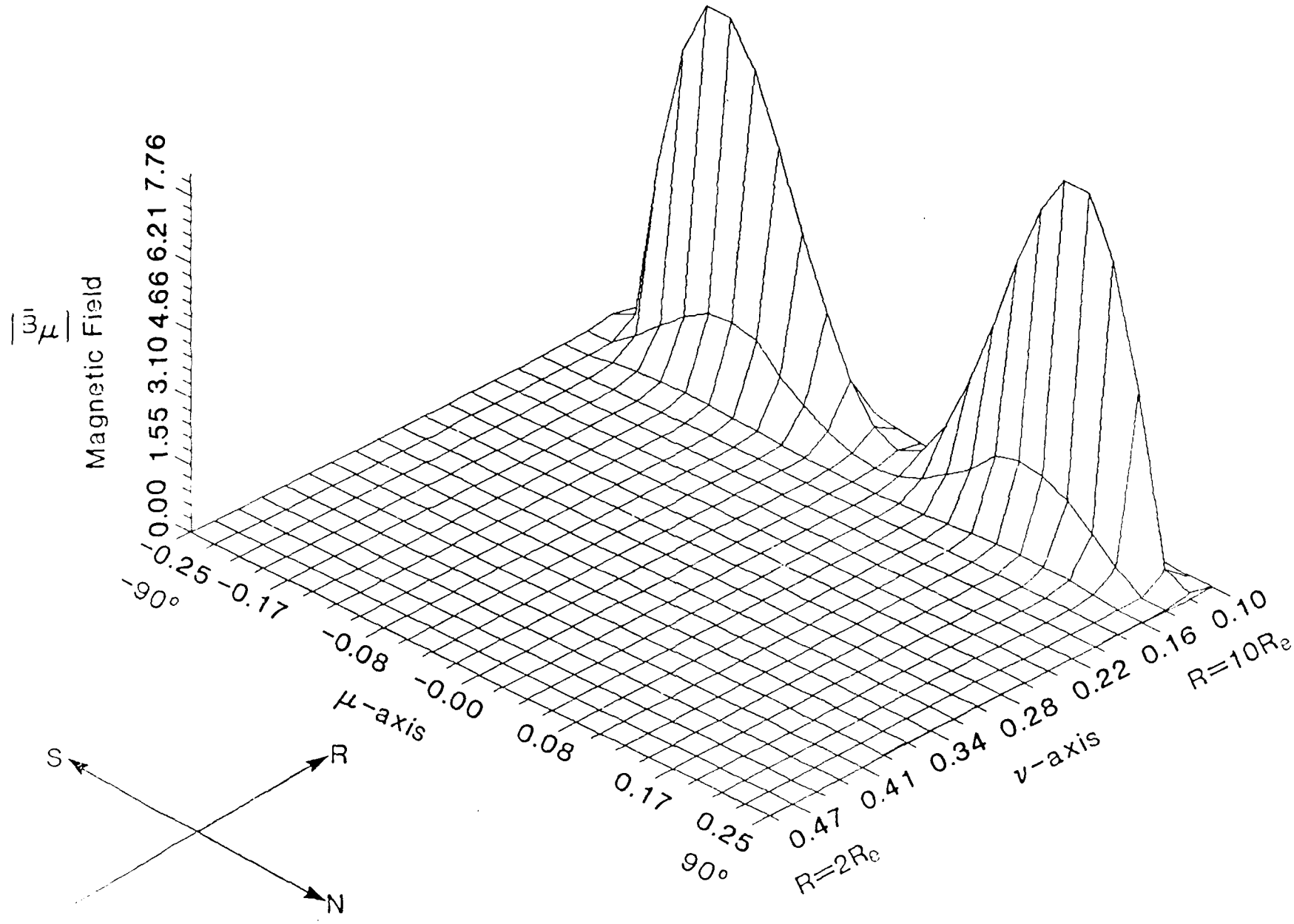

Fig. 7. Normalized magnetic field of toroidal mode (N-S component) (m = 100).

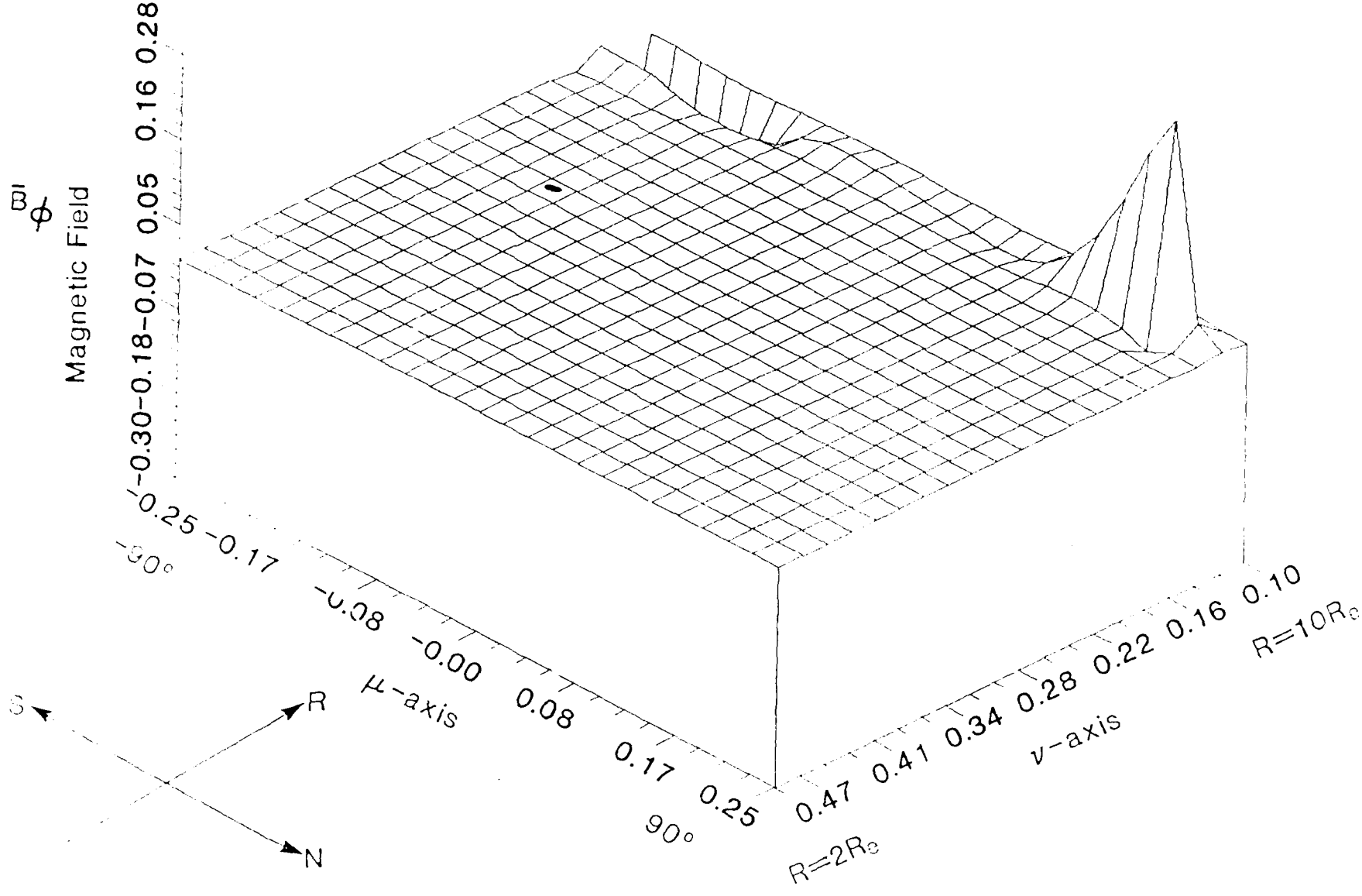

Fig. 8. Normalized magnetic field of toroidal mode (E-W component) (m = 100).

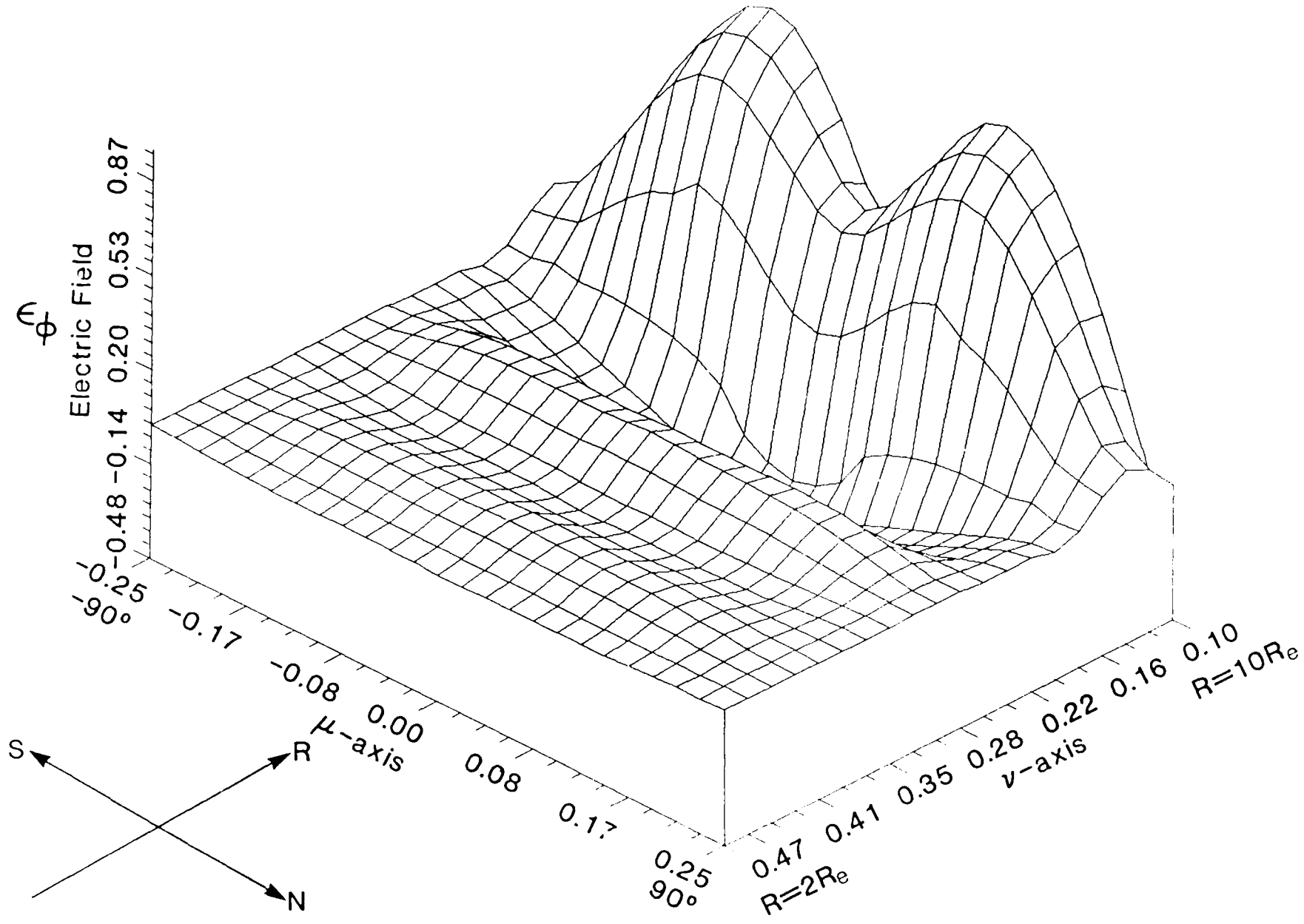

Fig. 9. Normalized electric field of poloidal mode (m = 20).

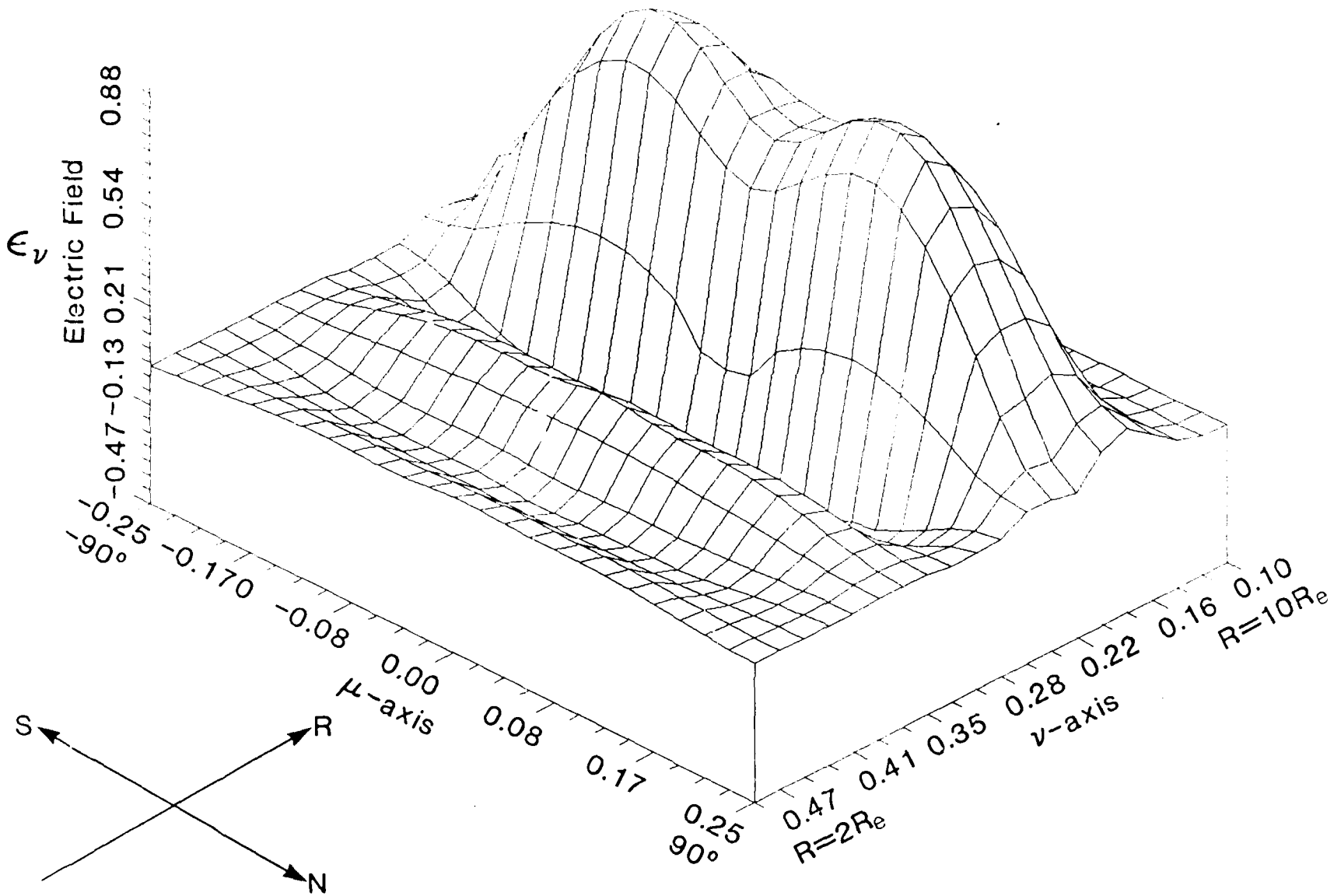

Fig. 10. Normalized electric field of toroidal mode (m = 20).

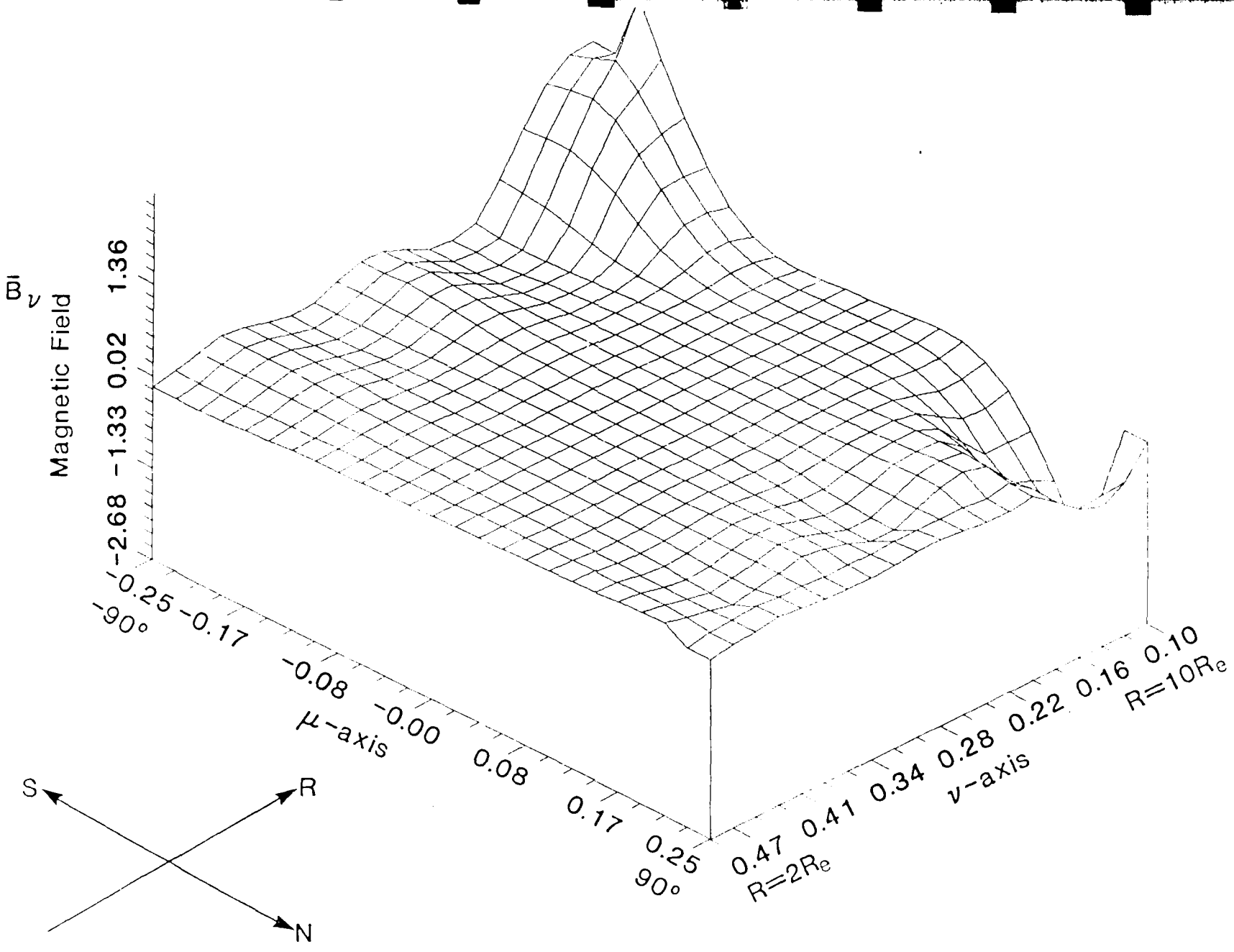

Fig. 11. Normalized magnetic field of poloidal mode (radial component) (m = 20).

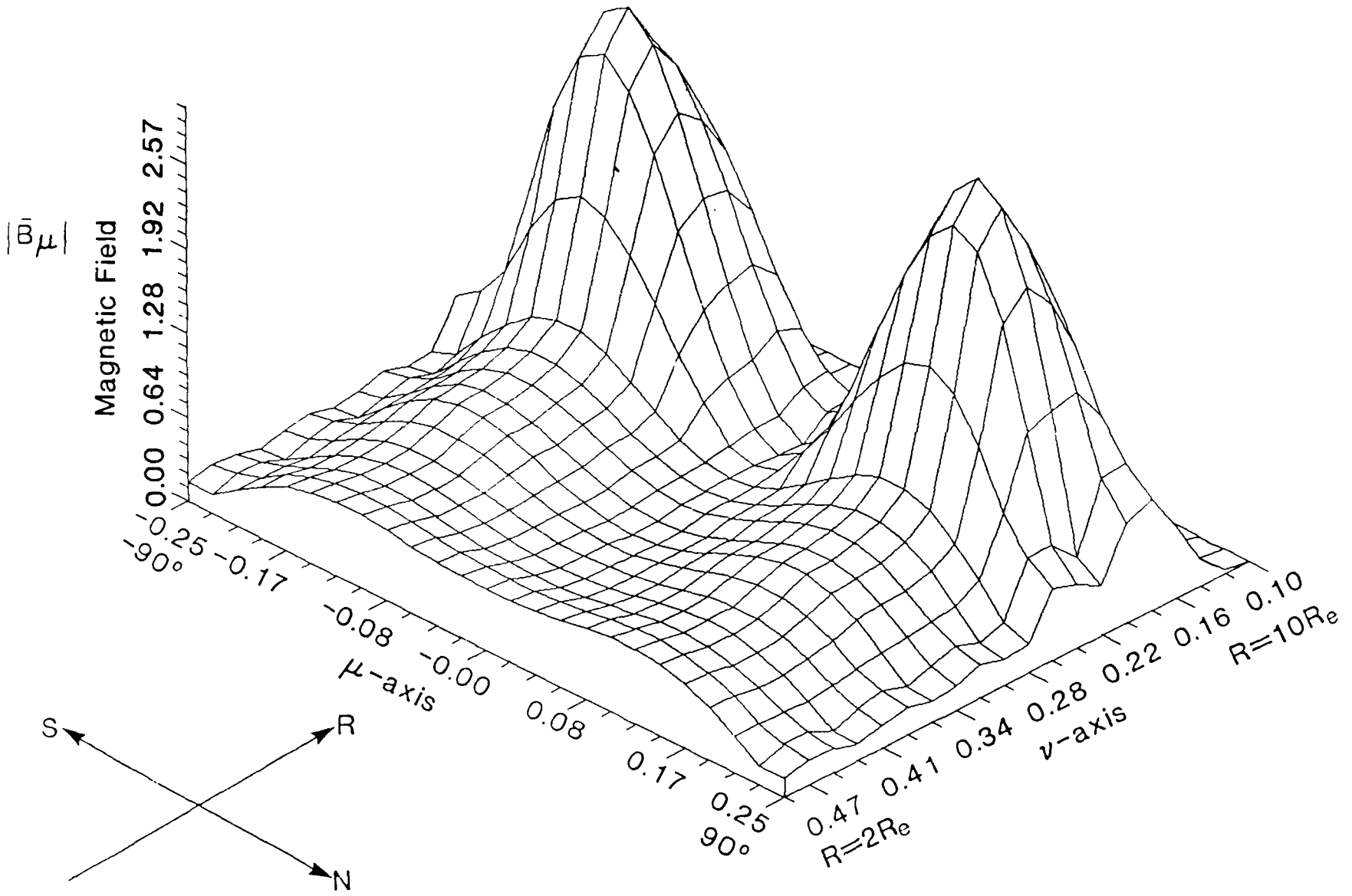

Fig. 12. Normalized magnetic field of toroidal mode (N-S component) (m = 20).

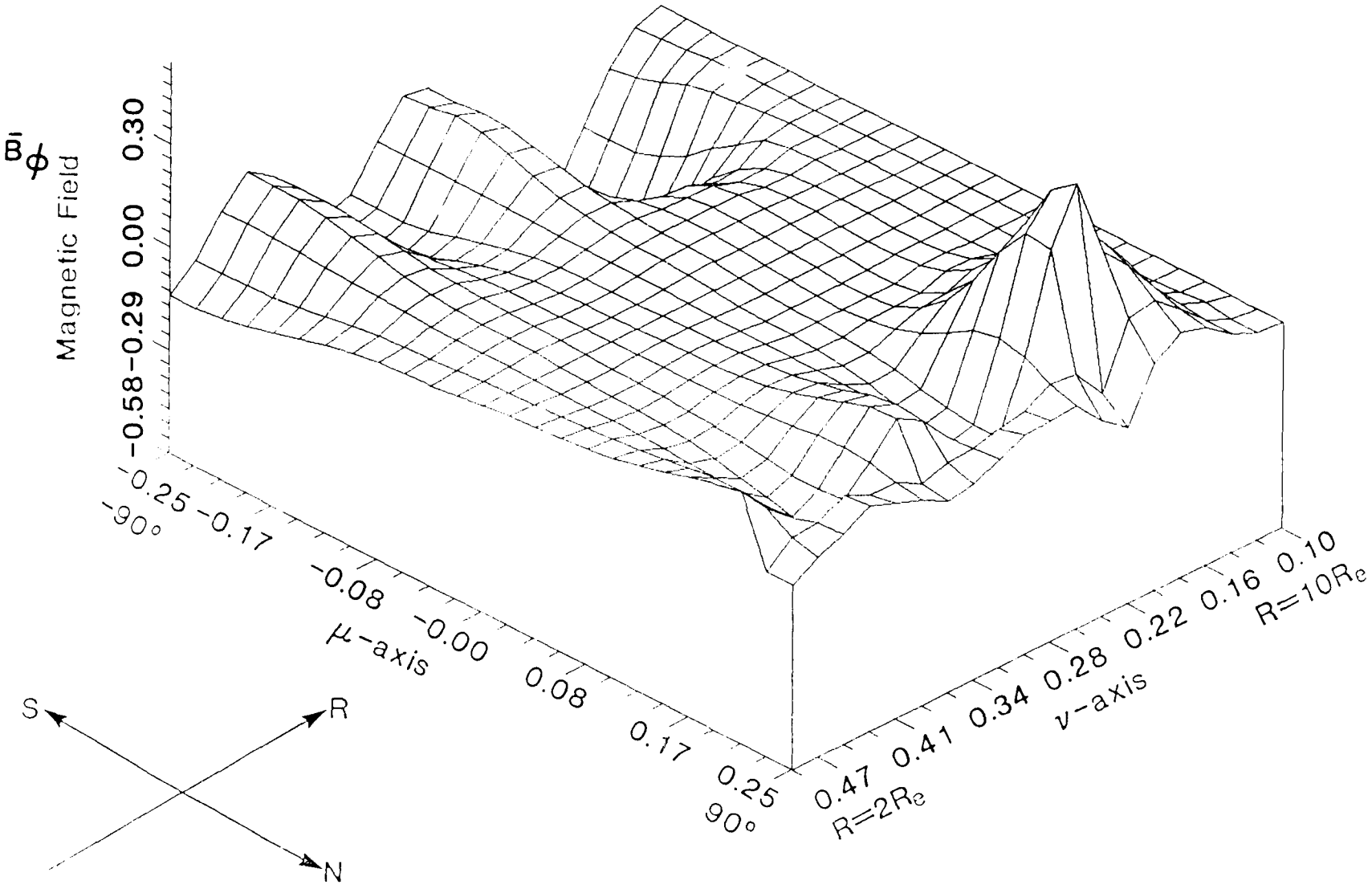

Fig. 13. Normalized magnetic field of toroidal mode (E-W component) (m = 20).

GEOPHYSICAL RESEARCH LETTERS, VOL. 14, NO. 9, PAGES 961-964, SEPTEMBER 1987

A NEW INTERPRETATION OF PLASMA-LINE OVERSHOOT PHENOMENA

S. P. Kuo

Polytechnic University, Farmingdale, N.Y. 11735

M. C. Lee

Massachusetts Institute of Technology, Cambridge, Ma. 02139

F. T. Djuth

Space Sciences Laboratory, The Aerospace Corporation, Los Angeles, Ca. 90009

Abstract. The temporal evolution of Langmuir waves excited by high-power, high-frequency (HF) radio waves in the ionosphere is studied theoretically. This study is motivated by past observations made with the 450 MHz radar at Arecibo Observatory in Puerto Rico. Two kinds of nonlinear damping to the parametric decay instability are considered in the derivation of the rate equation for the spectral intensity of enhanced Langmuir waves. They are Langmuir wave cascading caused by nonlinear Landau damping and cross-field electron diffusion. The first damping process leads to the saturation of individual unstable Langmuir wave. The second process, which results from the incoherent scattering of electron orbits by the total excited Langmuir waves, yields anomalous damping that applies to each Langmuir wave. Consequently, Langmuir waves with smaller growth rates will be suppressed by those with larger growth rates. Such a mode competition process may cause the overshoot of the HF-enhanced plasma line observed with the Arecibo 430 MHz radar. Favorable agreement is obtained between theory and the Arecibo observations.

Introduction

The HF-enhanced plasma lines observed in the Arecibo heating experiments have been generally attributed to the parametric decay instability, whereby the plasma waves and heavily damped ion-acoustic wave are parametrically excited by the injected HF heater waves [e.g. Fejer and Kuo, 1973; Perkins, et al., 1974]. The excited plasma waves then enhance the backscatter spectrum of the Arecibo 430 MHz radar at frequencies near 430 MHz $\pm f_{HF}$ where f_{HF}, is the frequency of the HF heater wave. The radar returns at these two sidebands are often referred to as HF-enhanced plasma lines ($HFPL_s$). One of the most reproducible phenomena associated with the HF-enhanced plasma lines in the F region over Arecibo is the so called main plasma line overshoot [Showen and Kim, 1978; Showen and Behnke, 1978]. A clear demonstration of the overshoot phenomenon is presented in the Figure 2 of Showen and Behnke. However, the growth and decay periods of the overshoot presented in that Figure are rather long in comparison with the recent observations at Arecibo. It is shown in the recent study of temporal evolution of $HFPL_s$ that the HFPL signal exhibited an initial growth lasting for a few tens of milliseconds before reaching a maximum value, and then greatly reduced its strength in the order of a second. The typical time scales for the overshoot process of $HFPL_s$ at Arecibo are summarized in Table I. These values are based upon the recent data presented by Duncan and Sheerin [1985] and Djuth et al. [1986], and the other unpublished data. Based upon the experimental observation of Coster et al., [1985] at Arecibo, it seems unlikely that the anomalous absorption by HF-induced short-scale (1-10m) irregularities can account for this overshoot phenomenon. In addition, recent efforts made at Arecibo to carefully measure the differential absorption of the ionospherically reflected HF wave have found an upper bound for the anomalous absorption of the HF waves by the induced short-scale irregularities that is no more than 10% power at the heater frequency of 5.1 MHz [J.A. Fejer, F.T. Djuth, and M.P. Sulzer, private communications, 1986]. Given the fact that strong plasma line overshoot was present during the absorption measurements, this data supports the idea that anomalous absorption does not play a key role in the plasma-line overshoot phenomenon.

In the present work we propose a mechanism that is based on the mode suppression process introduced by the resonance broadening effect to account for the plasma-line overshoot phenomenon. It is expected that the presence of the parametric decay instabilities gives rise to perturbations on the phase space orbits of electrons (charged particles in general). The result of the incoherent scattering of electron orbits by the total excited plasma waves can lead to electron diffusion in the velocity space along the magnetic field together with the cross-field diffusion in the coordinate space. On one hand, these diffusion processes appear as an enhanced viscosity to the electron motion. But, on the other hand, they broaden the resonance interaction between the electrons and waves. It has been suggested that the resonance broadening effect can contribute to the saturation of the parametric instability [Weinstock and Bezzerides, 1973] mainly through the velocity diffusion process, and further lead to the mode suppression [Dupree, 1968; Dum and Dupree, 1970] effectively through the cross-field spatial diffusion process. The mode suppression process can be understood from the fact that the anomalous damping introduced by resonance broadening effect to each unstable plasma line is proportional to the total spectral intensity of the excited plasma waves. In other words, the enhanced electron diffusion is determined by the total spectral intensity. The increase of the anomalous damping on the slowly

Paper number 7L6591.
0094-8276/87/007L-6591/$03.00

TABLE I. The Arecibo 430 MHz HF-Enhanced Plasma Line (HFPL) in the F Region

	Range of Values	Typical Value
Total HFPL Growth Period	2-50 ms	20 ms
Overshoot Time Scale	0.1 - 10.0 s	1 s
HFPL Overshoot Ratio	10 - 100	50

growing plasma line can result from the fast growth of other lines in the same region. It will be shown later that the linear growth rate of each plasma line depends on the wave propagation angle θ, (the geomagnetic field) and the wavenumber k of the plasma line. Consequently, the spectral lines having smaller growth rates will be suppressed when their linear growth rates are exceeded by the anomalous damping introduced by the modes with larger growth rates. A physical model based on the aforesaid process will be presented in the subsequent sections to interpret the plasma-line overshoot phenomenon.

Theoretical Model

We consider the parametric decay instability near the reflection height of the HF heater wave in the ionospheric F-region. If an HF heater wave with the ordinary polarization is transmitted, the wave electric field $\vec{E}_p = \hat{z}E_p$ can be assumed to be parallel to the geomagnetic field $\vec{B}_o = \hat{z}B_o$ in the region near its reflection height. Electron plasma waves and ion acoustic waves are then excited parametrically by the imposed pump wave as the pump field intensity exceeds the threshold of the instability. The linear dispersion relation of this instability for a dipole pump wave $E_p = E_o e^{-i\omega_o t} + c.c.$ is given by [Nishikawa, 1968; Kuo and Cheo, 1978],

$$4\omega_s\omega_Q(\gamma+\nu_Q/2)\,(\gamma+\nu_i/2) = k_z^2(e^2E_o^2/m_em_i) \quad (1)$$

where ω_s and ω_Q represent the frequencies of the ion acoustic mode and electron plasma mode, respectively; the frequency matching condition $\omega_s+\omega_Q=\omega_o$ is satisfied; γ is the linear growth rate, ν_Q is the electron-ion collision frequency; $\nu_i = (\pi/2)^{1/2}\omega_s\,(T_e/T_i)^{3/2}e^{-T_e/2T_i-3/2}$ represents the ion Landau damping rate, and $k_z = k\cos\theta$ for the excited spectral line with $\vec{k}$ and a propagation angle θ with respect to the earth magnetic field.

The linear growth rate $\gamma^L_{k\theta}$ of the spectral line $\vec{k}$ is then found to be

$$\gamma^L_{k\theta} \cong -\frac{1}{4}(\nu_Q+\nu_i) + [eE_o/2(m_em_i\omega_o\omega_s)^{1/2}]$$

$$\cos\theta = \alpha k^{1/2}\cos\theta - \beta_o - \beta_i k \quad (2)$$

where $\alpha = eE_o/2(m_em_i\omega_oc_s)^{1/2}$, $\beta_o = \nu_Q/4$, $\beta_i = \frac{1}{4}(\pi/2)^{1/2}c_s\,(T_e/T_i)^{3/2}e^{-T_e/2T_i-3/2}$, $\omega_s = kc_s$ and $\omega_Q \approx \omega_o$ have been used, and the maximum linear growth rate is given by $\gamma^L_{k\theta\,max} = (\alpha^2/4\beta_i)\cos^2\theta - \beta_o$ for $k = k_o = \alpha^2\cos^2\theta/4\beta_i^2$. It is seen that the linear growth rate of the spectral line is a function of the propagation angle θ and the wave number k and the growth rate is maximized for each k at $\theta = 0$. However, the instability can also be excited at a large propagation angle if the pump wave is intense enough. For a pump field exceeding the threshold field, the maximum angle for the unstable $|\vec{k}|$ modes is given by

$$\theta_{ok} = \cos^{-1}[(\beta_o+\beta_i k)/\alpha k^{1/2}] \quad (3)$$

where $\beta_o+\beta_i\,k \le \alpha k^{1/2}$ is required for the instability.

We now consider two possible nonlinear damping mechanisms of the instability. One is due to the cascading of the plasma lines and the other one is the cross-field diffusion damping caused by the resonance broadening effect. The cascading process occurs when the amplitude of the excited plasma line exceeds the threshold of parametric decay process. The daughter plasma line then takes energy away from the mother plasma line and thus slows down the growth of the mother plasma line. If this decay process does not drain much energy from the mother plasma line, cascading process will proceed further to excite more decay lines until the total energy drained by the decay lines is large enough to stop the growth of the mother line. Based on the energy balance relation, the anomalous damping rate $\nu^*_{k\theta}$ introduced by the cascading process on the original decay instability is approximately equal to the collisionless linear growth rate of the daughter decay mode having the mother decay mode as the pump. It is

$$\nu^*_{k\theta} \cong \sqrt{k}\,eE_{k\theta}/2(m_em_i\omega_oc_s)^{1/2} \quad (4)$$

where $E_{k\theta}$ is the field amplitude of the mother decay plasma line propagating at the angle θ and having the wavenumber k.

In addition to the cascading process that can only lead to the saturation of the instability, a second non-linear effect which originates in the broadening of wave-electron resonances by the random motion of electrons in the excited turbulent field is also considered in the study of the HFPL overshoot phenomenon. Secular changes of the guiding center positions, cyclotron radii, and phase angles of electrons by the turbulent field give rise to resonance broadening and cross-field diffusion similar to those produced by collisional scattering. It has been shown by Dum and Dupree [1970] that the field-dependent broadening can be expressed in terms of diffusion coefficients which broaden the resonance function in a similar way as the collisional damping does. Consequently, an anomalous damping to the instability is also introduced by the resonance broadening process. In the magnetized plasma, the cross-field diffusion will be the major response of electrons to the incoherent scattering by waves. The diffusion damping rate to the $\vec{k}$ line is thus obtained as

$$d_\theta(k) = k_\perp\cdot\underline{D}_\perp\cdot k_\perp \quad (5)$$

where $\underline{D} = \sum_{\vec{k}'}[c^2(\hat{z}\times\vec{E}_{k'})\,(\hat{z}\times\vec{E}_{k'})/B_o^2]\,\frac{2\gamma_{k'o}}{(\omega_o^2+\gamma_{k'o}^2)}$,

$\gamma_{k'o} = \sqrt{k'}\alpha\cos\theta'$, and $\Omega_e^2 << \omega_o^2$ is assumed. Replacing the summation by integral, we can rewrite (5) as

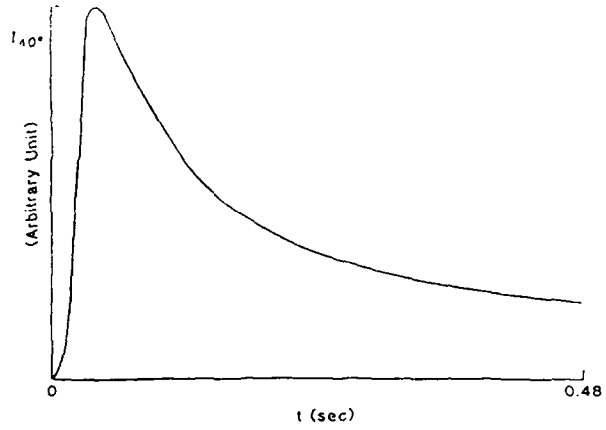

Fig. 1. Temporal evolution of the spectral intensity of the 40° plasma lines; the parameters $2E_o = 0.5$v/m, $\nu_e = 400$/sec, $f_o = 5$MHz and $C_s = 3.5\times10^3$ m/sec are used.

$$d_\theta(k) = [\alpha c^2 k^2 \sin^2\theta / B_o^2 \omega_o^2] \int\int 2\pi k'^2 \sqrt{k'} \sin^3\theta' \cos\theta' E^2_{k'\theta'} dk' d\theta'. \quad (6)$$

From (2), (4) and (6), the nonlinear growth rate of the k line can be defined by

$$\gamma_{k\theta} = \gamma^L_{k\theta} - \nu^*_{k\theta} - d_\theta(k). \quad (7)$$

The rate equation for describing the nonlinear evolution of $E_{k\theta}$ is then given by

$$\frac{d}{dt} E_{k\theta} = \gamma_{k\theta} E_{k\theta} \quad (8)$$

Analysis

To simplify the analysis, we only analyze the evolution of the total spectral intensity I_θ of plasma lines propagating at the same angle θ with respect to the geomagnetic field, where $I_\theta = 4\pi \sin\theta \int dk\, k^2 E^2_{k\theta}$ is so defined. In terms of I_θ, Equation (8) becomes approximately

$$\frac{d}{dt} I_\theta \cong \left[\bar{\alpha}_\theta \cos\theta - \bar{\beta}_\theta - 2\bar{d}_\theta - \bar{\eta}_\theta I_\theta^{1/2}\right] I_\theta \quad (9)$$

where $\bar{\alpha}_\theta = 2\alpha\sqrt{k_o}$, $\bar{\beta}_\theta = 2(\beta_o + \beta_1 k_0)$, $\bar{\eta}_\theta = e/k_0^{1/2}(4\pi \sin\theta m_e m_i \omega_o c_s)^{1/2}$, and

$$\bar{d}_\theta = \left[\alpha c^2 k_o^{5/2} \sin^2\theta / 2B_o^2\omega_o^2\right] \int_o^{\theta_o(t)} I_{\theta'} \sin^2\theta' \cos\theta' d\theta';$$

$$k_o = \alpha^2 \cos^2\theta / 4\beta_1^2. \quad (10)$$

we perform the average in k by assuming the $E^2_{k\theta}$ is peaked initially at k_o with maximum linear growth rate; θ_o is the maximum averaged spectral angle and defined by

$$\bar{\alpha}_{\theta_o} \cos\theta_o - \bar{\beta}_{\theta_o} - 2\bar{d}_{\theta_o} = 0 \quad (11)$$

With the aid of (9) and (10), taking the time derivative of (11) leads to

$$\frac{d}{dt}\theta_o = -\{b\sin^3\theta_o\cos^4\theta_o/[\bar{\alpha}\sin^2\theta_o + bI_{\theta_o}\sin^5\theta_o\cos^5\theta_o + (2 - 5\sin^2\theta_o/\cos^2\theta_o)(\bar{\alpha}_{\theta_o}\cos\theta_o - \bar{\beta}_{\theta_o})]\} \int_o^{\theta_o(t)} [\bar{\alpha}_\theta\cos\theta - \bar{\beta}_\theta - 2\bar{d}_\theta - \bar{\eta}_\theta I_\theta^{1/2}] I_\theta \sin^2\theta\cos\theta\, d\theta \quad (12)$$

where $b = \alpha^6 c^2/32\beta_1^5 B_o^2 \omega_o^2$ and $\bar{\alpha} = \alpha^2/\beta_1$.

So far we have derived two coupled equations (9) and (12) for the temporal evolution of the spectral intensity of HFPL$_s$ oriented at the angle θ. They have been solved numerically. For describing the overshoot phenomenon observed in the Arecibo heating experiments, we let $\theta = 40°$ and the numerical results of (9) and (12) are presented in Figures 1 and 2, which show the functional dependence of I_{40}· and $\theta_o(t)$ on time t, respectively. As shown in Figure 1, the spectral intensity I_{40}· grows initially at the linear growth rate, it overshoots for very high level to form a peak and then decreases at a much slower rate subsequently. It eventually saturates at a much lower level than its peak value. An overshoot phenomenon has been clearly demonstrated by the proposed theory.

Summary

A theoretical model for the temporal evolution of the HF-enhanced plasma line (HFPL) is developed. We suggest that mode suppression caused by the resonance broadening effect may be the physical process responsible for the overshoot of HFPL detected by the Arecibo 430 MHz radar. In other words, the presence of other decay lines having larger growth rates, which cannot be detected by the Arecibo radar, gives rise to enhanced viscosity to electron motion and, thus, increases the threshold for exciting the detected plasma line. We also include the nonlinear effect introduced by the cascading process in the formulation theory. This effect results in the saturation of the parametric decay instability, and hence, is responsible for the steady state level of the HFPL after the overshoot process.

The difference between the linear growth rate of the parametric decay instability and the anomalous damping introduced the aforementioned two processes defines the nonlinear growth rate of the

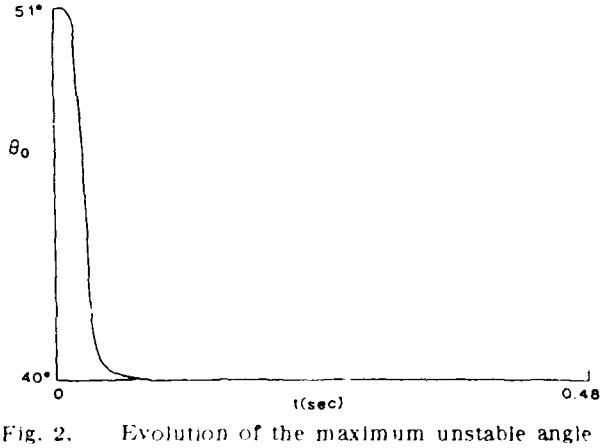

Fig. 2. Evolution of the maximum unstable angle in time.

HFPL. It is then used for establishing the nonlinear growth rate equation (8) of the HFPL, from which the rate equation (9) for the total spectral intensity I_θ of plasma lines propagating at the same angle θ is derived. Although Equation (9) does not provide the exact amount of the temporal development of HFPL, it greatly simplifies the analysis of the problem and maintains the important features of the phenomenon as illustrated in Figure 1. A second rate equation (12) for the averaged maximum spectral angle θ_0 is also obtained for studying the temporal evolution of the HFPL self-consistently. The numerical results of (9) and (12) for $\theta = 40^\circ$ have clearly demonstrated the overshoot phenomenon similar to that observed by Showen and Behnke [1978] in the Arecibo ionospheric heating experiments. However, regarding the overshoot time scales, our calculated values are more consistent with the typical results of recent observations at Arecibo as shown by Table I.

Acknowledgements. This work is supported jointly by the Air Force Office of Scientific Research under Grant No. AFOSR-85-0133, AFOSR-85-0316 and the National Science Foundation under Grant No. ATM-8315322 at the Polytechnic University, and by the NASA under Grant No. NAG5-270 and P.O. S-56148D at the Massachusetts Institute of Technology, and by the Aerospace-sponsored Research Program.

References

Coster, A.J., Djuth,F.T., Jost, R.J. and Gordon, W.E., The Temporal Evolution of 3-M Striations in the Modified Ionosphere, J. Geophys Res., 90, 2807, 1985.

Djuth, F.T. Gonzales, C.A., and Ierkic, H.M., Temporal Evolution of HF-Enhanced Plasma Line in the Arecibo F Region, J. Geophys Res., 91, 12089, 1986.

Dum, C.T., and Dupree, T.H., Nonlinear Stabilization of High Frequence Instabilities in a Magnetic Field, Phys. Fluids., 13, 2064, 1970.

Duncan, L.M. and Sheerin, J.P., High-Resolution Studies of the HF Ionosphere Modification Interaction Region, J. Geophys. Res., 90, 8371, 1985.

Dupree, T.H., A Perturbation Theory for Strong Plasma Turbulence and Nonlinear Theory of Low Frequency Instabilities", Phys. Fluids, 9, 773, 1966; and 11, 2680, 1968.

Fejer, J.A. and Kuo, Y.Y. Structure in the Nonlinear Saturation Spectrum of Parametric Instabilities, Phys. Fluids, 16, 1480 1973.

Kuo, S.P. and Cheo, B.R., Parametric Excitation of Coupled Plasma Waves, Phys. Fluids., 21, 1753, 1978.

Nishkiawa, K., Parametric Excitation of Coupled Waves I & II, J. Phys. Soc. Jpn., 24, 916 and 1152, 1968.

Perkins, F.W., Oberman, C., and Valeo, E.J., Parametric Instabilities and Ionospheric Modification, J. Geophys. Res., 79, 1678, 1974.

Showen, R.L., and Behnke, R.A., The Effect of HF-Induced Plasma Instabilities on Ionospheric Electron Temperatures, J. Geophys. Res., 83, 207, 1978

Showen, R.L., and Kin, D.M., Time Variations of HF-Enhanced Plasma Waves, J. Geophys. Res., 83, 623, 1978.

Weinstock, J. and Bezzerides, B., Nonlinear Saturation of Parametric Instabilities: Spectrum of Turbulence and Enhanced Collision Frequency, Phys. Fluids, 16, 2287, 1973.

(Received May 18, 1987;
revised July 9, 1987;
accepted July 22, 1987.)

Radio Science, Volume 20, Number 3, Pages 546–552, May–June 1985

A theoretical model of artificial spread *F* echoes

S. P. Kuo

Polytechnic Institute of New York, Farmingdale

M. C. Lee

Research Laboratory of Electronics, Massachusetts Institute of Technology, Cambridge

Steven C. Kuo

Polytechnic Institute of New York, Farmingdale

(Received August 7, 1984; revised December 13, 1984; accepted December 20, 1984.)

Four invariants of the ray trajectory are found for a ray propagating in a horizontally stratified ionosphere under the density perturbation of HF wave-induced field-aligned irregularities. The reflection height of the ray can then be determined with the aid of those invariants. The results show that the reflection height of the ray varies drastically (namely, strong spread *F* echoes) in the presence of irregularities that polarize in the magnetic meridian plane. By contrast, the reflection height is not affected (namely, no spread *F* echoes) by those irregularities that polarize in the direction perpendicular to the meridian plane. Spread *F* is quite insensitive to the magnetic dip angle θ_0 in the region from 20° to 70°. The dependence of spread *F* on the scale length of the irregularity has also been examined for the case $\theta_0 = 50°$. It is found that spread *F* is not caused by irregularity with scale length less than about 100 m.

1. INTRODUCTION

Spread *F* that refers to diffuse echoes on an ionogram from the ionospheric *F* region was observed in the ionospheric heating experiments conducted at Boulder, Colorado [*Utlaut*, 1971]. This ionospheric phenomenon is generally believed to be caused by the excitation of large-scale (a few hundreds of meters to kilometers) field-aligned ionospheric irregularities. However, spread *F* is a rare phenomenon in the experiments at Arecibo, Puerto Rico [*Showen and Kim*, 1978] and it has not been observed at Tromsø, Norway since the new European heating facility has been in operation [*Stubbe et al.*, 1982]. Evidences, such as the radio star scintillations [*Frey et al.*, 1984] and the sanning radar incoherent backscatter process [*Duncan and Behnke*, 1978] indicate that large-scale ionospheric irregularities have been excited by HF heater waves at Tromsø and Arecibo. Hence a lack of spread *F* echoes does not imply the absence of heater wave-induced ionospheric irregularities. It may be due to the difference in the polarization directions of the HF wave-induced irregularities where the polarization direction of the irregularity is defined to be the direction of its wave vector. In general, field-aligned irregularities can have two independent polarization directions. One lies in the meridian plane and the other one is in the direction perpendicular to the meridian plane. The theoretical results of filamentation instability in magnetoplasmas [*Kuo and Schmidt*, 1983] also show that the irregularities excited by the *o* mode pump and by the *x* mode pump have different polarization directions. The irregularities excited by the *o* mode pump are field-aligned and are polarized in the direction perpendicular to the meridian plane. By contrast, the irregularities excited by the *x* mode pump are polarized in the meridian plane and are, in general, not field-aligned. However, the field-aligned nature of the irregularities may be established to reduce the diffusion damping along the magnetic field.

Since spread *F* is generally used as an indicator of large-scale irregularities, and yet it is known that sometimes such irregularities do not produce spread *F*. Hence a study leading to better understanding of the spread *F* phenomenon and its relationship with

Paper number 4S1537.
0048-6604/85/004S-1537$08.00

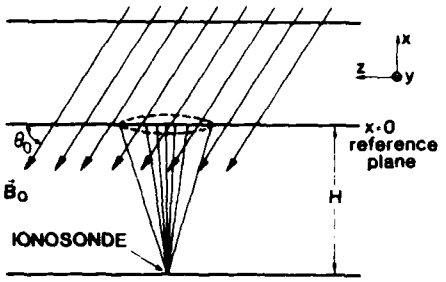

Fig. 1. Coordinates used in the analysis.

density irregularities is thought to be important in this aspect. In the present work a theoretical model for artificial spread F echoes is developed, from which the relationship between the spread F echoes and the HF wave-induced irregularities is studied. The primary purpose of this study is to determine the effects of the irregularity polarizations, scale length, and the magnetic dipangle on the spread F echo. In section 2, the ray trajectory equations are analyzed to study the wave propagation in a horizontally stratified ionosphere under the density perturbation of the HF wave-induced field-aligned irregularities. Four invariants of the ray trajectory are found. Main results are illustrated in the figures. Conclusions are finally drawn in section 3.

2. MODEL AND ANALYSIS

We consider a horizontally stratified ionosphere having a scale length L. Thus the unperturbed electron density is represented by $n_0(x) = n_0(1 + x/L)$, where x is the vertical coordinate and $n_0 = n_0(0)$ is the electron density at the reference plane $x = 0$ located at height H. When field-aligned irregularities are present, the background electron density distribution is perturbed. Thus the total density is the sum of the unperturbed density and the fluctuating densities of the irregularities. In general, field-aligned irregularities can have two independent polarization directions. One lies in the magnetic meridian plane and the other one is in the direction perpendicular to the meridian plane. For those irregularities which are field-aligned in the magnetic meridian plane, the total density perturbation is simply expressed in a form of $\delta n_1 \sin k_1(x \cos \theta_0 + z \sin \theta_0)$, where $2\pi/k_1 = \lambda_1$ is the average scale length of the irregularities, θ_0 is the magnetic dip angle, and z is the horizontal coordinate as shown in Figure 1. The density perturbation associated with the irregularities which are field aligned in the direction perpendicular to the magnetic meridian plane is modeled as $\delta n_2 \sin (k_2 y + \phi)$, where $\lambda_2 = 2\pi/k_2$ is the averaged scale length, y is the coordinate perpendicular to the meridian plane, and ϕ is the arbitrary phase angle. In this model, the total electron density distribution, $n(x)$ is then composed of three components, namely,

$$n(x, z) = n_0(1 + x/L) + \delta n_1 \sin k_1(x \cos \theta_0 + z \sin \theta_0) + \delta n_2 \sin (k_2 y + \phi) \quad (1)$$

For simplicity, the effect of the geomagnetic field on wave propagation will be neglected in the following analyses. The dispersion relation for the wave propagation is thus given by

$$\omega^2 = \omega_{pe}^2 + k^2c^2 \quad (2)$$

where ω and k are the wave frequency and the wave number, respectively, and

$$\omega_{pe}^2 = \omega_{pe0}^2[1 + x/L + (\delta n_1/n_0) \sin k_1(x \cos \theta_0 + z \sin \theta_0) + (\delta n_2/n_0) \sin (k_2 y + \phi)] \quad (3)$$

Since, in reality, the ionosonde antennas radiate radio wave beams with finite cross sections and spread angles, so it is more appropriate to consider the transmitted pulses to be composed of rays whose initial wave vectors and the horizontal locations on the reference plane $x = 0$ are all different. The trajectory of each ray is then governed by the following set of characteristic equations:

$$\frac{d}{dt} x = k_x c^2/\omega \quad (4)$$

$$\frac{d}{dt} y = k_y c^2/\omega \quad (5)$$

$$\frac{d}{dt} z = k_z c^2/\omega \quad (6)$$

$$\frac{d}{dt} k_x = -(\omega_{pe0}^2/2\omega L)[1 + (\delta n_1/n_0)k_1 L \cos \theta_0) \cdot \cos k_1(x \cos \theta_0 + z \sin \theta_0)] \quad (7)$$

$$\frac{d}{dt} k_y = -(\omega_{pe0}^2/2\omega)(\delta n_2/n_0)k_2 \cos (k_2 y + \phi) \quad (8)$$

$$\frac{d}{dt} k_z = -\tan \theta_0(\omega_{pe0}^2/2\omega L)(\delta n_1/n_0)(k_1 L \cos \theta_0) \cdot \cos k_1(x \cos \theta_0 + z \sin \theta_0) \quad (9)$$

where (5) and (8) form one set of coupled equations, and (4), (6), (7) and (9) form the other set of coupled equations, but these two sets of equations do not couple to each other. However, those coupled equa-

tions can be separated by the invariants of the trajectory derived as follows. We first take the ratio of (5) and (8), which yields

$$\frac{dy}{dk_y} = -\frac{2k_y c^2}{\omega_{pe0}^2(\delta n_2/n_0)k_2 \cos(k_2 y + \phi)} \tag{10}$$

Integrating this equation gives the first invariant of the trajectory

$$(\delta n_2/n_0)\sin(k_2 y + \phi) + k_y^2 c^2/\omega_{pe0}^2 = \text{const in time}$$
$$= (\delta n_2/n_0)\sin(k_2 y_0 + \phi) + k_{y0}^2 c^2/\omega_{pe0}^2 \tag{11}$$

where the subscript 0 represents the initial value.

We next substitute (9) into (7) to yield

$$\frac{d}{dt}(k_x - \cot\theta_0 k_z) = -\omega_{pe0}^2/2\omega L \tag{12}$$

Integrating (12) from the initial height $x = 0$ of the ray to the new height x at time t, leads to the second invariant relation

$$k_x - \cot\theta_0 k_z + (\omega_{pe0}^2/2\omega L)t = \text{const in time}$$
$$= k_{x0} - \cot\theta_0 k_{z0} \tag{13}$$

We now construct an equation by first multiplying (4) and (6) by $\cos\theta_0$ and $\sin\theta_0$ respectively, and then summing them up. The result is

$$\frac{d}{dt}(x\cos\theta_0 + z\sin\theta_0) = (c^2/\omega)(k_x\cos\theta_0 + k_z\sin\theta_0) \tag{14}$$

Two additional invariants will be derived as follows. From the ratio of (14) and (7), we obtain

$$\frac{d(x\cos\theta_0 + z\sin\theta_0)}{dk_x} = -\frac{2c^2 L}{\omega_{pe0}^2} \cdot \frac{k_x\cos\theta_0 + k_z\sin\theta_0}{1 + (\delta n_1/n_0)(k_1 L\cos\theta_0)\cos k_1(x\cos\theta_0 + z\sin\theta_0)} \tag{15}$$

With the aid of (13), (14) and (4), (15) is integrated to obtain the third invariant

$$x + (\tan 2\theta_0/2)z + (\delta n_1/n_0)L(\cos^2\theta_0/\cos 2\theta_0)$$
$$\cdot \sin k_1(x\cos\theta_0 + z\sin\theta_0)$$
$$+ (c^2 L/\omega_{pe0}^2)(k_x^2 + \tan 2\theta_0 k_x k_z)$$
$$= \text{const in time} = (\tan 2\theta_0/2)z_0 + (\delta n_1/n_0)$$
$$\cdot L(\cos^2\theta_0/\cos 2\theta_0)\sin(k_1 z_0\sin\theta_0)$$
$$+ (c^2 L/\omega_{pe0}^2)(k_{x0}^2 + \tan 2\theta_0 k_{x0} k_{z0}) \tag{16}$$

The fourth invariant is obtained from integrating the resultant equation defined by the ratio of (14) and (9). It is

$$(\tan 2\theta_0/2)z + (\delta n_1/n_0)L(\sin^2\theta_0/\cos 2\theta_0)$$
$$\cdot \sin k_1(x\cos\theta_0 + z\sin\theta_0)$$
$$+ (c^2 L/\omega_{pe0}^2)(-k_z^2 + \tan 2\theta_0 k_x k_z)$$
$$= \text{const in time} = (\tan 2\theta_0/2)z_0 + (\delta n_1/n_0)$$
$$\cdot L(\sin^2\theta_0/\cos 2\theta_0)\sin(k_1 z_0\sin\theta_0)$$
$$+ (c^2 L/\omega_{pe0}^2)(-k_{z0}^2 + \tan 2\theta_0 k_{x0} k_{z0}) \tag{17}$$

However, (16) and (17) can be rearranged to reduce to much simpler forms. We first take the difference of (16) and (17) to yield

$$x + (\delta n_1/n_0)L\sin k_1(x\cos\theta_0 + z\sin\theta_0) + (k^2 c^2 L/\omega_{pe0}^2)$$
$$= (\delta n_1/n_0)L\sin(k_1 z_0\sin\theta_0) + k_0^2 c^2 L/\omega_{pe0}^2 \tag{18}$$

where $k_0 = k(0)$. We next multiply (16) by $\sin^2\theta_0$ and (17) by $\cos^2\theta_0$ and then take their difference. The result is

$$x - z\cot\theta_0 + (c^2 L/\omega_{pe0}^2)(k_x - k_z\cot\theta_0)^2$$
$$= -z_0\cot\theta_0 + (c^2 L/\omega_{pe0}^2)(k_{x0} - k_{z0}\cot\theta_0)^2 \tag{19}$$

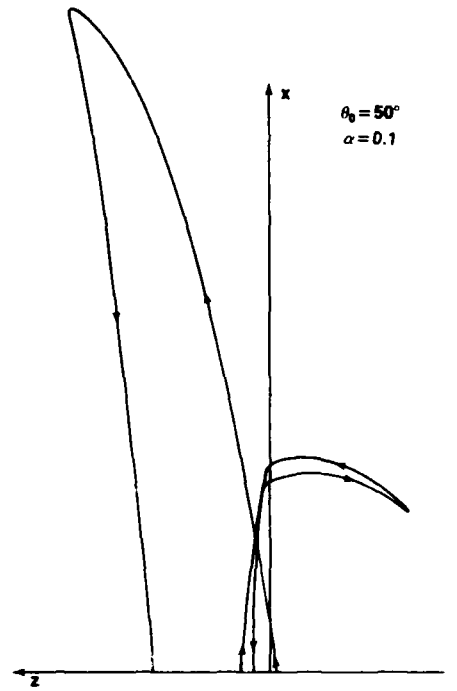

Fig. 2. Example of the appropriate trajectories of the rays detectable to the ionosonde. The parameters used in the calculation are $\theta_0 = 50°$, $L = 50$ km, $\lambda_1 = 1$ km, $k_0^2 c^2/\omega_{pe0}^2 = 1$, and $\alpha = \delta n_1/n_0 = 0.1$.

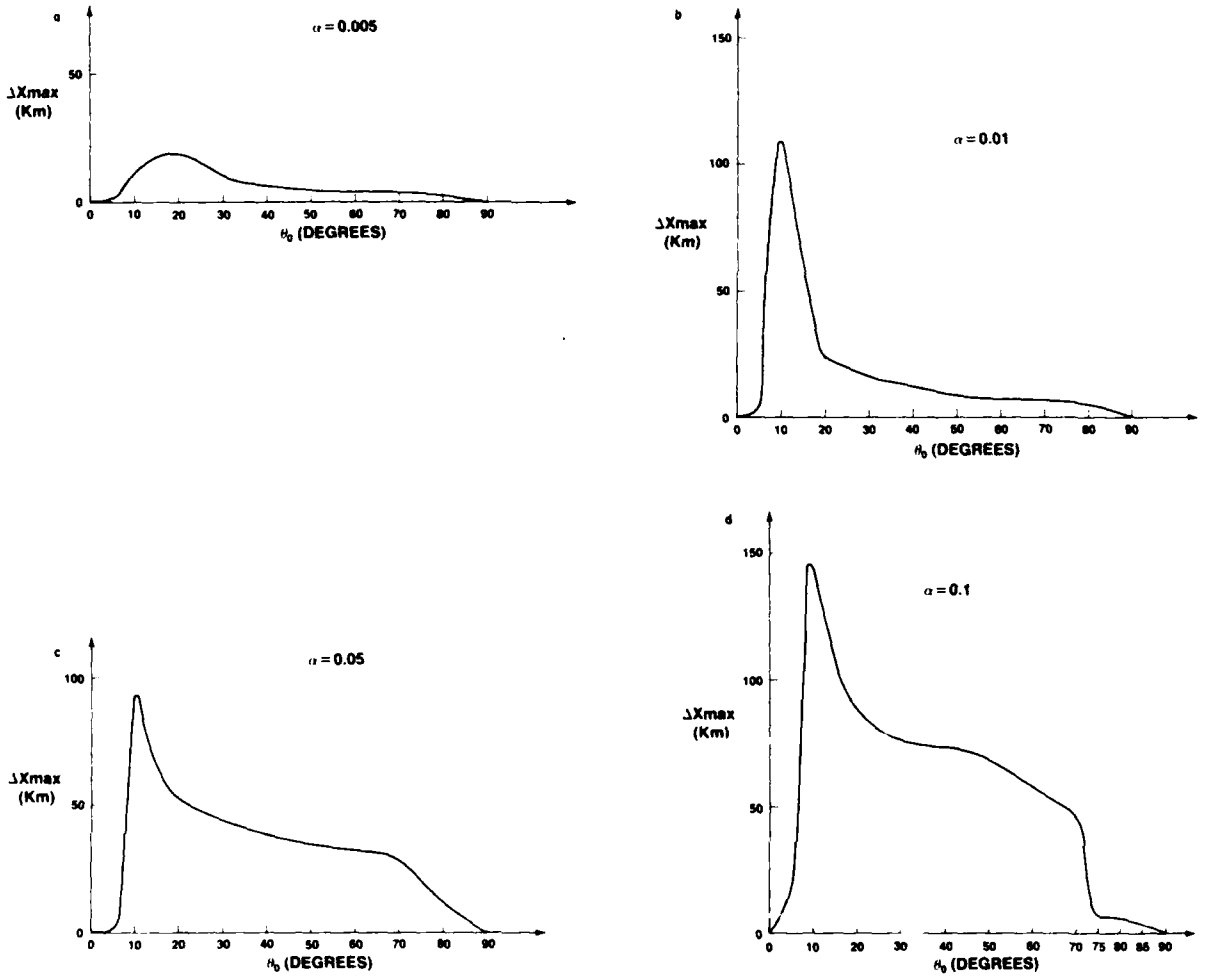

Fig. 3. The functional dependence of the reflection height spread Δx_{max} of a diagnostic beam on the magnetic dip angle θ_0 for $\delta n_1/n_0$ = (*a*) 0.005, (*b*) 0.01, (*c*) 0.05, and (*d*) 0.1.

We have shown that the trajectory of each ray is governed by four invariant relations (11), (13), (18) and (19) that are derived from two sets of coupled differential equations (4)–(9). Hence the temporal evolution of any one of the four variables x, z, k_x and k_z, and either one of the two variables y and k_y, can be determined, with the aid of these invariants, by the corresponding rate equations, namely, equations (4)–(9). The elapsed time for each ray traveling from the reference height to the reflection height can in principle be determined by integrating (7) from $k_x = k_{x0}$ to $k_x = 0$, with the prescribed initial conditions: $x(0) = 0$, $z(0) = z_0$ and $k_z(0) = k_{z0}$. Since the density perturbation δn_2 produced by the irregularities oriented in the direction perpendicular to the magnetic meridian plane does not appear in (7), the reflection height of each ray is thus not expected to be modified by the presence of such oriented irregularities. Physically, it is realized that a ray is reflected (i.e., from upgoing to downgoing) when k_x changed the sign. We thus expect that the reflection height of the ray is likely determined by those parameters which can affect the value of k_x. Apparently, equation (7) shows that δn_2 is not the one among those parameters. This result that k_x is independent of δn_2 is also consistent with the Snells' law in the limit of the absence of the x variation in the plasma density. However, the density perturbation δn_1 produced by the irregularities that are oriented within the meridian plane can affect the reflection height of the ray as seen in (7). One

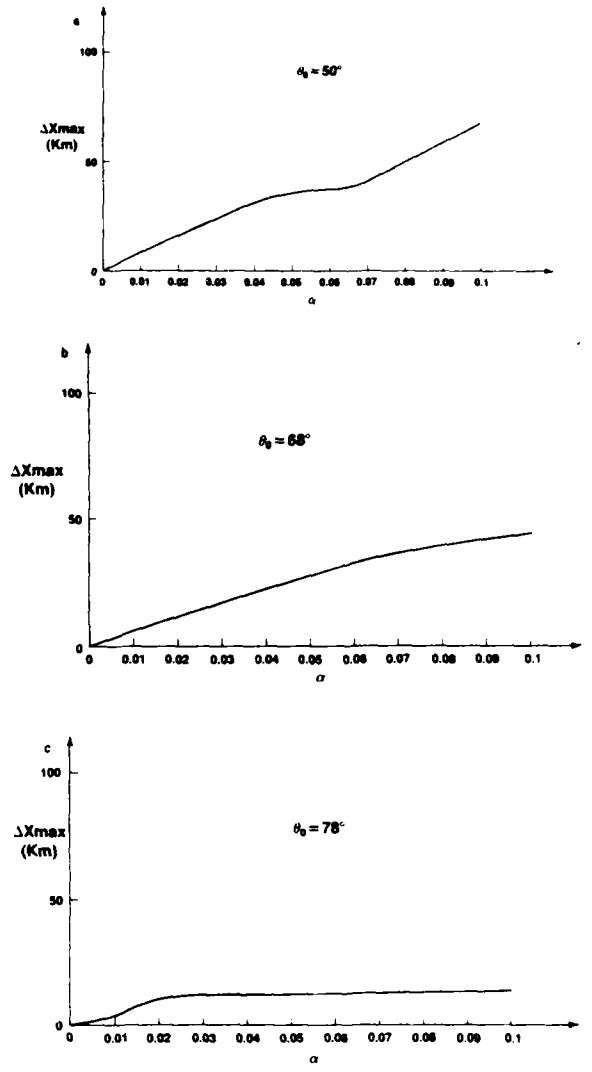

Fig. 4. Δx_{max} versus α for $\theta_0 =$ (a) 50°, (b) 68°, and (c) 78°, where $\alpha = \delta n_1/n_0$.

way to show this effect is to integrate (7) numerically. This equation can be integrated with the aid of the invariant relations (13), (18) and (19). If we assume that each ray of the antenna radiation beam has a straight trajectory from the ionosonde to the reference plane as shown in Figure 1, then the initial conditions for ray trajectory starting from the reference plane can be defined as $x = x_0$, $k_{x0} = k_0 H/(H^2 + z_0^2)^{1/2}$, and $k_{z0} = k_0 z_0/(H^2 + z_0^2)^{1/2}$, where z_0 is a free parameter characterizing the ray. By varying z_0 within the cross sectional range of the beam, a set of trajectories for the rays of the beam can be determined. However, not all the rays can be reflected back to the ionosonde. Only the rays which can return to the ionosonde are responsible for the observed diffuse echoes on the ionogram, and hence the intensity of spread F is proportional to the maximum difference of the reflection heights of those rays. The boundary conditions at $x = 0$ for a downgoing ray which can propagate straightly from the reference plane back to the ionosonde are defined to be $k_x = -k_0 H/(H^2 + z_f^2)^{1/2}$ and $k_z = -k_0 z_f/(H^2 + z_f^2)^{1/2}$, where z_f is the z coordinate of the ray on the reference plane. Those conditions can be satisfied only by rays with appropriate z_0. In other words, the conditions at $x = 0$ for the upgoing rays which can be received later by the ionosonde can not be predefined. Instead, z_0 and z_f have to be determined simultaneously.

Presented in Figure 2 are the two distinctive trajectories for two different groups of rays in the beam, where the background parameters used in the calculation are $\theta_0 = 50°$, $L = 50$ km, $\lambda_1 = 1$ km, $k_0^2 c^2/\omega_{pe0}^2 = 1$ and $\delta n_1/n_0 = \alpha = 0.1$. The rays which follow these trajectories can return to the ionosonde. These two trajectories are found to depend on the value of α. They approach each other and then merge into a single trajectory coincided with the x axis as the value of α decreases to zero. It is therefore shown that if the ionosonde transmitting beam is modelled by many rays having different initial locations on a reference plane, the spread F echoes can indeed be interpreted to be caused by the difference in the reflection heights (or the time delays) of the returned signals. The virtual height spread is thus proportional to the maximum difference Δx_{max} of these reflection heights. This spread disappears when the irregularities oriented in the meridian plane are absent. It should be noted that an ionosonde, like any receiver, has a limited sensitivity and requires a certain minimum "number of rays" from any height interval to be recognized as a signal. Therefore, the reflection height of this signal should be defined to be the average value over those of rays. In view of this, Δx_{max} defined in this study may not be a fully sensible measure of the spread F strength. Nevertheless, it indeed provides a qualitative indication.

We now employ the similar parameters to analyze the system of (7), (13), (18), and (19): $L = 50$ km, $\lambda_1 = 1$ km and $k_0^2 c^2/\omega_{pe0}^2 = 1$; z_0 is allowed to vary for determining the trajectories of the rays. Only taken into account are the trajectories of the rays detectable to the ionosonde for determining the maximum difference Δx_{max} from the reflection heights of these rays. Δx_{max} versus the magnetic dip angle θ_0 as calculated for $\alpha (= \delta n_1/n_0) = 0.005$, 0.01, 0.05 and 0.1

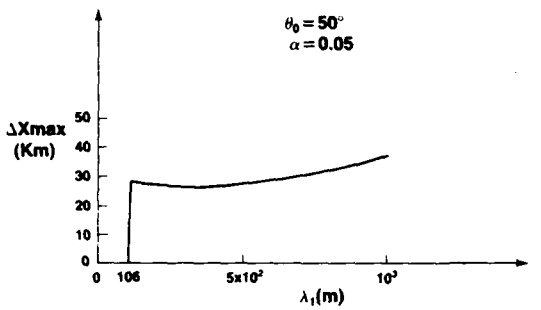

Fig. 5. The dependence of spread F on the scale length λ_1 of the irregularity, where $\theta_0 = 50°$ and $\alpha = 0.05$.

and presented in Figures 3*a*–3*d*. Shown in Figures 4*a*–4*c* are Δx_{max} versus the irregularity intensity α for $\theta_0 = 50°$, 68°, and 78° that correspond to magnetic dip angles at Arecibo, Boulder and Tromsø, respectively. The dependence of spread F on the scale length of the irregularity has also been examined for the case $\theta_0 = 50°$ and $\alpha = 0.05$. The result is presented in Figure 5 showing that spread F can only be caused by irregularities with scale lengths larger than about 106 m.

3. DISCUSSION AND CONCLUSIONS

A theoretical model of spread F echoes has been developed for determining the effects of the magnetic dip angle, irregularity intensity, and the polarization direction and the scale length of irregularity on the occurrence frequency and the intensity of spread F. We first show that irregularities polarized perpendicular to the meridian plane do not cause spread F. Therefore, only irregularities polarized within the meridian plane have been considered in the analyses for evaluating the aforementioned effects.

As shown in Figures 3*a*–3*d*, spread F becomes prominent as the magnetic dip angle exceeds about 5°. The reflection height spread Δx_{max} first increases rapidly to a maximum at about $\theta_0 = 8°$ (except for very low irregularity intensity, e.g., $\alpha = 0.001$, where the peak appears at $\theta_0 \cong 20°$) and then decreases monotonically to zero at $\theta_0 = 90°$. However, Δx_{max} is quite flat in the region from 20° to 70° (30° to 80° for $\alpha = 0.001$). Furthermore, Δx_{max} increases monotonically with the irregularity intensity as seen in Figures 4*a*, 4*b* and 4*c* for $\theta_0 = 50°$, 68°, and 78° corresponding, respectively, to the magnetic dip angles at Arecibo, Boulder, and Tromsø. While a near linear dependence is found in the $\theta_0 = 50°$ and 68° cases, Δx_{max} starts to approach a maximum at $\alpha = 0.02$ for $\theta_0 = 78°$. The dependence of spread F on the scale length λ_1 of irregularities has been examined for $\theta_0 = 50°$ and $\alpha = 0.05$. The result shown in Figure 5 indicates that spread F appears only when $\lambda_1 > 106$ m. The reflection height spread remains a fairly constant value from 106 m to about 500 m. This value then increases monotonically by 35% at $\lambda_1 = 1$ km which is the largest scale length employed in the analyses. Our model shows that spread F is quite insensitive to the magnetic dip angle. As long as the irregularity with the polarization within the meridian plane exists, significant spread F should be observed over a wide range of latitude including Arecibo, Boulder, and even Tromsø. In other words, the appearance of spread F should not depend upon the locations of the ionosondes. We, therefore, conclude that spread F echoes on the ionograms are caused by the irregularities with polarization directions within the meridian plane and the scale lengths greater than about 100 m. By contrast, irregularities with polarization directions perpendicular to the meridian plane do not give rise to spread F echoes.

The different occurrence frequencies of artificial spread F noticed at Arecibo, Boulder, and Tromsø are most probably due to the excitation of different types of irregularities. However, the large geomagnetic dip angle at Tromsø also plays an important role (see Figure 3), which works to substantially reduce the spread F strength at Tromsø. The *o* mode and *x* mode pump waves transmitted from the Boulder heating facilities cannot be separated as easily as those from the Arecibo or the Tromsø facilities. This fact can be evidenced by the measurements of HF wave-induced short-scale irregularities at Boulder [*Fialer*, 1974] showing that *x* mode can still excite short-scale irregularities though not as efficiently as *o* mode wave. The heater wave transmitted into the ionosphere from Tromsø, Norway, is a left (*x* mode) or right (*o* mode) hand circularly polarized wave propagating along the geomagnetic field. Therefore the generated irregularities (by either *o* mode or *x* mode) at Tromsø are expected to be magnetic field-aligned [*Kuo and Schmidt*, 1983]. Further, if the plasma inhomogeneity in the vertical direction is taken into account, the filamentation instability would be excited preferentially in the direction perpendicular to the meridian plane (i.e., the *y* direction of the coordinate system used in this work) in order to have symmetric high frequency sidebands. This, together with the effect of geomagnetic dip angle, may explain why spread F has never been observed since the Tromsø facilities were operated a few years ago. We also note that when the heater is operated in *o* mode at Arecibo, no spread F or change of reflec-

tion heights can be seen (L. M. Duncan, private communication, 1984). It then implies, based on the proposed model of spread F mechanism, that the o mode heater excited irregularities must be oriented in the y direction. This again agrees with the theoretical prediction of the generation of large-scale irregularities by the filamentation instability [*Kuo and Schmidt*, 1983] and supports the proposed model of spread F mechanism self-consistently.

Acknowledgments. This work was supported jointly, in part by the NSF grant ATM-8315322, in part by AFOSR grants AFOSR 83-0001 and 85-0133 at Polytechnic Institute of New York and by NASA grant NAG 5-270, and in part by the previous AFGL contract F19628-83-K-0024 at Massachusetts Institute of Technology.

REFERENCES

Duncan, L. M., and R. A. Behnke, Observations of self-focusing electromagnetic waves in the ionosphere, *Phys. Rev. Lett.*, *41*, 998–1001, 1978.

Fialer, P. A., Field-aligned scattering from a heated region of the ionosphere: Observation at HF and VHF, *Radio Sci.*, *9*, 923–940, 1974.

Frey, A., P. Stubbe, and H. Kopka, First experimental evidence of HF produced electron density irregularities in the polar ionosphere diagnosed by UHF radio star scintillations, *Geophys. Res. Lett.*, *11*, 523–526, 1984.

Kuo, S. P., and G. Schmidt, Filamentation instability in magneto plasmas, *Phys. Fluids*, *26*, 2529–2536, 1983.

Showen, R. L., and D. M. Kim, Time variations of HF-induced plasma waves, *J. Geophys. Res.*, *83*, 623–628, 1978.

Stubbe, P., H. Kopka, H. Lauche, M. T. Rietveld, A. Brekke, O. Holt, T. B. Jones, T. Robinson, A. Hedberg, B. Thide, M. Crochet, and H. J. Lotz, Ionospheric modification experiments in northern Scandinavia, *J. Atmos. Terr. Phys.*, *44*, 1025–1041, 1982.

Utlaut, W. F., A survey of ionospheric modification effects produced by high-power HF radio waves, *AGARD Conf. Proc.*, *138*, 3-1–3-16, 1973.

S. C. Kuo and S. P. Kuo, Department of Electrical Engineering, Polytechnic Institute of New York, Long Island Center, Farmingdale, NY 11735.

M. C. Lee, Research Laboratory of Electronics, Massachusetts Institute of Technology, Cambridge, MA 02139.

Radio Science, Volume 20, Number 3, Pages 539–545, May–June 1985

Simultaneous excitation of large-scale geomagnetic field fluctuations and plasma density irregularities by powerful radio waves

M. C. Lee

Research Laboratory of Electronics, Massachusetts Institute of Technology, Cambridge

S. P. Kuo

Polytechnic Institute of New York, Long Island Center, Farmingdale

(Received August 21, 1984; revised February 20, 1985; accepted February 28, 1985.)

We elaborate upon the physical mechanism of thermal filamentation instability of radio waves whose frequencies can be as low as in the VLF band and as high as in the SHF band. This instability can excite large-scale magnetic and plasma density fluctuations simultaneously in the ionosphere and magnetosphere. We comment on relevant experiments in terms of this instability and other mechanisms.

1. INTRODUCTION

Manifest ionospheric disturbances can be produced by powerful HF radio waves in ionospheric heating experiments, such as fluctuations in ionospheric density, plasma temperature, and the earth's magnetic field (see, for example, *Gurevich* [1978], *Fejer* [1979], *Stubbe et al.* [1982], and *Lee and Kuo* [1983*a*]). Unexpectedly large perturbations in the earth's magnetic field (~ 10.8 nT) were observed in Tromsø experiments with the EISCAT HF heating facilities [*Stubbe and Kopka*, 1981], and we predicted the coexistence of large-scale ionospheric irregularities [*Kuo and Lee*, 1983]. Whistler waves at frequencies close to, but less than, the local electron gyrofrequency are expected to cause both plasma density irregularities and geomagnetic field fluctuations in the ionosphere if MF signals are transmitted, or in the magnetosphere if VLF signals are injected [*Lee and Kuo*, 1984*a*]. Microwave transmissions at 2.45 GHz with central maximum power density of 230 W/m^2 from the conceptualized Solar Power Satellite are also expected to perturb the earth's magnetic field significantly in the ionosphere along the microwave beam [*Lee and Kuo*, 1984*b*]. Our theoretical analyses have shown that geomagnetic field fluctuations can be excited simultaneously with large-scale field-aligned ionospheric density by powerful radio waves. The frequencies of radio waves can be as low as in the VLF band and as high as in the SHF band.

Thermal filamentation instability excited by radio waves in the ionosphere and magnetosphere is responsible for the simultaneous perturbation in ionospheric density δN and geomagnetic field $\delta \mathbf{B}$. A nonoscillatory (i.e., purely growing) mode is associated with δN and $\delta \mathbf{B}$, whose magnitudes are interrelated uniquely by an equation characteristic of the thermal filamentation instability. Since the filamentation wave vector is perpendicular to the incident wave vector, the radio wave tends to be "self-focused" with this instability. One purpose of this paper is to elaborate upon the physical mechanism of thermal filamentation instability as presented in section 2, that leads to features distinctively different from those of thermal self-focusing instabilities [e.g., *Perkins and Valeo*, 1974; *Cragin et al.*, 1977; *Perkins and Goldman*, 1981]. In addition, we wish to comment on some relevant experiments in section 3 in terms of thermal filamentation instability and other mechanisms. Conclusions are finally drawn in section 4.

2. PHYSICAL MECHANISM OF THERMAL FILAMENTATION INSTABILITY

Radio waves, if intense enough, are able to excite thermal filamentation instability in the ionosphere and magnetosphere, that produces sideband and purely growing modes with wave vectors perpendicular to the propagation direction of radio waves. Magnetic field-aligned nonoscillatory modes (i.e., fila-

Paper number 5S0191.
0048-6604/85/005S-0191$08.00

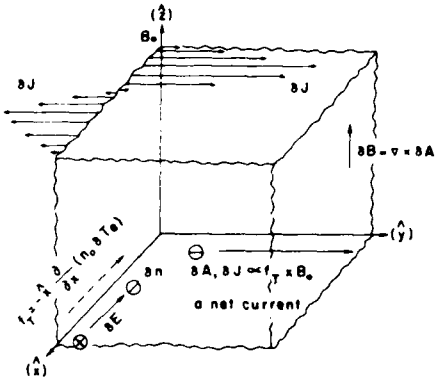

Fig. 1. The physical process leading to the simultaneous excitation of large-scale earth's magnetic field perturbations $\delta\mathbf{B}$ and plasma density irregularities δN by the thermal filamentation instability of powerful radio waves.

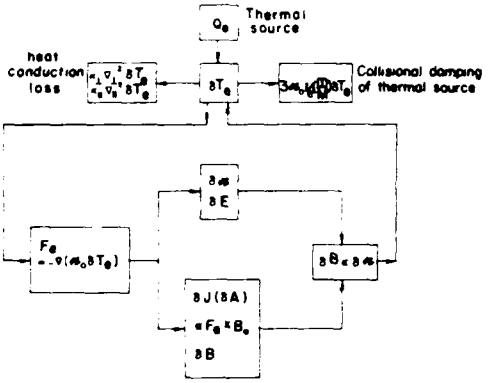

Fig. 2. The threshold condition and a positive feedback loop for the thermal filamentation instability.

ments of magnetostatic and ionospheric density fluctuations) are formed along the radio wave paths. They are caused by a nonlinear thermal effect due to radio wave–plasma interactions. We elucidate its physical mechanism as follows and diagram it in Figure 1.

The wave fields, that include the incident and sideband fields, interact with plasmas and consequently yields two types of nonlinear force: the ponderomotive force (or generally termed nonlinear Lorentz force) and the thermal pressure force. In generating field-aligned nonoscillatory modes, the thermal pressure force turns out to be larger than the ponderomotive force by a factor of $(\lambda/2\pi r_e)^2$ for modes with scale lengths λ less than $\pi r_e\,(2M/m)^{1/2}$ (~ 15 m in the ionosphere) and by a factor of (M/m) otherwise [*Kuo et al.*, 1983; *Lee and Kuo*, 1983*b*], where r_e and (M/m) are the electron gyroradius and the ratio of ion to electron masses, respectively. Ions cannot be effectively heated because of large cross-field heat diffusion loss. Thermal pressure force can be built up only in the electron gas. The dotted arrow in Figure 1 denotes such a force $\mathbf{f}_T = -\hat{x}(\partial/\partial x)(N_0\,\delta T_e)$ experienced by electrons across the earth's magnetic field ($\mathbf{B}_0 = \hat{z}B_0$).

Electron density fluctuations (δN) that are induced consequently by the thermal pressure force give rise to a self-consistent field ($\delta\mathbf{E} = \hat{x}\delta E$) associated with the excitation of the purely growing mode. While the net force acting on electrons is $(\mathbf{f}_T - eN_0\,\delta\mathbf{E})$, that on singly charged ions is $eN_0\,\delta\mathbf{E}$. These wave-induced forces combined with the orthogonal earth's magnetic field result in cross-field drift motions of electrons and ions at the velocities of $(\delta\mathbf{E} - \mathbf{f}_T/eN_0) \times \mathbf{B}_0/B_0^2$ and $(\delta\mathbf{E} \times \mathbf{B}_0/B_0^2)$, respectively. Therefore, a relative motion between electrons and ions at the velocity of $(\mathbf{f}_T/eN_0) \times \mathbf{B}_0/B_0^2$ results and produces a net current flowing along the direction of the y axis. This wave-induced current (and vector potential, $\delta\mathbf{A}$) varies sinusoidally along the x axis. It can be visualized as a combination of many sheetlike currents on the y-z plane with a thickness of half the scale length λ, flowing in opposite directions alternately. Or, equivalently, pairs of dipole current form within the radio wave–heated ionospheric region. Earth's magentic field fluctuations $\delta\mathbf{B}$ that result from the radio wave-induced current are field aligned. They point to the same direction as the geomagnetic field's, $\mathbf{B}_0$, because of $\nabla \times \delta\mathbf{A} = \Delta\mathbf{B} = \hat{z}\delta B$.

The physical mechanism of producing both $\delta\mathbf{B}$ and δN is summarized in Figure 2 with the aid of block diagrams, showing how a positive feedback loop can be formed for the thermal filamentation instability. In brief, electron temperature perturbation δT_e caused by radio wave heating produces a cross-field thermal pressure force $\mathbf{f}_T$ as the key nonlinearity of the thermal filamentation instability. This nonlinear force induces earth's magnetic field perturbation $\delta\mathbf{B}$ and ionospheric density irregularities δN that, subsequently, cause nonuniform electron heating and, then, perturbs the electron temperature in turn. It can be expected from the above delineated physical picture that $\delta N \propto \delta B$ because both of them are induced in proportion by $\mathbf{f}_T$. Such a relation has been, indeed, found in our detailed formulation of the theory with the following form [equation (2′) of *Lee and Kuo*, 1984*b*]:

$$\frac{\delta N}{N_0} \simeq \left\{1 + \frac{\nu_e}{\gamma}\left(\frac{2\pi c}{\lambda_\perp \omega_{pe}}\right)^2\left[1 + \frac{\Omega_e\Omega_i}{\nu_e\nu_i}\left(\frac{\lambda_\perp}{\lambda_\parallel}\right)^2\right]\right\}\left(\frac{\delta B}{B_0}\right) \qquad (1)$$

where the parameters, $\nu_e(\nu_i)$, $\Omega_e(\Omega_i)$, ω_{pe}, c, γ, $\lambda_\perp(\lambda_\parallel)$, and $N_0(B_0)$ have their conventional meanings of effective electron (ion) collision frequency, electron (ion) gyrofrequency, electron plasma frequency, the speed of light in vacuum, the growth rate of the instability, the perpendicular (parallel) scale length of the instability and the background ionospheric density (earth's magnetic field strength), respectively. The density perturbation, $\delta N/N_0$, is proportional linearly to the magnetic perturbation, $\delta B/B_0$, with a ratio greater than unity. If this ratio is close to unity, $\delta B/B_0$ comparable to $\delta N/N_0$ can be excited by the thermal filamentation instability. Otherwise, the earth's magnetic field perturbation is negligibly small as compared with the ionospheric density perturbation.

One might, however, be skeptical about the possibility of producing $\delta B/B_0 \simeq \delta N/N_0$ based on the following argument. If $\delta B/B_0 \simeq \delta N/N_0$, then both $\delta B/B_0$ and $\delta N/N_0$ must be extremely small compared with $\delta T_e/T_0$ according to the "MHD equilibrium" condition:

$$\frac{\delta N}{N_0} \simeq \frac{\delta B}{B_0} \lesssim \frac{\beta}{2}\frac{\delta T_e}{T_0} \tag{2}$$

where β is the ratio of kinetic to magnetic pressure, namely, $N_0 T_0/(B_0^2/8\pi) \sim 10^{-5}$ for typical ionospheric parameters. It is apparent from (2) that, in "MHD equilibrium," $\delta T_e/T_0$ ($\sim 2 \times 10^2$) is absurdly unrealistic even for 0.1% of $\delta N/N_0$ or $\delta B/B_0$. The argument that $\delta B/B_0$ must be extremely small under the "MHD equilibrium" condition is certainly true. This fact can be also seen from (1), which requires $\delta B/B_0 = 0$ when $\gamma = 0$, corresponding to the "MHD equilibrium" condition either before the onset or after the saturation of the thermal filamentation instability. During the linear stage of the instability (i.e., the growth rate (γ) = a nonzero constant), $\delta B/B_0$ and $\delta N/N_0$ are related by (1) and significant geomagnetic field fluctuations can be produced by powerful radio waves. In other words, the geomagnetic field perturbation caused by powerful radio waves via the thermal filamentation instability is a transient phenomenon, whose duration may be estimated from the growth rate of the instability. It is reasonable to define this duration to be the period for achieving the seven e-folds of magnitude above the thermal fluctuation level, namely, $7\gamma^{-1}$.

The parallel wave number $k_\parallel$ is zero for ideal field-aligned modes. Nevertheless, a small (compared to $k_\perp$) but finite $k_\parallel$ can be introduced by inhomogeneity effects associated with either the background ionospheric density or the finite cross section of the radio wave beam. The inhomogeneity effects have been reasonably ignored in our previous studies of VLF, MF, and HF cases. This is because the instability becomes effective in the ionosphere and magnetosphere for modes with scale lengths less than the scale sizes of the background plasma density gradients and the linear dimensions of wave beam cross sections by, at least, 2 orders of magnitude. By contrast, the inhomogeneity effect imposed by the narrow microwave beam cannot be neglected in the case of the Solar Power Satellite. The parallel scale length $\lambda_\parallel$, which is of the order of the microwave beam size (~ 10 km), renders the factor enclosed by the brackets in (1) to be much greater than unity in the ionospheric F region. Physically, large heat conduction loss along the geomagnetic field inhibits the thermal filamentation instability from producing significant earth's magnetic field perturbation in the F region. Parallel heat conduction loss is, however, drastically reduced by the large electron-neutral collisions in the E region. Therefore, the thermal filamentation instability can operate effectively in the E region but not the F region in the solar power satellite case.

Parallel heat conduction loss may significantly enhance the threshold of the instability whose full expression is given by [equation (6′) of *Lee and Kuo*, 1984*b*]

$$\left|\frac{e\varepsilon_{th}}{mc}\right| = f\frac{2\pi V_t}{\lambda_\perp}\left[2\frac{m}{M} + \left(\frac{2\pi V_t}{\lambda_\perp \Omega_e}\right)^2 + \left(\frac{2\pi V_t}{\lambda_\parallel \nu_e}\right)^2\right]^{1/2} \tag{3}$$

where ε_{th}, $\lambda_\perp(\lambda_\parallel)$, $m(M)$, and V_t are the threshold wave field intensity, the perpendicular (parallel) scale length, the electron (ion) mass, and the electron thermal velocity, respectively; the factor, f, can be a function of ω_0, ω_{pe}, Ω_e, and $\lambda_\perp$ depending upon the frequency (ω_0) of the radio waves. The thermal filamentation instability requires a threshold basically because the sideband and purely growing modes are not normal modes but nonlinearly driven modes in space plasmas. The threshold level (ε_{th}) is determined in (3), representing the energy balance between the driving thermal source of the instability (i.e., the collisional dissipation of radio wave energy) and the damping processes denoted by the three terms: $2(m/M)$, $(2\pi V_t/\lambda_\perp \Omega_e)^2$, and $(2\pi V_t/\lambda_\parallel \nu_e)^2$. These three damping terms correspond to the collisional damping of the thermal source, the cross-field heat conduction loss, and the parallel heat conduction loss, re-

spectively. The first term dominates for the instability with $\lambda_\perp > (2M/m)^{1/2}\pi V_t/\Omega_e$ (~ 15 m in the ionosphere) and $(\lambda_\parallel/\lambda_\perp) > (\Omega_e/\nu_e)$. But, parallel heat conduction loss becomes the dominant damping process if $\lambda_\parallel/\lambda_{MFP} > \pi(2M/m)^{1/2}$, where λ_{MFP} is the electron mean free path.

In general, the instability with large-scale lengths requires lower thresholds, since $|\varepsilon_{th}| \propto \lambda_\perp^{-1}$. The favorable excitation of geomagnetic field fluctuations by large-scale modes can be seen in (1), which for highly field aligned modes, can be reduced to

$$\frac{\delta N}{N_0} \simeq \left[1 + \frac{\nu_e}{\gamma}\left(\frac{2\pi c}{\lambda_\perp \omega_{pe}}\right)^2\right]\left(\frac{\delta B}{B_0}\right) \tag{4}$$

where the growth rate γ increases generally with scale lengths. Smaller ratios of $\delta N/N_0$ to $\delta B/B_0$ are therefore associated with larger-scale modes, namely, significant geomagnetic field fluctuations can be excited mainly through large-scale thermal filamentation instability.

It is interesting to note that the threshold condition given by (3) is independent of the electron collision frequency ν_e for the excitation of "large-scale, highly field aligned" modes, that is,

$$\left|\frac{e\varepsilon_{th}}{mc}\right| \simeq f\frac{4\pi V_t}{\lambda_\perp}\left(\frac{m}{M}\right) \tag{5}$$

where the factor f is not a function of ν_e. This is understandable because both the generation rate (the left-hand side of (5)) and the damping rate of the thermal source are proportional to ν_e. More specifically, electron collisions with ions or neutrals convert the radio wave energy into the thermal source of the filamentation instability; meanwhile, the induced electron temperature perturbations are also determined by the collisional loss of wave-generated heat. It should be stressed that electron collisions do not weaken the purely growing modes (i.e., the magnetostatic and ionospheric density fluctuation) because electrons and ions move together in the wave vector direction of the purely growing mode.

The expressions of the growth rate have been found to be generally proportional to ν_e. This offers another evidence that electron collisions enhance the instability. The principal reason is that large cross-field mobility of charged particles is conducive to the establishment of collective oscillations, i.e., the field-aligned purely growing fluid modes. The cross-field mobility is greatly enhanced by electron collisions. Another interesting thing to note is that the relationship between δN and δB shown in (4) turns out to be not a function of ν_e because $\gamma \propto \nu_e$.

The generation of large-scale ionospheric density irregularities by powerful radio waves have been investigated, for example, by *Perkins and Valeo* [1974] and *Perkins and Goldman* [1981] via the thermal self-focusing instability, and by *Fejer* [1973], *Cragin and Fejer* [1974], and *Cragin et al.* [1977] via the thermal stimulated Brillouin backscattering instability. These two instabilities have their own distinctive features in, for instance, the threshold conditions discussed in next section, though they are believed to be physically equivalent. The simultaneous excitation of large-scale earth's magnetic field fluctuations and ionospheric density irregularities is the important discovery in our theory of thermal filamentation instability. In addition, the geomagnetic field effect on the high-frequency sideband mode that was ignored in the previous theories has been taken into account in our formulation of the instability.

The inclusion of this effect exhibits its important contribution to the driving sources of sideband modes (especially as $\omega_0 < \Omega_e$) that satisfy the following Fourier transform wave equation

$$\left[\left(k_0^2 + k^2 - \frac{\omega_0^2}{c^2}\right)\mathbf{I} - k_0^2\hat{z}\hat{z} - k^2\hat{x}\hat{x} - ik_0\frac{\hat{c}}{\hat{c}x}(\hat{x}\hat{z} - \hat{z}\hat{x})\right]\boldsymbol{\varepsilon}_1 = i\frac{4\pi\omega_0}{c^2}(\mathbf{J}_S + \mathbf{J}_N + \mathbf{J}_M) \tag{6}$$

where $\mathbf{I}$ is the unit dyadic; $\hat{z}$ and $\hat{x}$ denote the unit vectors taken along the direction of the geomagnetic field ($\mathbf{B}_0 = \hat{z}B_0$) and the filamentation wave vector ($\mathbf{k} = \hat{x}k$). For simplicity, the radio wave has been assumed to propagate along the geomagnetic field. The wave-induced current density includes three parts: $\mathbf{J}_S = -eN_0\mathbf{V}_1$, $\mathbf{J}_N = eN\mathbf{V}_0$, and $\mathbf{J}_M = eN_0\mathbf{V}_M$, where

$$\mathbf{V}_j = i\frac{e}{m}\frac{\omega_0}{(\omega_0^2 - \Omega_e^2)}\left[\boldsymbol{\varepsilon}_{j\perp} + \hat{z}\left(1 - \frac{\Omega_e^2}{\omega_0^2}\right)\varepsilon_{jz} + i\frac{\Omega_e}{\omega_0}\hat{z}\times\boldsymbol{\varepsilon}_j\right] \qquad j = 0 \text{ or } 1 \tag{7}$$

are the electron quiver velocities responding to the incident wave field ($\boldsymbol{\varepsilon}_0$) and the sideband field ($\boldsymbol{\varepsilon}_1$), respectively;

$$\mathbf{V}_M = -i\frac{e}{mc}\frac{\omega_0}{(\omega_0^2 - \Omega_e^2)}\left[\mathbf{V}_0\times\hat{z} + i\frac{\Omega_e}{\omega_0}\mathbf{V}_0\right]\delta B \tag{8}$$

is the electron velocity perturbation caused by the $\mathbf{V}_0 \times \delta\mathbf{B}$ Lorentz force. $\mathbf{J}_S$ is the linear response of electrons to the sideband field $\boldsymbol{\varepsilon}_1$, whereas $\mathbf{J}_N$ and $\mathbf{J}_M$ are the nonlinear beating currents stemming from the nonlinear coupling between the purely growing

modes (δN or $\delta \mathbf{B}$) and the incident wave field (ε_0). On one hand, the sideband mode is produced by the parametric interaction of the incident radio wave and the purely growing modes. On the other hand, the purely growing modes are driven by the thermal pressure force ($-\nabla(N_0 \delta T_e)$) that is caused by the ohmic dissipation of the incident and sideband modes at the rate of $Q_e = 2\nu_e N_0 m(\mathbf{V}_0^* \cdot \mathbf{V}_1 + \mathbf{V}_0 \cdot \mathbf{V}_1^*)$.

3. COMMENTS ON RELEVANT EXPERIMENTS

The thermal filamentation instability of VLF waves (whistlers) can be excited in the magnetosphere rather than the ionosphere. This is because the instability can only be excited in the frequency range $\Omega_e/2 < \omega_0 < \Omega_e$ by whistlers and $\Omega_e/2\pi$ is about 1.4 MHz in the ionosphere and 13.65 KHz in the magnetosphere at $L = 4$. Although VLF wave injection experiments have been performed actively, for example, at Siple, Antarctica, the ground-based transmitters are usually operated in a pulsed-wave mode with duration of a few seconds. These VLF wave pulses have been used to study, primarily, coherent wave-particle interactions in the magnetosphere such as the wave amplification, the triggering of wave emissions, the induced particle precipitation, etc. (see, for example, *Helliwell* [1983]). However, the excitation of thermal filamentation instability in the magnetosphere requires the continuous operation of VLF transmitters for a few minutes because of the small electron collision frequency (~ 0.1 Hz) and then the small growth rates (10^{-3} to 10^{-2} Hz). Experiments can be planned with the Siple transmitter or more powerful U.S. Navy communication transmitters operated in CW modes and also with spacecrafts, for instance, the ISEE 1 to monitor the VLF wave-induced magnetospheric disturbances.

The thermal filamentation instability can be excited in the ionosphere by radio waves whose frequencies exceed half the electron gyrofrequency (~ 0.7 MHz). The ionospheric heating facilities located at Arecibo and Tromsø currently operate in the HF band at lowest frequencies of the order of 3 MHz (J. A. Fejer, private communication, 1984). Those in U.S.S.R. are also primarily HF transmitters except the one near Moscow that operates at a frequency (~ 1.35 MHz) near the electron gyrofrequency [*Gurevich and Migulin*, 1982]. Unexpectedly large geomagnetic field perturbation of the order of 10 nT had been caused by the Tromsø transmitter [*Stubbe and Kopka*, 1981; *Stubbe et al.*, 1982] and we explain it in terms of the thermal filamentation instability [*Kuo and Lee*, 1983]. This instability needs several minutes to be developed under the experimental conditions at Tromsø. This characteristic growth time is consistent with the observations that geomagnetic perturbation increased regularly with the operation time of radio waves in the range from 10 to 360 s [*Stubbe et al.*, 1982]. Another interpretation of magnetic fluctuations is that they are caused by perturbations in the steady currents (i.e., the auroral electrojet) flowing in the ionosphere caused by perturbations in the ionospheric conductivity [*Fejer and Krenzien*, 1982, and references therein]. One would expect from this mechanism that increased magnetic field fluctuations are associated with more intense electrojet current for future experimental verification. The source(s) of magnetic fluctuations can be unambiguously identified by in situ measurements performed by rockets or spacecrafts in the modified ionosphere. While the auroral electrojet as a line source is located at an altitude of about 100 km above the earth's crest, the radio wave-induced dc current appears in a higher and broader heated ionospheric region below the reflection height of the incident heater wave. A unique feature of thermal filamentation instability is that the simultaneously excited magnetic and density fluctuations have identical characteristic scale lengths and growth rates. Moreover, the strengths of these two types of fluctuations are interrelated specifically by (1). The in situ measurements would provide an excellent diagnosis of the heated ionosphere to test the theories in these aspects.

The theories of *Perkins and Valeo* [1974] and *Cragin et al.* [1977] have been examined by *Farley et al.* [1983] and *Frey and Duncan* [1984] as candidate mechanisms of producing large-scale irregularities in overdense ionospheric heating experiments at Arecibo. The thresholds of Perkins and Valeo theory are significantly higher than those of Cragin et al. theory, especially, in generating kilometer-scale irregularities. The measured threshold powers for exciting a few kilometer-scale irregularities in the Arecibo experiments agree reasonably well with the theoretical values of Cragin et al. However, the observed hundreds of meter-scale irregularities cannot be excited by Cragin et al. instability because the required threshold powers P_{th} are too large according to the scaling law: $P_{th} \propto \lambda_\perp^4$ (in contrast to $\lambda_\perp^2$ of *Perkins and Valeo* [1974]). The detection of hundreds meter-scale irregularities by UHF scintillation technique was recently performed by *Frey et al.* [1984] in

Tromsø heating experiments. Frey et al. considered three candidate mechanisms including *Perkins and Valeo* [1974], *Cragin et al.* [1977], and ours [*Kuo and Lee*, 1983]. They reported that the thresholds of our thermal filamentation instability were consistent with their measured ones, whereas those of the other two instabilities were higher by at least a factor of 100.

It has been predicted that the conceptualized Solar Power Satellite (SPS) will produce large-scale ionospheric irregularities [*Perkins and Goldman*, 1981] and also possibly together with the simultaneous excitation of earth's magnetic field fluctuations [*Lee and Kuo*, 1984*b*]. A rocket experiment named Microwave Ionosphere Nonlinear Interaction Experiment (MINIX) was carried out recently by the Kyoto University group in Japan to simulate the SPS [*Matsumoto et al.*, 1984]. The microwaves were transmitted at a frequency of 2.45 GHz with incident power densities comparable to the envisioned intensity of 230 W m^2 in SPS. The beam width of order of a few meters is, however, less than that (~ 10 km) proposed for SPS by, at least, 3 orders of magnitude. The excitation of electron cyclotron waves and electron plasma waves were observed, but it is not surprising that ionospheric irregularities and other predicted phenomena could not be produced in MINIX because of the rather narrow microwave beam. The beam size is probably a very crucial parameter in the simulation experiments of SPS.

4. CONCLUSIONS

Thermal filamentation instability can be excited in space plasmas by powerful radio waves whose frequencies exceed half the electron gyrofrequency. Large-scale magnetic and plasma density fluctuations can be simultaneously created if the transmitter of radio waves is operated continuously for a few minutes. During its linear stage, this instability is able to produce significantly large earth's magnetic field fluctuations in the ionosphere and magnetosphere that is a low-β plasma. A threshold is required for the instability fundamentally because the high-frequency sidebands and the purely growing modes are not eigenmodes rather the nonlinearly driven modes. The off-resonance effect (i.e., detuning) imposes the primary damping mechanism of the instability. The electron-ion (electron-neutral) collisions play the following roles in the excitation of thermal filamentation instability: (1) to convert the radio wave energy into the driving heat source of the instability, (2) to reduce the electron temperature perturbations induced by the heat source; this is also the principal process of energy loss in determining the threshold level of large-scale, highly field aligned instability (see equation (3)), and it is therefore commonly termed "electron-ion (electron-neutral) cooling" [e.g., *Farley et al.*, 1983], and (3) to facilitate cross-field mobility of charged particles for establishing the collective oscillations (i.e., the field-aligned purely growing modes) and, as a consequence, the growth rate of the instability is generally proportional linearly to the electron-ion (electron-neutral) collision frequency.

We have proposed the thermal filamentation instability as the cause of HF wave-induced geomagnetic field perturbation in Tromsø ionospheric heating experiments [*Stubbe and Kopka*, 1981; *Stubbe et al.*, 1982]. The thresholds of this instability were found to agree with the measured ones in recent Tromsø experiments [*Frey et al.*, 1984]. However, our proposed mechanism and the one suggested by *Fejer and Krenzien* [1982] among others need to be further verified in the future experiments with, for instance, coordinated in situ measurements in the heated ionospheric region. The thermal filamentation instability of VLF waves (whistlers) can occur in the magnetosphere with growth times of a few minutes. Our work thus suggests a wave plasma interaction process for future VLF wave injection experiments to explore with the operation of transmitters in a CW rather than pulsed wave mode. The Japanese simulation experiments of Solar Power Satellite [*Matsumoto et al.*, 1984] unfortunately cannot test the Perkins and Goldman's predictions and ours of microwave-induced ionospheric disturbances because of the intrinsic limitation on the transmitter size in a rocket. The space station under consideration by NASA probably can provide better experimental conditions for the future simulation experiments.

Acknowledgments. The work at Massachusetts Institute of Technology was supported by NASA grant NAG 5-270 and in part by the previous AFGL contract F19628-83-K-0024; that at Polytechnic Institute of New York was supported jointly by the NSF grant ATM-8315322 and in part by Air Force Office of Scientific Research grant AFOSR-83-0001 and 85-0133.

REFERENCES

Cragin, B. L., and J. A. Fejer, Generation of large-scale field-aligned irregularities in ionospheric modification experiments, *Radio Sci.*, 9, 1071, 1974.

Cragin, B. L., J. A. Fejer, and E. Leer, Generation of artificial spread F by a collisionally coupled purely growing parametric instability, *Radio Sci.*, *12*, 273, 1977.

Farley, D. T., C. LaHoz, and B. G. Fejer, Studies of the self-focusing instability at Arecibo, *J. Geophys. Res.*, *88*, 2093, 1983.

Fejer, J. A., Generation of large-scale field-aligned density irregularities in ionospheric heating experiments, *AGARD Conf. Proc.*, *138*, 13-1, 1973.

Fejer, J. A., Ionospheric modification and parametric instabilities, *Rev. Geophys.*, *17*, 135, 1979.

Fejer, J. A., and E. Krenzien, Theory of generation of ULF pulsations by ionospheric modification experiments, *J. Atmos. Terr. Phys.*, *44*, 1075, 1982.

Frey, A., and L. M. Duncan, Simultaneous observation of HF-enhanced plasma waves and HF-wave self-focusing, *Geophys. Res. Lett.*, *11*, 677, 1984.

Frey, A., P. Stubbe, and H. Kopka, First experimental evidence of HF produced electron density irregularities in the polar ionosphere; diagnosed by UHF radio star scintillations, *Geophys. Res. Lett.*, *11*, 523, 1984.

Gurevich, A. V., *Nonlinear Phenomena in the Ionosphere*, vol. 10, *Physics and Chemistry in Space*, Springer-Verlag, New York, 1978.

Gurevich, A. V., and V. V. Migulin, Investigations in the U.S.S.R. of nonlinear phenomena in the ionosphere, *J. Atmos. Terr. Phys.*, *44*, 1019, 1982.

Helliwell, R. A., Controlled stimulation of VLF emissions from Siple Station, Antarctica, *Radio Sci.*, *18*, 801, 1983.

Kuo, S. P., and M. C. Lee, Earth magnetic field fluctuations produced by filamentation instabilities of electromagnetic heater waves, *Geophys. Res. Lett.*, *10*, 979, 1983.

Kuo, S. P., B. R. Cheo, and M. C. Lee, The role of parametric decay instabilities in generating ionospheric irregularities, *J. Geophys. Res.*, *88*, 417, 1983.

Lee, M. C., and S. P. Kuo, Ionospheric irregularities and geomagnetic field fluctuations due to ionospheric heating, Proceedings of the International Symposium on Active Experiments in Space, *ESA Spec. Publ.*, *95*, 81–89, 1983*a*.

Lee, M. C., and S. P. Kuo, Excitation of upper hybrid waves by a thermal parameteric instability, *J. Plasma Phys.*, *30*, 463, 1983*b*.

Lee, M. C., and S. P. Kuo, Excitation of magnetostatic fluctuations by filamentation of whistlers, *J. Geophys. Res.*, *89*, 2289, 1984*a*.

Lee, M. C., and S. P. Kuo, Earth's magnetic field perturbations as the possible environmental impact of the conceptualized solar power satellite, *J. Geophys. Res.*, *89*, 11,043, 1984*b*.

Matsumoto, H., N. Kaya, S. Miyatake, I. Kimura, and M. Nagatomo, Rocket experiment on nonlinear interaction of high power microwave energy beam with the ionosphere: Project-MINIX for future solar power satellite, paper presented at 21st General Assembly Open Symposium on Active Experiments in Space Plasmas, URSI, Florence, Italy, Aug. 28 to Sept. 5, 1984.

Perkins, F. W., and M. V. Goldman, Self-focusing of radio waves in an underdense ionosphere, *J. Geophys. Res.*, *86*, 600, 1981.

Perkins, F. W., and E. J. Valeo, Thermal self-focusing of electromagnetic waves in plasmas, *Phys. Rev. Lett.*, *32*, 1234, 1974.

Stubbe, P., and H. Kopka, Generation of Pc 5 pulsations by polar electrojet modulation: First experimental evidence, *J. Geophys. Res.*, *86*, 1606, 1981.

Stubbe, P., et al., Ionospheric modification experiments in northern Scandinavia, *J. Atmos. Terr. Phys.*, *44*, 1025, 1982.

S. P. Kuo, Polytechnic Institute of New York, Long Island Center, Farmingdale, NY 11735.

M. C. Lee, Research Laboratory of Electronics, Massachusetts Institute of Electronics, 36-389, Cambridge, MA 02139.

J. Plasma Physics (1986), *vol.* 35, *part* 1, *pp.* 177–184
Printed in Great Britain

Resonant electron diffusion as a saturation process of the synchrotron maser instability

By M. C. LEE

Research Laboratory of Electronics, Massachusetts Institute of Technology, Cambridge, Massachusetts 02139, USA

AND S. P. KUO

Polytechnic Institute of New York, Long Island Center, Farmingdale, New York 11735, USA

(Received 27 September 1985)

The theory of resonant electron diffusion as an effective saturation process of the auroral kilometric radiation has been formulated. The auroral kilometric radiation is assumed to be amplified by the synchrotron maser instability that is driven by an electron distribution of the loss-cone type. The calculated intensity of the saturated radiation is found to have a significantly lower value in comparison with that caused by the quasi-linear diffusion process as an alternative saturation process. This indicates that resonant electron diffusion dominates over quasi-linear diffusion in saturating the synchrotron maser instability.

1. Introduction

Coherent electromagnetic radiation can be generated in a magnetized non-Maxwellian plasma by the synchrotron maser instability. This instability occurs under the conditions of inverted population, and stems from the relativistic mass dependence of the electron gyrofrequency that gives rise to phase bunching in the electron gyration orbits (see, for example, Bekefi, Hirshfield & Brown 1961). The operation of this instability has been suggested by, for instance, Melrose (1976) and Wu & Lee (1979) to be responsible for auroral kilometric radiation (see, for example, Gurnett 1974; Benson 1985 and references therein).

The optimum environment for the excitation of this instability in space plasmas is provided by the following processes that invert the population and form the non-Maxwellian electron distribution for lasing. Kilovolt electric potential drops are believed to exist along the auroral field lines during the inverted-V events (e.g. Gurnett & Frank 1973; Lin & Hoffman 1982 and references therein). Although the depletion of the background electrons to a very low level is expected because of the parallel electric field, the upgoing electrons that originate in the reflected plasma-sheet electrons introduce a loss-cone distribution. The non-Maxwellian electron distribution thus created is capable of producing intense coherent electromagnetic radiation in the upper atmosphere (Benson 1985).

The synchrotron maser instability converts the electron energy into coherent radiation. More specifically, the amplification of electromagnetic radiation occurs at the expense of the kinetic energy of electrons whose perpendicular momentum falls in the range where the electron distribution function has a positive slope. The saturation of this instability is, therefore, carried out by processes that can decrease the positive slope of the momentum distribution. A quasi-linear diffusion process has been analysed by Wu *et al.* (1981) to evaluate the saturation level of the auroral kilometric radiation. This diffusion process suppresses the instability by driving electrons into the lower velocity region, i.e. by reducing the positive gradient of the electron distribution function. Since the radiation frequency is less than, but very close to, the electron gyrofrequency, resonance broadening was also examined by Wu *et al.* as another potential saturation process. They found that the saturation wave energy would be one order of magnitude higher if resonance broadening, rather than quasi-linear diffusion, were considered to be the primary saturation process. In other words, quasi-linear diffusion dominates over resonance broadening as a saturation process of the synchrotron maser instability in generating auroral kilometric radiation.

A computer simulation of auroral kilometric radiation was performed later by Wagner *et al.* (1983). It shows that the synchrotron maser instability saturates when the resonant electrons diffuse into the loss cone as a result of the turbulent scattering of particles by the amplified radiation. The turbulent scattering means the resonant broadening due to the perturbations on the particle trajectories caused by the amplified radiation whose saturation intensities can be determined by computer simulation and analytically from our equation (17). The resonant electrons referred to are those that satisfy the synchrotron maser resonance condition: $\omega_r - \Omega - k_z v_z = 0$ where ω_r is the real part of the radiation frequency, Ω defined by $eB_0/\gamma mc$ is the relativistic electron gyrofrequency, k and v represent the wavenumber of radiation and the electron velocity, respectively. The subscript z denotes the z axis of a rectangular reference frame taken along the geomagnetic field. The parameters, e, m, c, B_0, and γ defined by $(1-v^2/c^2)^{-\frac{1}{2}}$, have their respective conventional meanings of electron charge, electron rest mass, the speed of light in vacuum, the geometric field intensity, and the relativistic factor. In the present paper, we investigate analytically this computer simulated physical process. An upper bound of the corresponding saturated radiation can then be derived analytically, and compared quantitatively with the saturated radiation deduced from the quasi-linear diffusion saturation process.

The formulation of the resonant electron diffusion is presented in § 2, starting with the relativistic Vlasov equation. This is followed by a quantitative analysis and comparison of resonant electron diffusion with quasi-linear diffusion as the dominant process that causes the saturation of the synchrotron maser instability in the production of auroral kilometric radiation. A summary and conclusions are presented in § 3.

2. Formalism

2.1. *Resonant electron diffusion*

Resonant diffusion of the background electron distribution in velocity space results from the interaction of electrons with the amplified electromagnetic radiation. We use the following relativistic Vlasov equation

$$\left\{\frac{\partial}{\partial t}+(\mathbf{p}/\gamma m).\nabla-e[\mathbf{E}+(\mathbf{p}/\gamma mc)\times(\mathbf{B}+\hat{z}B_0)].\nabla_{\mathbf{p}}\right\}f=0, \tag{1}$$

where $\mathbf{p}$ is the electron momentum and $\mathbf{B}_0$ is the background geomagnetic field assumed to be uniform. $\mathbf{E}$ and $\mathbf{B}$ designate the wave fields of the amplified radiation, which is assumed to have a right-hand circular polarization, that is,

$$\left.\begin{aligned}\mathbf{E} &= \sum_k (\hat{x}+i\hat{y})\,\epsilon\, e^{i(kz-\omega t)},\\ \mathbf{B} &= -i\sum_k (\hat{x}+i\hat{y})\,(kc/\omega)\,\epsilon\, e^{i(kz-\omega t)}\end{aligned}\right\} \tag{2}$$

where $\omega(=\omega(k))$ and $\epsilon(=\epsilon(k))$ are the wave frequency and field intensity of the amplified radiation, respectively.

The distribution function (f) is assumed to be a linear combination of the background ($\langle f\rangle$) and the perturbation (δf) portions:

$$f=\langle f\rangle+\delta f=f_0+f_1+\delta f_0+\delta f_1$$

where $\langle f\rangle = f_0+f_1$ and $\delta f=\delta f_0+\delta f_1$. The four parts of the distribution function, f_0, f_1, δf_0 and δf_1, correspond to the unperturbed background distribution, the perturbation on the background distribution (a second-order effect), the phase coherent linear density perturbation (a first-order effect), and the phase coherent nonlinear density perturbation (a third-order effect), respectively. The unperturbed background distribution (f_0) is of the loss-cone type given by

$$f_0(P_\perp,P_z)=\frac{1}{j!}\pi^{-\frac{1}{2}}(\Delta P_j)^{-(2j+3)}P_\perp^{2j}\exp(-P^2/\Delta P_j^2), \tag{3}$$

where $j(>0)$ is the loss-cone index, $\Delta P_j=[mT_e/(\frac{1}{2}+\frac{1}{3}j)]^{\frac{1}{2}}$, and $P^2=P_\perp^2+P_z^2$. The phase coherent linear (δf_0) and nonlinear (δf_1) density perturbations are caused by the instability via wave–particle resonant interaction. The phase incoherent density perturbation due to nonlinear wave–wave interaction will not be included in our analysis, for simplicity. However, it should be pointed out that when the amplified wave field grows to a significantly high level, the wave–wave interaction process may also become important and contribute additively to the saturation of the instability.

Along the unperturbed trajectory $d\mathbf{r}/dt=\mathbf{P}/\gamma m$ and $d\mathbf{P}/dt=-\Omega\mathbf{P}\times\hat{z}$, the governing equations deduced from (1) for perturbations of the distribution function are given by

$$\frac{d}{dt}\delta f_0=e\left[\mathbf{E}+\left(\frac{\mathbf{P}}{\gamma mc}\right)\times\mathbf{B}\right].\nabla_{\mathbf{P}}f_0, \tag{4}$$

$$\frac{d}{dt}f_1=e\left\langle\left[\mathbf{E}^*+\left(\frac{\mathbf{P}}{\gamma mc}\right)\times\mathbf{B}^*\right].\nabla_{\mathbf{P}}(\delta f_0+\delta f_1)+\text{c.c.}\right\rangle, \tag{5}$$

$$\frac{d}{dt}\delta f_1 = e\left[\mathbf{E} + \left(\frac{\mathbf{P}}{\gamma mc}\right) \times \mathbf{B}\right] . \nabla_{\mathbf{P}} f_1, \tag{6}$$

where both c.c. and the superscript * indicate the complex conjugate. Integrating (4) along the unperturbed trajectory, one obtains the phase coherent density perturbation due to the instability,

$$\delta f_0 = \sum_k i \frac{e\epsilon e^{i(kz-\omega t)}}{\omega - \Omega - kv_z} e^{i\theta}\left[\left(1 - \frac{kP_z}{\gamma m\omega}\right)\frac{\partial}{\partial P_\perp} + \frac{kP_\perp}{\gamma m\omega}\frac{\partial}{\partial P_z}\right] f_0 \tag{7}$$

where $\theta = \tan^{-1}(Py/Px)$.

Similarly, integrating (6) leads to

$$\delta f_1 = \sum_k i \frac{e\epsilon e^{i(kz-\omega t)}}{\omega - \Omega - kv_z} e^{i\theta}\left[\left(1 - \frac{kP_z}{\gamma m\omega}\right)\frac{\partial}{\partial P_\perp} + \frac{kP_\perp}{\gamma m\omega}\frac{\partial}{\partial P_z}\right] f_1. \tag{8}$$

Substituting (7) and (8) into (5) yields

$$\frac{d}{dt} f_1 = \sum_k ie^2|\epsilon|^2 e^{-i(\omega-\omega^*)t}\left[\left(1 - \frac{kP_z}{\gamma m\omega^*}\right)\left(\frac{\partial}{\partial P} + \frac{1}{P_\perp}\right) + \left(\frac{kP_\perp}{\gamma m\omega^*}\right)\frac{\partial}{\partial P_z}\right]$$
$$\times \frac{1}{(\omega - \Omega - kv_z)}\left[\left(1 - \frac{kP_z}{\gamma m\omega}\right)\frac{\partial}{\partial P_\perp} + \left(\frac{kP_\perp}{\gamma m\omega}\right)\frac{\partial}{\partial P_z}\right]\langle f\rangle + \text{c.c.} \tag{9}$$

which, after being integrated along the unperturbed trajectory, becomes

$$f_1 = \sum_k \frac{e^2|\epsilon|^2}{|\omega|^2} e^{-i(\omega-\omega^*)t}\left\{\frac{1}{P_\perp}\frac{\partial}{\partial P_\perp} P_\perp \frac{\partial}{\partial P_\perp} + \left[\left(\frac{\partial}{\partial P_\perp} + \frac{1}{P_\perp}\right)\right.\right.$$
$$\left.\left.\times (\omega + \omega^* - 2kv_z - \Omega) + \frac{\partial}{\partial P_z} kv_\perp\right]\frac{1}{|\omega - kv_z - \Omega|^2}\left[\Omega\frac{\partial}{\partial P_\perp} + kv_\perp\frac{\partial}{\partial P_z}\right]\right\}\langle f\rangle. \tag{10}$$

Substituting (10) into (8), one finally gets the phase coherent nonlinear density perturbation due to the instability,

$$\delta f_1 = \sum_{k,k'} i \frac{e^3\epsilon|\epsilon'|^2}{\omega|\omega'|^2} e^{-i(\omega'-\omega'^*)t}\frac{e^{i(kz-\omega t)}}{\omega - \Omega - kv_z} e^{i\theta}\left[(\omega - kv_z)\frac{\partial}{\partial P_\perp} + kv_\perp\frac{\partial}{\partial P_z}\right]$$
$$\times \left\{\frac{1}{P_\perp}\frac{\partial}{\partial P_\perp} P_\perp \frac{\partial}{\partial P_\perp} + \left[\left(\frac{\partial}{\partial P_\perp} + \frac{1}{P_\perp}\right)(\omega' + \omega'^* - 2k'v_z - \Omega) + \frac{\partial}{\partial P_z} k'v_\perp\right]\right.$$
$$\left.\times \frac{1}{|\omega - \Omega - k'v_z|^2}\left[\Omega\frac{\partial}{\partial P_\perp} + k'v_\perp\frac{\partial}{\partial P_z}\right]\right\}\langle f\rangle, \tag{11}$$

where ω' ($= \omega'(k')$) and ϵ' ($= \epsilon'(k')$) are the wave frequency and field intensity of radiation with wavenumber k'. One can note from (7) and (11) that the wave–particle resonant interaction occurs at $\omega_r - \Omega - kv_z = 0$ where ω_r is the real part of the wave frequency ω.

2.2. *Saturation of the instability*

The linear and nonlinear density perturbations, δf_0 and δf_1, give rise to the induced current density defined by

$$\delta\mathbf{J} = -en_0 \int dP_\perp dP_z \int_0^{2\pi} d\theta P_\perp (\mathbf{P}/\gamma m)\,\delta f,$$

where n_0 is the unperturbed background electron density. We shall show that the nonlinearly induced current, imposing a stabilizing effect, determines the saturation level of the instability. These induced currents, appearing in the following wave equation, acts as the driving source of the radiation:

$$\frac{\partial^2}{\partial t^2}\mathbf{E} - c^2\nabla^2\mathbf{E} = -4\pi\frac{\partial}{\partial t}\delta\mathbf{J}. \tag{12}$$

With the substitution of the calculated induced current densities, this wave equation yields the nonlinear dispersion relation for the synchrotron maser instability. It is found to be

$$\begin{aligned}\omega^2 - k^2c^2 = 2\pi\omega_p^2\Bigg[\int dP_\perp\, dP_z \frac{P_\perp}{\gamma}\left\{\frac{\omega - kv_z}{\omega - \Omega - kv_z} - \frac{P_\perp^2(\omega^2 - k^2c^2)}{2m^2c^2\gamma^2(\omega - \Omega - kv_z)^2}\right\} \\ \times\Bigg(f + \sum_{k'}\frac{e|\epsilon'|^2}{|\omega'|^2}\Bigg\{\frac{1}{P_\perp}\frac{\partial}{\partial P_\perp}P_\perp\frac{\partial}{\partial P_\perp} \\ + \left[\left(\frac{\partial}{\partial P_\perp} + \frac{1}{P_\perp}\right)(\omega' + \omega'^* - 2k'v_z - \Omega)\right. \\ \left. + \frac{\partial}{\partial P_z}k'v_\perp\right]\frac{1}{|\omega' - \Omega - k'v_z|^2}\left[\Omega\frac{\partial}{\partial P_\perp} + kv'_\perp\frac{\partial}{\partial P_z}\right]\Bigg\}\langle f\rangle\Bigg)\Bigg]\end{aligned} \tag{13}$$

where $\omega = \omega_r + i\Gamma$, the real and imaginary parts being the real wave frequency and the nonlinear growth rate, respectively.

Solving (13) for ω_r and Γ, we derive the nonlinear growth rate:

$$\begin{aligned}\Gamma = \frac{\pi^2\omega_p^2m^2c^2}{4\omega_r^2}\int_{P_{z1}}^{P_{z2}}dP_z\int_0^\infty dP_\perp P_\perp\left[\gamma + \frac{\Omega_0}{\omega_r} + \frac{kP_z}{m\omega_r}\right]\delta(P_\perp - P_{\perp 0}) \\ \times\left[\Omega\frac{\partial}{\partial P_\perp} + kv_\perp\frac{\partial}{\partial P_z}\right]\Bigg(f_0 + \sum_{k'}\frac{e^2|\epsilon'|^2}{\omega_r'^2}\Bigg\{\frac{1}{P_\perp}\frac{\partial}{\partial P_\perp}P_\perp\frac{\partial}{\partial P_\perp} \\ + \left[\left(\frac{\partial}{\partial P_\perp} + \frac{1}{P_\perp}\right)(2\omega_r' - 2k'v_z - \Omega) + \frac{\partial}{\partial P_z}k'v_\perp\right] \\ \times\frac{1}{|\omega' - \Omega - k'v_z|^2}\left(\Omega\frac{\partial}{\partial P_\perp} + k'v_\perp\frac{\partial}{\partial P_z}\right)\Bigg\}\langle f\rangle\Bigg),\end{aligned} \tag{14}$$

where

$$P_{z1,2} = mc\left[\frac{\Omega_0 kc \mp \omega_r(\Omega_0^2 + k^2c^2 - \omega_r^2)}{\omega_r^2 - k^2c^2}\right]^{\frac{1}{2}},$$

$$P_{\perp 0} = mc\left[\left(\frac{\Omega_0}{\omega_r} + \frac{kP_z}{m\omega_r}\right)^2 - 1 - \frac{P_z^2}{m^2c^2}\right]^{\frac{1}{2}}.$$

The following identities have been used in the derivation of (14):

$$\frac{1}{\omega - \Omega - kv_z} = \mathbf{P}\frac{1}{\omega_r - \Omega - kv_z} - i\pi\delta(\omega_r - \Omega - kv_z)$$

and

$$\delta(\omega_r - \Omega - kv_z) = \frac{\gamma[\gamma + \Omega_0/\omega_r + kP_z/m\omega_r]}{(2P_{\perp 0}\omega_r/m^2c^2)}\,\delta(P_\perp - P_{\perp 0})$$

for

$$P_{z1} < P_z < P_{z2}$$

where **P** means the principal part. We remark that the real wave frequency ω_r of the amplified radiation is determined primarily by the bulk electrons of the distribution rather than the resonant electrons. It is then reasonable to assume that the real wave frequency is only weakly affected by the nonlinearity due to the wave–particle interaction. Therefore, we will not include the effect of nonlinear frequency shift in the present work and simply approximate ω_r with the value derived from the linear dispersion relation deduced from (13) after dropping the nonlinear terms.

The saturation condition for the instability is determined by (14) after setting $\Gamma = 0$. The result has an unknown integral over the average background distribution function, $\langle f \rangle$. An estimate of it can be reasonably made on the basis of the following arguments. The growth rate of the instability and the distribution function can be assumed to remain unchanged for most of the instability evolution time. It is only during the final stage of the instability that the growth rate drops sharply to zero with the formation of a plateau in the velocity range of the distribution function where a positive slope existed originally. Mathematically while $|\omega - \Omega - kv_z|^2 \to 0$ because of the resonance condition and $\Gamma \to 0$ at the final stage of the instability, $[\Omega\partial/\partial P_\perp + kv_\perp \partial/\partial P_z]\langle f \rangle \to 0$ because of the formation of a plateau in the distribution function. For an order of magnitude estimate of the saturation level, we let

$$\frac{1}{|\omega' - \Omega - k'v_z|^2}\left(\Omega\frac{\partial}{\partial P_\perp} + k'v_\perp\frac{\partial}{\partial P_z}\right)\langle f \rangle \simeq \frac{1}{\Gamma_l^2}\left(\Omega\frac{\partial}{\partial P_\perp} + k'v_\perp\frac{\partial}{\partial P_z}\right)f_0 \qquad (15)$$

in (14), where

$$\Gamma_l = \frac{\pi^2\omega_p^2 m^2c^2}{4\omega_r^2}\int_{P_{z1}}^{P_{z2}} dP_z \int_0^\infty dP_\perp P_\perp \times\left[\gamma + \frac{\Omega_0}{\omega_r} + \frac{kP_z}{m\omega_r}\right]\delta(P_\perp - P_{\perp 0})\left[\Omega\frac{\partial}{\partial P_\perp} + kv_\perp\frac{\partial}{\partial P_z}\right]f_0 \qquad (16)$$

is the initial (namely, the linear) growth rate of the instability. The assumption that the growth rate of the synchrotron maser instability driven by a loss-cone distribution remains at its initial value for a large fraction of the time has been justified in Wu *et al.* (1981).

After a few exponentiation periods, the fastest growing wave becomes dominant. Since the frequency spectrum of the amplified radiation narrows down sufficiently, the single-wave approximation is good enough for the purpose of estimating the saturation level of the instability. In view of these points and noting that $\Gamma_l(k)$ is largest at $k = 0$ (Wu 1981), we can further simplify the analysis of (14) by considering only a single wave with $k = 0$ for estimating the upper bound of the saturated wave intensity.

2.3. *Intensity of the saturated radiation*

With these simplifications the integrations in (14) can be carried out analytically. Then, taking $\Gamma = 0$ in (14) leads to the following expression for the saturation intensity:

$$\frac{\epsilon_s^2}{4\pi n_0 T_e} = \frac{\bar{\omega}_r^2}{\bar{\omega}_p^2}\frac{3[j-2\alpha^2(j+1)/(2j+3)]}{2j(2j+3)(3j+1)}\left\{1+\frac{\bar{\omega}_r^2}{\gamma_l^2}\left[1-\frac{2(j+1)(3j+2)}{j(2j+3)(3j+1)}\alpha^2\right.\right.$$
$$\left.+\frac{4(j+1)(j+2)\alpha^4}{j(2j+3)(2j+5)(3j+1)}-\frac{(j-1)(2j+1)}{2(3j+1)\alpha^2}\right]$$
$$\left.+\frac{\beta^4\bar{\omega}_r^8}{\gamma_l^4}\left(1+\frac{\gamma_l^2}{\bar{\omega}_r^2}\right)\frac{(j+1)\alpha^2}{j(2j+3)(3j+1)}\left(j-\alpha^2\frac{2j+4}{2j+5}\right)\right\}^{-1} \tag{17}$$

where

$$\bar{\omega}_r = \omega_r/\Omega_0, \quad \bar{\omega}_p = \omega_p/\Omega_0, \quad \gamma_l = \Gamma_l/\Omega_0, \quad \beta^2 = \Delta P_j^2/m^2c^2$$

and

$$\alpha^2 = (1-\bar{\omega}_r^2)/\beta^2\bar{\omega}_r^2.$$

The normalized linear growth rate γ_l, obtained from (16), is given by

$$\gamma_l = \frac{\pi^{\frac{1}{2}}\bar{\omega}_p^2}{\beta^2\bar{\omega}_r}\alpha^{2j+1}e^{-\alpha^2}\frac{j!\,2^{2j+1}}{(2j+1)!}\left[j-\alpha^2\frac{2j+2}{2j+3}\right]. \tag{18}$$

It is clear from (18) that γ_l is negative for $j = 0$ corresponding to the case of a Maxwellian distribution (see (2)). The positive index j characterizes the velocity spread of the loss-cone distribution (defined by (2)) in the $v_\perp$ space. It is the population inversion in $P_\perp$ that provides the source of free energy for the synchrotron maser instability.

We now evaluate the intensity of the saturated radiation based on (17) with the intention of comparing resonant diffusion with quasi-linear diffusion as the dominant saturation process in auroral kilometric radiation that is amplified by the synchrotron maser instability. The typical magnetospheric parameters that were used by Wu (1981) to analyse quasi-linear diffusion in the loss-cone distribution with $j = 1$ are also adopted as follows:

$$\bar{\omega}_p = 0{\cdot}2, \quad T_e = 5\,\text{keV}, \quad n_0 = 1\,\text{cm}^{-3}, \quad \beta^2 \simeq 0{\cdot}02.$$

For the $k = 0$ mode, the calculated $\bar{\omega}_r$ is about 0·999 and then $\alpha \simeq 0{\cdot}112$ and $\gamma_l \simeq 6{\cdot}8\times10^{-3}$. With these parameters, we obtain the following results from (17):

$$\frac{\epsilon_s^2}{4\pi n_0 T_e} \simeq 8{\cdot}7\times10^{-5} \quad \text{or} \quad \frac{\epsilon_s^2}{4\pi} \simeq 7{\cdot}0\times10^{-13}\,(\text{erg cm}^{-3}) \tag{19}$$

for $n_0 = 1\,\text{cm}^{-3}$ and $T_e = 5\,\text{keV}$.

This energy density ($7{\cdot}0\times10^{-13}\,\text{erg cm}^{-3}$) of the saturated radiation is lower than those ($\simeq 10^{-10}\,\text{erg cm}^{-3}$) obtained from the consideration of the quasi-linear diffusion process by about two orders of magnitude. This indicates that resonant diffusion is more effective than quasi-linear diffusion in causing the saturation of the synchrotron maser instability that is driven by a loss-cone distribution.

3. Summary and Conclusions

We have formulated the theory of resonant electron diffusion as a saturation process of the synchrotron maser instability driven by a loss-cone electron distribution. We were motivated by the computer simulation work of Wagner *et al.* (1983). They showed that auroral kilometric radiation amplified by the synchrotron maser instability saturates when the resonant electrons diffuse into the loss cone via turbulent scattering of electrons by the excited radiation. We are able to evaluate analytically the intensity of the saturated auroral kilometric radiation. The ratio ($\simeq 8{\cdot}7 \times 10^{-5}$) of the saturated wave energy to the kinetic energy, as given in (19), is less than that ($\simeq 2{\cdot}0 \times 10^{-3}$) obtained in computer simulation by a factor of about 20 because different distribution functions and parameters are used.

The main purpose of this paper is to find out whether resonant diffusion indeed dominates over quasi-linear diffusion in causing the saturation of auroral kilometric radiation. The saturated radiation intensity has been calculated with the same distribution function and plasma parameters that were employed in Wu (1981) for the analysis of the quasi-linear diffusion process. The radiation saturated by the resonant diffusion process has a significantly lower intensity in comparison with that by the quasi-linear diffusion process. We conclude, therefore, that resonant electron diffusion provides the dominant process for saturating the synchrotron maser instability in the generation of auroral kilometric radiation as Wagner *et al.* (1983) demonstrated in the computer simulation.

The work at the Massachusetts Institute of Technology was supported jointly by the NASA grant NAG 5-270 and in part by the previous Air Force contract F19628-83-K-0024; that at the Polytechnic Institute of New York was supported jointly by the NSF grant ATM-8315322 and in part by the Air Force Office of Scientific Research, Air Force Systems Command, U.S. Air Force under grant AFOSR-85-0316 and 85-0133.

REFERENCES

Bekefi, G., Hirshfield, J. L. & Brown, S. C. 1961 *Phys. Rev.* **122**, 1037.

Benson, R. F. 1985 *J. Geophys. Res.* **90**, 2753.

Gurnett, D. A. 1974 *J. Geophys. Res.* **79**, 4227.

Gurnett, D. A. & Frank, L. A. 1973. *J. Geophys. Res.* **78**, 145.

Lin, C. S. & Hoffman, R. A. 1982 *Space Sci. Rev.* **33**, 415.

Melrose, D. B. 1976 *Astrophys. J.* **207**, 651.

Wagner, J. S., Lee, L. C., Wu, C. S. & Tajima, T. 1983 *Geophys. Res. Lett.* **10**, 483.

Wu, C. S. 1981 *Physics of Auroral Arc Formation* (ed. S. I. Akasofu and J. R. Kan). AGU Geophysical Monograph, vol. 25, p. 418.

Wu, C. S. & Lee, L. C. 1979 *Astrophys. J.* **230**, 621.

Wu, C. S., Tsai, S. T., Xu, M. J. & Shen, J. W. 1981 *Astrophys. J.* **248**, 384.

USSR, ACADEMY OF SCIENCE

MODIFICATION OF THE IONOSPHERE BY POWERFUL RADIO WAVES

(Proceedings of the International Symposium, Suzdal, september 1986)

MOSCOW 1986

Kuo, S.P., Polytechnic University, Route 110, Farmingdale, NY 11735
Lee, M.C., Massachusetts Institute of Technology, Cambridge, MA, 02139

PARAMETRIC EXCITATION OF WHISTLER WAVES BY HF HEATER

Recently, there is considerable interest in investigating mechanisms for generation and amplification of VLF/ELF/ULF waves in the ionosphere by high power HF waves. Experimental efforts together with theoretical studies have been continued during the past few years. The interpretations for the experimental observations include the modulation of the electrojet current,[1] thermal filamentation instability of the HF heater,[2] and parametric excitation of Alfven waves. In this work, the process for parametric excitation of whistler waves as the possible mechanism of VLF wave generation is studied.

We consider a L-H circularly polarized heater propagating upward along a downward geomagnetic field. A linearly increasing density profile $n=n_0(1+z/L)$ is assumed. If the frequency of the heater is less than the F-peak frequency, the heater becomes a standing wave and has the Airy function distribution. We select to the width of the first peak of the Airy function, the pump field in this region is then modeled by $\vec{E}_p = (\hat{x}-i\hat{y})\,[\epsilon_0/(1-|z/\Delta)]e^{-i\omega_0 t} = (\hat{x}-i\hat{y})\epsilon_p$.

We now study the process for the parametric decay of the heater into a whistler wave $(\omega,\vec{k}_1)$ and a Langmuir wave $(\omega_\ell,\vec{k}_\ell)$ pair in the first peak region, where $\omega_0=\omega+\omega_\ell-\delta$ and $\vec{k}_1(0)+\vec{k}_\ell(0)=\vec{k}$ are satisfied. From the wave equation, the coupled mode equation for the whistler wave field $\delta\vec{E}_w=(\hat{x}-i\hat{y})a_w \exp\{i(kz+\omega t+\int_0^z \delta k_w(z')dz')\}$ is obtained as

$$\left(\frac{\partial}{\partial t} - v_w\frac{\partial}{\partial z} + \nu_w\right)a_w = \frac{e}{m}\,\frac{k\Omega_e(\omega-\delta)}{\omega_{pe}^2(\omega_0-\Omega_e)}\,a_p a_\ell^* e^{-i\int_0^z \Delta\kappa(z')dz'} e^{i\delta t} \qquad (1)$$

where

$$v_w = 2kc^2\Omega_e/\omega_{pe}^2,\ \nu_w = \nu_e\,\omega/\Omega_e,\ \Delta k = \kappa' z,$$

$$\kappa' = -(\omega_p^2/L)(\omega/2k\Omega_e c^2+1/2kv_{te}^2),\ v_{te}^2 = 3T_e/m_e$$

and the expressions for the pump field $\epsilon_p=a_p e^{-i\omega_0 t}$ and the Langmuir wave field $\delta\vec{E}_\ell = \hat{z}a_\ell \exp\{i(kz-\omega_\ell t+\int_0^z \Delta k_\ell(z')dz')\}$ are used.

From the electron continuity equation, momentum transport equation, and Poisson equation, the equation for Langmuir wave is derived to be

$$\left(\frac{\partial}{\partial t} + v_\ell\frac{\partial}{\partial z} + \nu_\ell\right)a_\ell = \frac{e}{m}\,\frac{k\omega_p^2}{\omega_\ell\omega(\omega_0-\Omega_e)}\,a_p a_w^* e^{-i\int_0^z \Delta\kappa(z')dz'} e^{i\delta t} \qquad (2)$$

Taking the Laplace transform in time with p the Laplace transform variable, (1) and (2) can be combined into a second order differential equation as

$$\left[\frac{d^2}{dz^2} + f(z)\right]\psi(z) = 0 \qquad (3)$$

where

$$\psi = A_\ell \exp\{\frac{1}{2}\int_0^z f_1(z')dz'\},\ A_\ell = L(a_\ell),$$

$f_1(z)=(p+\nu_\ell)/v_\ell-(P+\nu_w-i\delta)/v_w+i\Delta k-1/(L+z)-1/(\Delta-iz)$, $f(z)=$
$-\frac{1}{4}[2(p+\nu_\ell)/v_\ell-f_1(z)]^2-\frac{1}{2}[i\kappa'+1/(L+z)^2+1/(\Delta-iz)^2]+\alpha^2(1-\delta/\omega)/(1+z^2/\Delta^2)$ and $\alpha^2=(e/m)^2k^2\Omega_e|a_0|^2/\omega_\ell(\omega_0-\Omega_e)^2\nu_\ell v_w$. Both the effects of the background inhomogeneity ($L\neq\infty$) and finite instability zone ($\Delta\neq\infty$) are included. Since, in reality, $L>>\Delta$ and $|\kappa'|<<1/\Delta^2$, we can thus approximate $f(z)\approx -1/4\Delta^2+\alpha^2(1-z^2/\Delta^2)$, and (3) becomes, in terms of the normalized coordinate $\zeta=(\alpha/\Delta)^{1/2}z$,

$$\left[\frac{d^2}{d\zeta^2} + (\alpha\Delta - 1/4\Delta\alpha - \zeta^2)\right]\psi = 0 \qquad (4)$$

The eigenvalue is thus determined by the equations $\alpha\Delta-1/4\alpha\Delta=2n+1$, which, in turn, determines the threshold of the instability to be

$$a_{0th} \geq (1.5+\sqrt{2})^{1/2}(\omega_0-\Omega_e)\,cv_w/\omega_{po}\Delta \qquad (5)$$

Since the geometry employed in this work is only appropriate for the high latitude ionosphere, the parameters of the Tromso facility[1] is thus chosen to evaluate the threshold of the instability. Substituting $\omega_0/2\pi = 4.04$ MHz, $\Omega_e/2\pi = 1.4$ MHz, $v_w \sim 10^5$ m/sec, and $\omega_{po} \cong \omega_0$ into (5) yields $a_{0th} \sim 1.2$ V/m. This value is lower than the peak amplitude of the electric field ~ 3 V/m available by the Tromso facility,[3] where the effect of swelling on the field amplitude has been included.

This work is supported jointly by the NSF Grant ATM-8315322, the AFOSR Grant AFOSR-85-0133, and the NASA Grant No. NAG-5-270.

References

1. Stubbe, P. and H. Kopka, "Generation of PC5 Pulsation by Polar Electrojet Modulation, First Experimental Evidence," J. Geophys. Res., 86, 1606, 1081.

2. Kuo, S.P. and M.C. Lee, "Earth Magnetic Field Fluctuation Produced by Filamentation Instabilities of Electromagnetic Heater Waves," Geophys. Res. Lett., 10, 970, 1083.

3. Stubbe, P. et al., "Ionospheric Modulation Experiments in Northern Scandinavia," JATP, 44, (12), 1025, 1082.

Lee, M.C. and Kong, J.A., Research Laboratory of Electronics, Massachusetts Institute of Technology, Cambridge, MA 02139, U.S.A.

Kuo, S.P., Polytechnic University, Route 110, Farmingdale, NY 11735, U.S.A.

ENHANCED IONOSPHERIC MODIFICATIONS BY THE COMBINED OPERATION OF HF AND VLF HEATERS

The combined operation of HF and VLF heaters is proposed to enhance ionospheric modifications in the F region with the following scenario. HF heater waves first illuminate the ionospheric F region with the expectation of generating intense field-aligned density striations. These greatly enhanced ionospheric density fluctuations, as shown below, are able to render the nonlinear mode conversion of VLF waves into lower hybrid waves. The subsequent injection of VLF pump waves into the HF wave- modified ionospheric region is expected to produce strong lower hybrid wave turbulence that can effectively heat the ionospheric plasmas. The enhanced modification effects in the ionosphere can be monitored by, for example, the measurements of airglow and height distribution of plasma lines (Carlson et al., 1982)

Suppose that the experiments are performed at high latitudes, the injected VLF waves propagating in the ionosphere is represented by a right-handed circularly polarized mode(i.e., whistler wave mode).

$$\bar{E}_o = (\hat{x} + i\hat{y}) E_o \exp i(k_o z - \omega_o t) \tag{1}$$

where E_o, k_o, ω_o have their conventional meanings of wave electric field, wave number, and wave frequency, respectively. The wave propagation direction has been taken to be along the z axis that coincides with the geomagnetic field. Then, the uniform electron oscillations responding to the whistler wave field form a uniform AC current at the whistler frequency. However, in the presence of ionospheric density irregularities, a nonuniform current can be induced by the scattering of the whistler wave from the density irregularities. The HF heater induced ionospheric density irregularities can be described as standing wave-like electrostatic fluctuations having sinusoidal spatial variation. Then, it can be shown that this nonuniform current is linearly proportional to the density fluctuation, δn , associated with the HF heater amplified ionospheric density irregularities.

From the analysis of perturbations in the wave equation, we find that the wave field perturbation, $\delta \bar{E}$, is related to the ionospheric density fluctuation by the following equation:

$$\delta E_x = -E_o(\delta n/n_o) - i\delta E_y \tag{2}$$

where δE_x and δE_y are the two components of the induced wave field perturbations stemming from whistler wave scattering by the ionospheric density irregularities, $(\delta n/n_o)$ is the fractional ionization density fluctuations. It can be clearly seen from (2) that a linearly polarized mode component has been introduced into the otherwise right- handed circularly polarized mode fluctuations. In other words, the scattering of whistler waves off ionospheric irregularities causes elliptically polarized mode perturbations. This linearly polarized mode component, whose field intensity is given by $\delta E_{lh} = E_o(\delta n\ n_o)$, has the outstanding characteristics of lower hybrid modes.

With the afore-mentioned features of HF wave-induced ionospheric irregularities, we can show that the induced elliptically polarized modes may have dominant nature of electrostatic modes(i.e., lower hybrid modes). This occurs when the injected VLF wave is scattered by ionospheric irregularities whose scale lengths are less than $l = 0.71(c\ f_p)(f_e/f_o)^{1/2}$, where c, f_p, f_e, and f_o are the speed of light in vacuum, the plasma frequency, the electron cyclotron frequency, and the VLF wave frequency, respectively. The value of l is found to be approximately 420 meters with the substitution of the following parameters: $c = 3 \times 10^8, f_p = 6$ MHz, $f_e = 1.4$ MHz, and $f_o = 10$ KHz. It has been generally known that the HF heater-induced irregularities have scale lengths ranging from tens of centimeters to a few kilometers(e.g., Erukhimov et al., 1979; Farley et al., 1983 and references therein). Our preliminary analysis, therefore, has indicated that the HF heater-produced irregularities are able to scatter the injected VLF pumps into lower hybrid waves.

In summary, the proposed operation of HF and VLF heaters is expected to create intense lower hybrid wave turbulence that can greatly enhance the ionospheric modification effects in the F region for future experiments to corroborate.

This work is supported jointly by the NASA grant NAG-5-270(M.I.T.) and the NSF grant ATM-8315322, and the AFOSR grant AFOSR-85-0133(P.U.).

References:

Carlson, H.C., V.B. Wickwar, and G.P. Mantas, Observation of Fluxes of suprathermal electron accelerated by HF excited instabilities, J. Atmos. Terr. Phys., 44, 1089, 1982.

Erukhimov, L.M., V.I. Kovalev, A.M. Lerner, E.N. Myaskinov, I.N. Poddel'skii, and A.V. Rakhilin, Spectrum of large-scale artificial inhomogeneities in the F layer of the ionosphere, Radio Phys. Quantum Electron. Engl. Transl., 22, 888, 1979.

Farley, D T., C. LaHoz, and B.G. Fejer, Studies of the Self-focusing instabilirty at Arecibo, J. Geophys. Res., 88, 2093, 1983.

Lee, M.C. and J.A. Kong, Research Laboratory of Electronics, Massachusetts Institute of Technology, Cambridge, MA 02139, U.S.A.

Kuo, S.P., Polytechnic University, Route 110, Farmingdale, NY 11735, U.S.A.

ON THE RESONANT IONOSPHERIC HEATING AT THE ELECTRON GYROFREQUENCY

The thermal filamentation instability of radio waves can operate in a very broad range of wave frequencies in space plasmas. It has been suggested to be responsible for the geomagnetic field fluctuations induced by the HF heater located at Tromso, Norway (Kuo and Lee, 1983). The excited high frequency sidebands and the zero-frequency modes (associated with magnetic and density fluctuations) are not eigen modes rather the nonlinearly driven modes. When the pump wave frequency is not very close to the electron gyrofrequency, the instability threshold is primarily determined by the off-resonance(i.e., the detuning) effect as the dominant damping mechanism of the instability.

However the threshold is mainly imposed by the electron cyclotron damping as the heater wave frequency matches the electron gyrofrequency. It is interesting to examine the excitation of the thermal filamentation instability at the electron gyrofrequency, because ionospheric resonant heating at the electron gyrofrequency conducted in the U.S.S.R. has produced some intriguing nonlinear ionospheric phenomena(Migulin and Gurevich, 1985 and references therein). The main purpose of the present paper is to analyze the thermal filamentation instability in the ionosphere excited by the heater operated at the electron gyrofrequency.

For simplicity, the incident hater wave is assumed to have right-handed circular polarization. In the presence of the thermal filamentation instability, the total field of the heater wave is given by

$$\vec{E}_o = \{e_o(\hat{x} + i\hat{y}) + (e_{1-}\cos kx + \hat{z}e_{1z}\sin kx)\exp(\gamma t)\}\exp[i(k_o z - \omega_o t)] + c.c \tag{1}$$

where $(e_{1-}\cos kx + \hat{z})e_{1z}\exp(\gamma t)$ is the excited sideband field having the growth rate, and the filamentation vector, $\vec{k} = k\hat{x}$. The perturbations in plasma density, temperature, the magnetic field, etc. associated with the concomitant excitation of the zero-frequency modes have the general form $\delta p = \delta\bar{p}(\cos kx)\exp(\gamma t)$.

The high-frequency side-band mode satisfies the following Fourier transform wave equation,

$$\left(k_o^2 + k^2 - \frac{\omega_o^2}{c^2}\right)\bar{\bar{I}} - k_o\hat{z}\hat{z} - k^2\hat{x}\hat{x} + ik_o\frac{\partial}{\partial z}(\hat{x}\hat{z} + \hat{z}\hat{x})\cdot\vec{e} = i\frac{4\pi\omega_o}{c^2}\vec{j} \tag{2}$$

where $\bar{\bar{I}}$ denotes the unit dyadic. The induced current density, $\vec{J}$, is composed of three components resulting from the linear response of electrons to the sideband field or the nonlinear coupling between the zero-frequency modes and the pump wave field.

An interesting characteristic of the thermal filamentation instability is the condition for the simultaneous excitation of plasma density fluctuations and the magnetostatic fluctuations of the form: $\delta\vec{B} = \hat{z}\delta B(\cos kx)\exp(\gamma t)$. It is

$$\delta n/n_o = \left[1 + (1 + \nu_e/\gamma)(k^2c^2 + \gamma^2)/\omega_p^2\right](\delta B/B_o) \tag{3}$$

where ν_e is electron-ion collision frequency. The coupled mode equation for the zero-frequency modes is found to be

$$\left\{(\gamma^2 + k^2c^2)[1 + \frac{m}{M}(1 + \nu_e/\gamma)f] + \omega_i^2 f\right\}\delta A = (4\pi n_o ec/\Omega_e)\left[F_x + \frac{4}{3}(\nu_e/\gamma)\frac{\partial}{\partial x}(\vec{v}_o\cdot\vec{v}_1 + \vec{v}_o\cdot\vec{v}_1')\right] \tag{4}$$

where $f = (\gamma^2 + k^2c_s^2 + \frac{2}{3}\gamma k^2v_e^2/\gamma)/\Omega_i^2$ and $\omega_i(\Omega_i)$, n_o, and $m(M)$ are the ion plasma (cyclotron) frequency, the unperturbed plasma density and the electron(ion) mass, respectively. $\gamma = \gamma + 2\nu_e(m/M) + \nu_e k^2v_e^2/\Omega_e^2$. F_x is the x component of the nonlinear Lorentz force experienced by electrons.

The dispersion relation can be derived from (2) and (4). The preliminary analysis of it has shown that the threshold of the instability can be exceeded by the available power of the heater waves. Detailed analyses and discussions on the thermal filamentation instability will be presented at the meeting.

This work is supported jointly by the NASA grant NAG-5-270(M.I.T.) and the NSF grant ATM-8315322, and the AFOSR grant AFOSR-85-0133(P.U.).

References

Kuo, S.P. and Lee, M.C., Earth magnetic field fluctuations produced by filamentation instabilities of electromagnetic heater waves, Geophys. Res. Lett., 10, 979, 1983.

Migulin, V.V. and Gurevich, A.V., Investigation in the U.S.S.R. of nonlinear phenomena in the ionosphere, J. Atmos. Terr. Phys., 47, 1181, 1985.